Cape Peninsula University of Technology

Research Thesis

Submitted in fulfilment of the requirements

for the degree of

Master of Technology in Chemical Engineering

Title: **Development of A Predictive Haze Index to Reflect Observed Visibility Degradation in the City of Cape Town**

Candidate: *Jongikhaya Witi*

BTech (Cum Laude) Chemical Engineering

Internal Supervisor: *Prof. E.K. Cairncross*

B.Sc., (Chem. Eng.), PhD

Head of Department: Chemical Engineering

Cape Peninsula University of Technology

Dedication

This thesis is dedicated to my loving parents who sadly passed away in the past two years since I have been busy with my masters. As much as I have achieved what I have achieved, I will always look back and say this has been one of the most painful times in my life.

Statement

THE DEVELOPMENT AND VALIDATION OF A HAZE INDEX TO REFLECT THE OBSERVED VISIBILITY DEGRADATION IN THE CITY OF CAPE TOWN

I declare that the content of this thesis represents my own work, with the exception of those particular cases that are referenced in the text of the thesis. I also declare that this thesis has not been submitted to any other educational institution for the purpose of the awarding of an academic qualification.

December 2006

J. Witi

Acknowledgements

My sincere appreciation and gratitude are due to the following people and organizations:

Prof. Eugene K. Cairncross, Department of Chemical Engineering, Cape Peninsula University of Technology, under whose supervision this research was conducted, for his constant support and invaluable guidance.

Dr. Vinit K. Mistra, Department of Chemical Engineering, Cape Peninsula University of Technology, under whose co-supervision of this research has taught me a great deal in the field of Atmospheric Chemistry as well as air pollution.

Mr. Emmanuel Rusford, Department of Environmental Health, Cape Peninsula University of Technology, for his assistance in teaching me the fundamentals of biostatistics as well as Multiple Regression Techniques.

Mr. Luo Chin-Hsiang, Department of Environmental Engineering, Hung-Kuang University, Taiwan , for offering guidance in the field of Digital Image Processing.

Dr. Mark Zunckel, Council for Scientific and Industrial Research, Durban, for constant motivation and valuable tips.

Mr. Bruce Hendry, Department of Chemical Engineering, Cape Peninsula University of Technology, for providing invaluable advices and insights during the times of difficulty and stagnation.

Tifaranyike (Tuffy) Madzimabuto, Department of Chemical Engineering, Cape Peninsula University of Technology, for his constant motivation and experience.

Hassan Adam, Department of Chemical Engineering, Cape Peninsula University of Technology, for constant support and motivation.

Ms. Sally Benson, Scientific Services in Cape Town, for providing air pollution data on continuous basis throughout the life of this project. Going through the process of acquiring the data myself made me to appreciate the effort needed to pull out this information.

National Research Foundation, for its financial support which has helped a great deal in the ensuring the continuous existence of this project.

Dynamic Air Pollution Prediction System Project, for its financial support of the project which has ensured that the project is sustainable

Abstract

Measurement and forecasting of visibility is essential in assessing the extent of visibility degradation (haze) due to air pollution in Cape Town. Rapid impairment in visibility over the years forced the City of Cape Town to initiate the Brown Haze I (BH I) study in September 1997. The main objective of the Brown Haze I Study was to determine the contribution of all major pollutant sources to the brown haze, and to determine other factors that contribute to haze formation. However to date no study has attempted to devise quantitative methods to monitor visibility in Cape Town.

This study reports on a new method of measuring visibility using Digital Image Processing. An hourly series of time-stamped images of three scenic vistas was recorded over a period of 8 months (20060318 to 20061031) using three co-located Sanyo E-6311xP-H digital cameras equipped with E-50500D 20 to 100mm Variable-focal Auto Iris Lenses. The cameras were orientated in three directions (approximately due west, north and east). These time- stamped images were archived for subsequent digital image processing. The average image intensities of selected areas of each image were calculated using the histogram function of digital image processing software (Photoshop^{TM} 7.0), to obtain the inherent and apparent contrast ratios. The inherent and apparent contrast measurements were then used to calculate light extinction coefficient (b_{ext}) and the visual range (VR).

The Koschmeider equation was used to convert light extinction into visual range. The effectiveness and accuracy of this method was examined by estimating the % uncertainty in the calculated light extinction (b_{ext}) relative to ambient values of light extinction coefficient obtained from the light extinction model. Estimated uncertainties associated with light extinction coefficients from contrast measurements were observed to be lower than 12 % in winter and lower than 9 % in summer. These uncertainties are significantly lower when compared to those observed using other methods of estimating light extinction coefficient.

The influence of sun angle on visibility was also investigated by measuring inherent contrast at different times of the day in a pristine environment. These measurements confirmed that inherent contrast changes with the sun angle. Thus inherent contrast calibration curves were generated to correct for the effect of the sun angle.

Although a limitation in this study is that the calibration of visual range estimates by digital image processing was performed by using the light extinction coefficient model rather than, for example, comparison with measurements using three co-located transmissometers, there is a strong agreement between visual range estimates from both methods, particularly during midday. High correlation coefficients are observed between the calibration curves generated using visual range estimates from digital image processing versus visual range measurements from the light extinction model.

In addition, real time visibility observation, air pollution and meteorology sampling were conducted to investigate the influence of air pollutants (gases and aerosols) and some meteorological factors on visibility and extinction coefficients in Cape Town. Multiple linear regression methods including variable selection (stepwise regression) and model diagnostic methods were applied in order to develop real-time visibility forecasting models. In total, six models were developed (models for two seasons and three directions). Furthermore, for all six developed models, a minimum 74 % of variability in visual range was explained by the modelled relationship with the air pollutant concentrations and the meteorological variables used to predict visibility. This was achieved through the removal of influential observations and outliers by model diagnostic methods. Meteorological parameters such as relative humidity and wind speed played a significant effect on the reduction of visibility in Cape Town.

This study has confirmed light scattering by particles to be the major contributor to light attenuation. Particle scattering (b_{sp}) in Cape Town of 79 % (95% CI: 54 - 94) compared well with b_{sp} contributions in Los Angeles (1982) were an average of up to 78% was observed. These studies where however done two decades ago.

A haze index scale is proposed which is made up of two components. With its two components (haze index and visibility descriptor), this haze index scale provides a linear scale of visibility degradation as a means of communicating visual range measurements using a numerical index as well as a description of the extent of visibility degradation. Unlike other haze index scales in existence (e.g. deciview haze index scale), this haze index scale is linear to perceived changes in visibility conditions. The haze index range from 10 to 1 on a numerical scale and has visibility descriptor range from excellent to very poor. A value of 10 is equivalent to < 1.5 km

visibility while a value of 1 is equivalent to > 70 km visibility. This haze index is derived from the same principle as the Dynamic Air Pollution Prediction System (DAPPS) air pollution index (API) which also uses numerical indicator as well as visibility descriptor. In the real-time forecasting results presented in this study, it was demonstrated that 3% of the forecasted visibility was less than 1.5 km (very poor visibility level), 6 % (poor visibility level), 32 % (acceptable visibility level), 55 % (good visibility level) and 4% (excellent level) for summer month.

Table of Contents

Contents

Page No.

List of Tables

List of Figures

List of Figures (Continued)

Nomenclature and Abbreviations

Symbol	Description	Units
[C]	Concentration	μgm^{-3}
BH	Brown Haze	
b_{ext}	Extinction Coefficient	m^{-1}
b_{ag}	Absorption Coefficient [Gases]	m^{-1}
b_{ap}	Absorption Coefficient [Particles]	m^{-1}
b_{sg}	Scattering Coefficient [Gases]	m^{-1}
b_{sp}	Absorption Coefficient [Particles]	m^{-1}
b_{rg}	Extinction coefficient [Rest of atmospheric gases]	m^{-1}
C_o	Inherent Contrast	Dimensionless
C_x	Apparent Contrast	Dimensionless
CM	Course Mass [$PM_{10} - PM_{2.5}$]	μgm^{-3}
CPU	Central Processing Unit	
CCT	City of Cape Town	
CMYK	Cyan Magenta Yellow Black	
DIP	Digital Image Processing	
EC	Elemental Carbon	μgm^{-3}
e_i	Residual	Dimensionless
FFT	Fast-Fourier Transform	
G_x, G_y	Pixel mean values	
GPS	Global Positioning System	
IMPROVE	Interagency Monitoring of Protected Visual Environments	
IPCC	Intergovernmental Panel on Climate Change	
ICAO	International Civil Aviation Organization	
JPEG	Joint Photographic Experts Group	

Nomenclature and Abbreviations (Continued)

Symbol	Description	Units
MLR	Multiple Linear Regression	
MPI	Mean Pixel Intensity/ Brightness	Gray scale [0-255]
MRADs	Minor Restricted Activity Days	
NO_3^-	Nitrate Ion	μgm^{-3}
NO	Nitric Oxide	μgm^{-3}
NO_x	Oxides of Nitrogen	μgm^{-3}
O_2	Oxygen molecule	μgm^{-3}
O_3	Ozone molecule	μgm^{-3}
PAHs	Poly Aromatic Hydrocarbons	
PC	Personal Computer	
PMT	Photomultiplier tube	
$PM_{2.5}$	Particulate Matter with aerodynamic diameter of 2.5μm or less	μgm^{-3}
PM_{10}	Particulate Matter with aerodynamic diameter of 10μm or less	μgm^{-3}
PNA	Poly-nuclear aromatics	
R	Response of a pixel	
RAD	Restricted Activity days	
RGB	Red Green Blue light model	
RH	Relative Humidity	Percentage
SD	Standard Deviation	
SO_2	Sulphur Dioxide	μgm^{-3}
SO_4^{2-}	Sulphate Ion	μgm^{-3}
SO_x	Oxides of Sulphur	μgm^{-3}
TEOM	Tapered Elementary Oscillating Mass	
TIFF	Tagged Image File Format	
TOR	Thermal Optical Reflectance	

Nomenclature and Abbreviations (Continued)

T/P	Temperature/Pressure	
USEPA	United States Environmental Protection Agency	
USNHIS	United States Health Interview Survey	
UV	Ultraviolet	
VOCs	Volatile Organic Compounds	μgm^{-3}
Vr	Visual Range	km
w	Weighting coefficients in a 3 x 3 matrix	
WLDs	Work Loss Days	
z_i	Mean gray level values	

Chapter 1: Overview

1.1 Introduction

When the industrial revolution started way back in the 16th century, little did people know that 300 years in the future it would pose a threat to occupational health, safety and the environment including the climate. Not only has it done that, but has also managed to pose a threat to the ability of a person to see and appreciate scenic vista. Thus visibility degradation (haze) has been the subject of a number of air pollution studies around the world including Cape Town over past few decades. Rapid deterioration in visibility over the years persuaded the City of Cape Town to initiate the Brown Haze I (BH I) study. The main objective of the Brown Haze Study was to determine the contribution of all major sources to the brown haze, and to obtain a better understanding of the mechanism of haze formation. The focus of the study was therefore on visibility, rather than health, although the two are closely related. It should be noted that localized air pollution problems were not addressed in this study.

Although visibility degradation itself causes no adverse health effects, it usually indicates the presence of pollutants harmful to health. These pollutants (visibility degrading species) are found to be associated with health problems such as increases in daily mortality, and asthma [3]. Therefore visibility degradation is not just a visibility problem but is also a visual indicator of air quality [4]. Although Cape Town does not experience the serious atmospheric pollution problems of the other cities locally and abroad, it is the fastest growing urban region in South Africa and past studies have reported cases of adverse health effects in industrial areas within the city[5]. Generally, in urban areas, particles less than 2.5 microns in size ($PM_{2.5}$) are the single largest cause of visibility impairment. They are also the most harmful size range of particles to human health. Recent in-depth studies support a link between adverse health effects and fine particles with diameters less than 2.5 μm ($PM_{2.5}$) [6]. As a result, $PM_{2.5}$ has been targeted for chemical speciation by various countries because these small particles have the ability to penetrate into sensitive regions of the human respiratory tract [7].

The City of Cape Town (CCT) has recently realized the need for sampling fine particulate matter. This will in turn help researchers in their quest to understand better the health impacts associated with fine particulates. These particulates together

with a few atmospheric gases reduce visibility by scattering and absorption of visible radiation.

Visibility in the vicinity of airports is of importance to the aviation and to the tourism industries. Visibility impairment observed in airport runways may impact the scheduling of flights. Also of concern is the possible effect of increasing haze to the tourism industry, Cape Town's major growth industry. Effective control and management of visibility impairment require an understanding of the pollution sources that cause the degradation, and a practical way of measuring visibility.

In Cape Town, haze conditions occur mostly from April to September due to strong temperature inversions and windless conditions that can occur during these months, which leads to the build-up of pollutants emitted into the atmosphere. The haze extends over most of the Cape metropole area and is normally most intense in the morning and then lifts and disperses. It has a strong degrading effect on visibility, which is immediately apparent to the general public and to tourists. Capetonians are especially proud of the natural beauty of their city, and the haze is increasingly eroding this pride. Also of concern is the effect on the tourist industry, which is projected to be Cape Town's most important economic growth area. Recent concern has been expressed about the increasing incidence and intensity of the haze [8]. In recent times, the effects of haze are becoming prominent in remote areas due to transport of pollutants over long distances. Fine particulate matter is the major cause of reduced visibility and can be a major source of contaminants imported into otherwise pristine environments such as national parks and natural landmarks.

Visibility, as it relates to management of the many visual resources found in national parks, is a complex and difficult concept to define. The difficulty is whether to explain visibility in strictly technical terms that concern themselves with exact measurements of illumination, threshold contrast, and precisely measured distances or with value judgments of an observer viewing a scenic vista.

Historically, visual range has been defined as the greatest distance at which an observer can just see a black object viewed against the horizon sky [9]. An object is usually referred to as at threshold contrast when the difference between the brightness of the sky and the brightness of the object is reduced to such a degree that an observer

can just barely see the object. Much effort has been expended in establishing the threshold contrast for various targets under a variety of illumination and atmospheric conditions. An important result of this work is that threshold contrast for the eye, adapted to daylight, changes very little with background brightness, but it is strongly dependent upon the size of the target and the time spent looking for the target. Threshold contrast also varies significantly from individual to individual [7].

Nevertheless, visibility is more than being able to see a black object at a distance for which the contrast reaches a threshold value. On interpreting visibility, the observer will comment on the colour of the mountain, on whether geological features can be seen and appreciated, or on the amount of snow cover resulting from a recent storm system. In some cases the observer may comment on the contrast detail of nearby geological structures or on shadows cast by overhead clouds. Therefore visibility is more closely associated with conditions that allow appreciation of the inherent beauty of landscape features. It is important to recognize and appreciate the form, contrast detail, and colour of near and distant features.

Because visibility includes psychophysical processes and concurrent value judgments of visual impacts, as well as the physical interaction of light with particles in the atmosphere, it is of interest to understand the psychological process involved in viewing a scenic resource, the value that an observer places on visibility, and to be able to establish a link between the physical and psychological processes [7].

Thus, whether we define visibility in terms of visual range or in terms of some parameter more closely related to how visitors perceive a visual resource, the preservation or improvement of visibility requires an understanding of the constituents in the atmosphere that impair visibility as well as the origins of those constituents.

Introduction of particulate matter and certain gases into the atmosphere interfere with the ability of an observer to see landscape features. Monitoring, modelling, and controlling sources of visibility-reducing particulate matter and gases depend on scientific understanding of how these pollutants interact with light, transform from a gas into particles that impair visibility, and are dispersed across land masses and into local canyons and valleys. Scientific understanding of some of these issues is more

complete than of others. Chapter three discusses the scientific conceptual framework on which quantification of visibility reduction is dependent.

Visibility involves more than specifying how light is absorbed and scattered by the atmosphere. Visibility is a psychophysical process of perceiving the environment through the use of the eye-brain system [7]. Important factors involved in seeing an object are outlined in Figure 1.1 and summarized here.

- Illumination of the overall scene by the sun, including illumination resulting from sunlight scattered by clouds and atmosphere as well as reflections by ground and vegetation

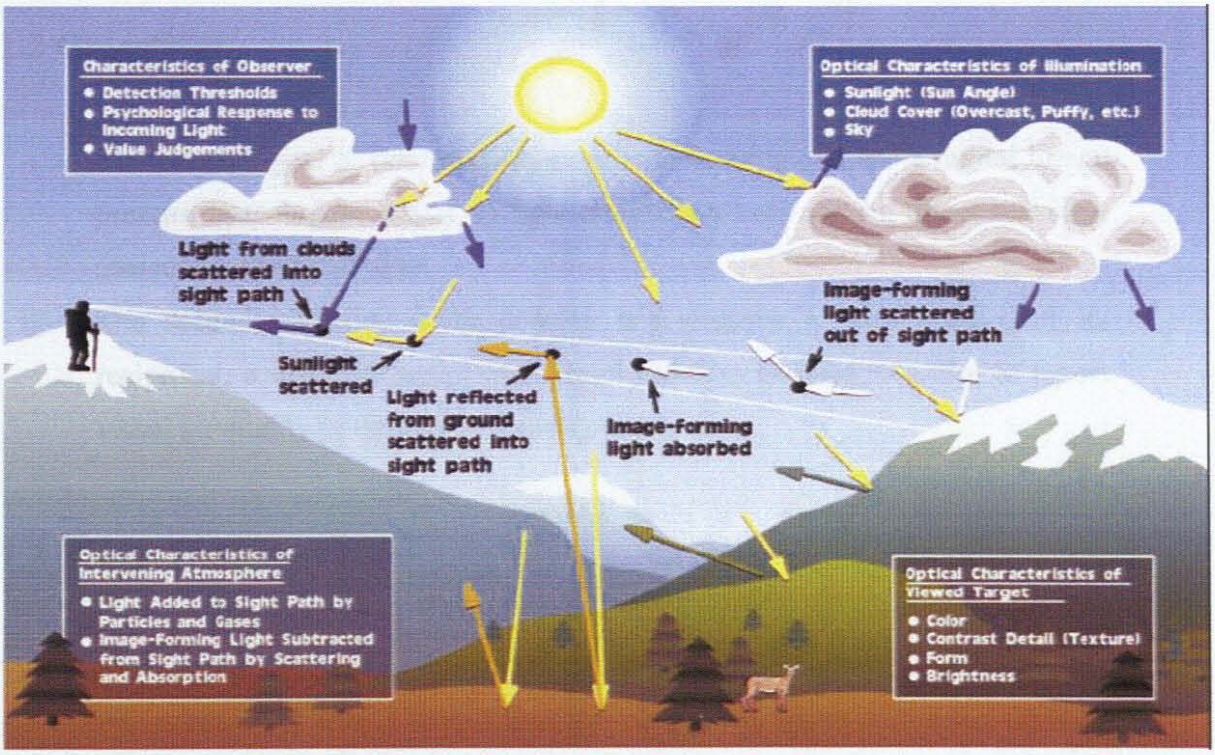

Figure 1.1: Important factors involved in seeing a scenic vista; figure adapted from Malm [10].

- Target characteristics that include colour, texture, form, and brightness.
- Optical characteristics of intervening atmosphere:

I. image-forming information (radiation) originating from landscape features is scattered and absorbed (attenuated) as it passes through the atmosphere toward the observer, and

ii. Sunlight, ground reflected light, and light reflected by other objects are scattered by the intervening atmosphere into the sight path.

- Psychophysical response of the eye-brain system to incoming radiation.

It is important to understand the significance of the light that is scattered in the sight path toward the observer. The amount of light scattered by the atmosphere and particles between the object and observer can be so bright and dominant that the light reflected by the landscape features becomes insignificant. This is somewhat analogous to viewing a candle in a brightly lit room and in a room that is in total darkness. In the first case, the candle can hardly be seen, while in the other it becomes the dominant feature in the room.

1.2 Objectives

i. The primary goal of this research work is to develop and use a digital image processing technique based on light attenuation laws for the direct real-time measurement of visibility.

ii. The second objective is to develop and propose a haze scale (and its reciprocal, a visibility scale) and a haze index to be used as a tool to report visual air quality in the city of Cape Town.

1.3 Thesis Outline

The outline of this thesis is as follows: Chapter 2 deals with the relationship between aerosols properties and optical effects, and their impact on health and global climate. Chapter 3 deals specifically with the optical effects of aerosols and gases and the theory behind light attenuation by these air pollutants. Chapter 3 also provides a method of quantify light attenuation as well as the translation of light attenuation into visibility measurement (Visual range or Meteorological range). In addition, the concept of using digital image processing for visibility measurement is developed. Chapter 4 outlines the selection of the study area, the instrumentation and software used as well as the equations used. Chapter 5 presents the results obtained from various data analysis methods such as Multiple Regression techniques. In addition, the haze index and its scale are developed. Chapter 6 discusses the results presented

in chapter 5. Chapter 7 outlines the conclusions drawn from discussions in chapter 6 and discusses some recommendations on how to improve the methodology for real time visibility estimates as well strengthening of the visibility measurement method developed in this study. The Appendices follows which displays the figures referred to, where applicable, throughout the document as well as additional background material. Finally, the list of references used is displayed at end of the thesis.

Chapter 2: Atmospheric Aerosols

2.1 Introduction

Atmospheric aerosols have significant local, regional and global impacts. Regionally, aerosols can be transported from areas of high emissions to relatively clean remote regions. Local sources of aerosols in the City of Cape Town include vehicular emissions, wood burning fires and industrial processes that can lead to urban air pollution [11]. Aerosols have the potential to significantly influence our entire planet through their role in heterogeneous chemistry in the troposphere and stratosphere [12], as well as their effect on the Earth's climate as they reflect, absorb and scatter sunlight and serve as condensation nuclei for cloud droplet formation [13]. At present, the radiative effects of aerosols have the largest uncertainties in the global climate predictions to quantify climate forcing due to anthropogenic changes in the composition of the atmosphere. A better understanding of the formation, composition and transformation of aerosols in the atmosphere is of critical importance in order to better quantify these effects.

The word aerosol was introduced more than 80 years ago as an analogy to the term hydrosol, a stable liquid suspension of solid particles in water [14]. An aerosol is defined in its simple form as solid or liquid particles suspended in a gas, and it includes a wide range of phenomena such as dust, fume, smoke, mist, fog, haze, and smog. Atmospheric aerosols are generally considered to be particles that range in size from a few nanometers (nm) to tens of micrometers (μm) in diameter. Particles may either be emitted directly into the atmosphere or formed there by oxidation of precursor gases, such as sulphur dioxide, nitrogen oxides and volatile organic compounds (VOCs), where the resulting oxidation products nucleate to form new particles or condense on pre-existing ones. Particles directly emitted from sources and those that are formed in the atmosphere are referred to as primary and secondary particles, respectively. Particles in the atmosphere arise from natural sources as well as anthropogenic activities. The former source includes windborne dust, sea spray, volcanic activities and biomass burning, while emissions of particles attributable to the activities of humans arise primarily from four source categories: fuel combustion, industrial processes, non-industrial fugitive sources (e.g. construction work), and transportation sources (e.g. automobiles). Natural aerosols are probably 4 to 5 times

larger than anthropogenic ones on a global scale, but regional variations in man-made pollution may change this ratio significantly in certain areas, particularly in the industrialised Northern Hemisphere [15].

Once airborne, particles can change their size and composition by condensation of vapour species or by evaporation, by coagulation with other particles, by chemical reaction, or by activation in the presence of water super-saturation to become fog and cloud droplets (see figure 2.1). Particles are eventually removed from the atmosphere by two mechanisms: deposition at the Earth's surface (dry deposition) and incorporation into cloud droplets during the formation of precipitation (wet deposition). Because wet and dry deposition lead to relatively short residence times in the troposphere, and because the geographical distribution of particle sources is highly non-uniform, tropospheric aerosols vary widely in concentration and composition over the Earth. Whereas atmospheric trace gases have lifetimes ranging from less than a second to a century or more, residence times of particles in the troposphere vary only from a few days to a few weeks [13].

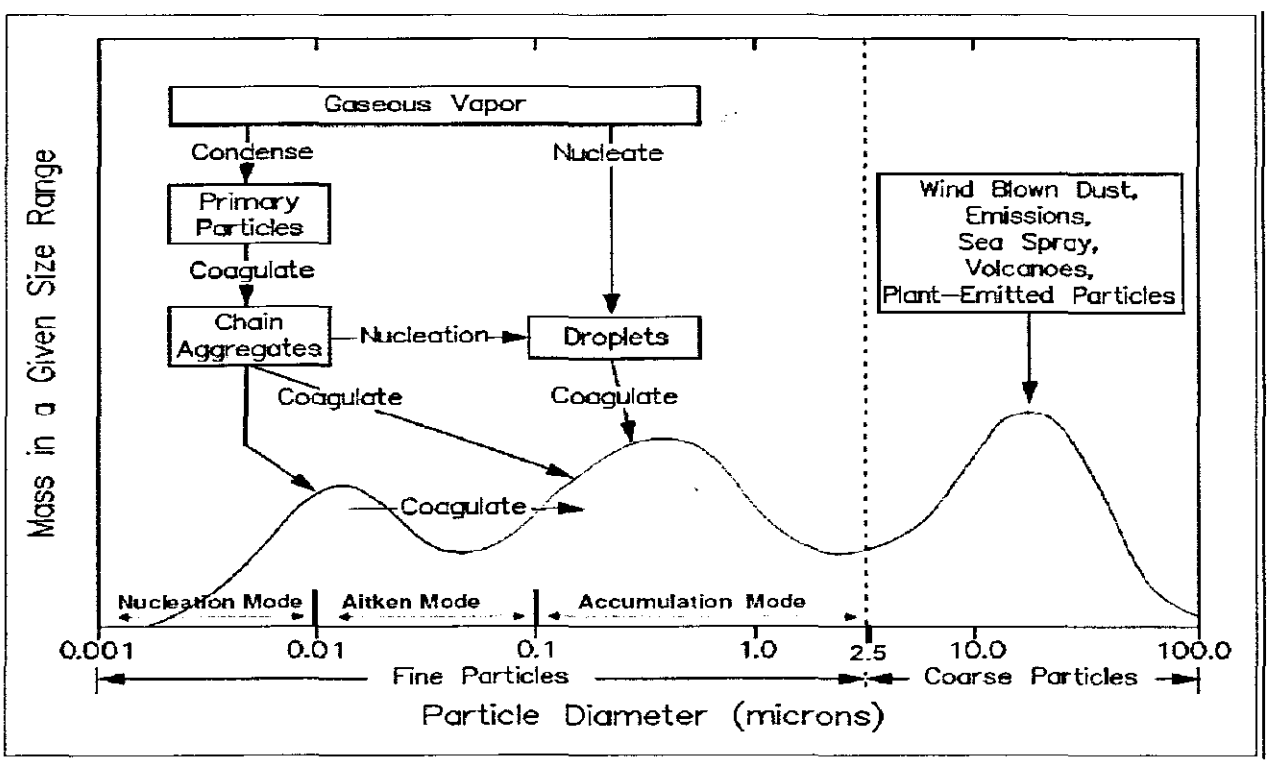

Figure 2.1: An idealized illustration showing TSP, as well as fine $PM_{2.5}$ and coarse (PM_{10}-$PM_{2.5}$) Particle ranges, with their major chemical mass components (adapted from Whitby and Cantrell, 1976 and EPA, 1999).

2.2 Relevance of Atmospheric Aerosols to Visibility

Anthropogenic emissions of atmospheric aerosols and their precursors have increased dramatically over the past century and have been implicated in many areas ranging from human health to climate change [13]. To the Public, the degradation of visibility is perhaps the most visible aspect of urban and regional air pollution. Aerosol particles in the size range of 0.1-2.5 μm are major contributors to this phenomenon because of their highly efficient light scattering properties [16]. Aerosols can also act as sites for heterogeneous chemical reactions to take place [9]. The most significant of these reactions are those that lead to the destruction of the stratospheric ozone. During winter in Polar Regions, aerosols grow to form polar stratospheric clouds. The large surface areas of these cloud particles provide sites for chemical reactions to take place. These reactions lead to the formation of large amounts of reactive chlorine and, ultimately, to the destruction of ozone in the stratosphere [17]. In addition to visibility and heterogeneous chemistry implications, the effects of atmospheric aerosols on human health and global climate have been increasingly recognised.

2.3 Aerosol Properties

2.3.1 Particle Size Definitions

Atmospheric particles are usually referred to as having a diameter, implying they are spherical. However, particles in the atmosphere have widely variable shapes for which geometrical diameters are more meaningful. Some means of expressing the size of such particles is essential since important properties of the particles such as volume, mass, surface area and velocity depend on the size and size [12]. In practice, the size of such irregularly shaped particles is expressed in terms of an equivalent diameter that depends on a physical, rather than a geometrical, property. An equivalent diameter is defined as the diameter of the sphere that would have the same value of a particular physical property as that of the irregular particle [12].

There are different definitions of equivalent diameters. One of the most commonly used is the aerodynamic diameter, D_a, which is defined as the diameter of a sphere of unit density (1 gcm^{-3}) that has the same settling velocity in air as the particle under

consideration. Aerodynamic diameter standardizes particles of various shapes and densities to spheres having the same aerodynamic property, settling velocity. The particle aerodynamic diameter D_a is given by equation 2.1

$$D_a = D_g k \sqrt{\frac{\rho_p}{\rho_0}} \tag{2.1}$$

Where D_g is the particle geometric diameter, ρ_p is the density of the particle; ρ_o is the reference density (1 gcm^{-3}), and k is a shape factor, which is 1.0 in the case of a sphere. Because of the effect of the particle density on the aerodynamic diameter, a spherical particle of density > 1 gcm^{-3} will have a larger aerodynamic diameter than its geometric diameter. However, the density for most substances is less than 10 so that the difference between the geometric and aerodynamic diameter as of a spherical particle is less than a factor of ~ 3.

Another definition of equivalent diameter is the Volume Equivalent diameter which is the diameter of a spherical particle with the same density having the same volume as the given non-spherical particle. The Stokes diameter is a diameter of a sphere having the same terminal settling velocity and density as the particle. For a spherical particle, the Stokes diameter is equivalent to the actual physical diameter ($D_P = D_{ST}$) [13]. It is important to note that various types of aerosol instrumentation report different measures of particle diameter depending on the employed methodology and application. Therefore, a universal measure of aerosol particle size does not exist and as a result the sizing definition will be specified for particle diameter reported in this thesis.

2.3.2 Particle Size Classification

Particle size is one of the most important parameters for characterising the behaviour of aerosols. The diameters of atmospheric aerosols span over four orders of magnitude, from a few nanometers to around 100 μm. To appreciate this wide size range one just needs to consider that the mass of a 10 μm diameter particle is equivalent to the mass of one billion (10^9) 10 nm particles of the same composition. Atmospheric aerosols are normally classified into separate modes according to their

size, formation process and atmospheric age. The exact size ranges of these modes vary in the literature.

Based on the number, surface, and volume distributions of aerosol particles shown in Figure 2.2, four distinct groups of atmospheric particles can be defined. Particles with diameters larger than 2.5 μm are identified as the coarse mode. These particles are mainly produced by mechanical processes and are introduced directly into the atmosphere from both natural and anthropogenic sources. The most significant source is the bursting of bubbles in the ocean, which creates coarse particles of sea salt. The wind also picks up dust, soil and biological particles and suspends them in the atmosphere. Anthropogenic coarse particles are introduced into the atmosphere through the abrasion of machinery, on the surface of roads, and in industrial and agricultural processes. Because of their relatively large size, coarse particles settle out of the atmosphere in a reasonably short time by sedimentation, except on windy days, where fallout is balanced by re-entrainment.

The Aitken mode particles, extending from 0.01 to 0.1 μm diameter, are formed from ambient-temperature gas-to-particle conversion as well as condensation of hot vapours during combustion processes. These particles act as nuclei for the condensation of low vapour pressure gaseous species, causing them to grow into the accumulation range. The lifetime of these particles is short, as they are lost principally by coagulation and growth into larger particles. The Aitken and accumulation mode particles are referred to collectively as fine particles.

Particles with diameters between 0.1–2.5 μm are considered as the accumulation mode representing a region of particle growth mainly due to the coagulation of particles with diameters smaller than 0.1 μm and from condensation of vapours onto existing particles, causing them to grow into this size range. They can also be introduced directly into the atmosphere, mainly through the incomplete combustion of wood, oil, coal, gasoline and other fuels. Because of the nature of their sources, particles in the accumulation size range generally contain substantial amounts of organic material as well as soluble inorganic ions such as ammonium, nitrate and sulphate. The accumulation mode is so named because particle removal mechanisms are least efficient in this regime, causing particles to accumulate there until they are ultimately lost through rain or other forms of precipitation (wet deposition).

The final type of particles is that of the size range smaller than 0.01 μm (not shown in figure 2.2) and is known as the ultra-fine particle size range. They are thought to be generated by gas to particle conversion processes that are not well understood on a molecular level. Because of their very small size and mass, they are difficult to study given the available measurement techniques. These particles have been observed in bursts of very large numbers in the presence of either biogenic or anthropogenic emissions under favourable local conditions in many different environments including forests [18] and coastal zones [19] and have been referred to as the nucleation mode. These particles are only observed as a distinct mode at their source and have a very short lifetime, sometimes on the order of minutes, due to their rapid coagulation or random impaction onto surfaces.

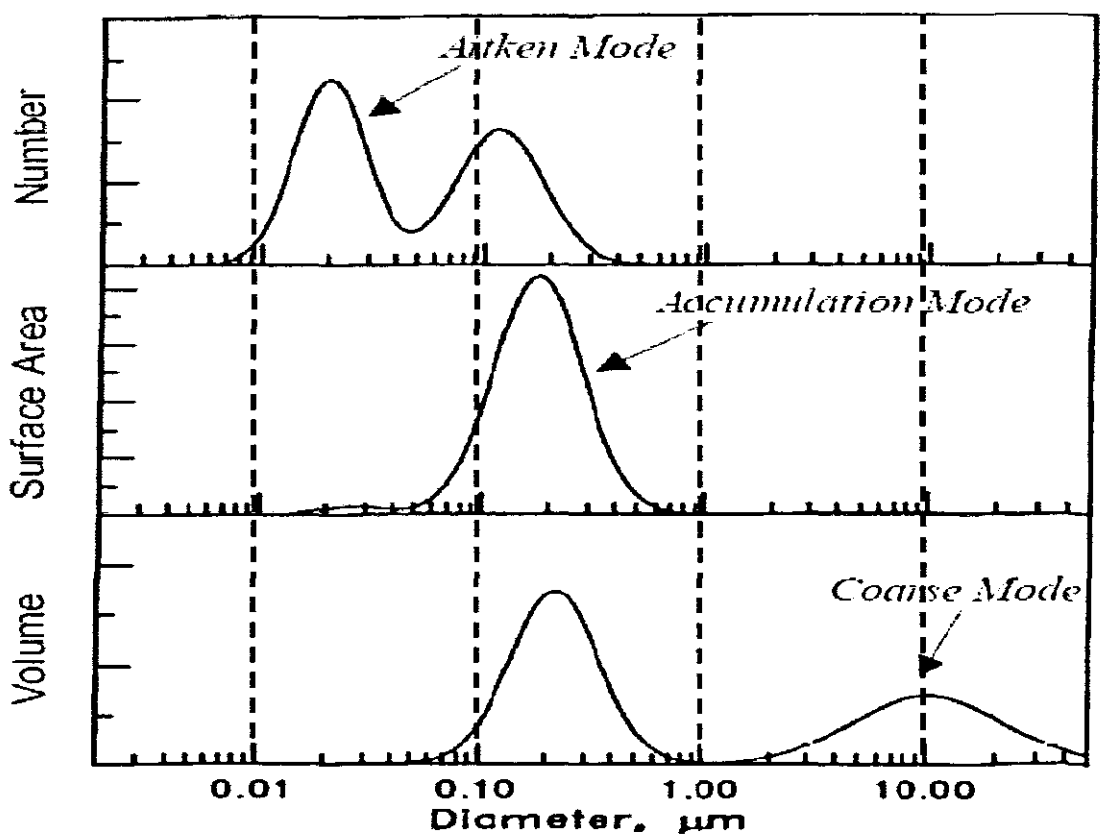

Figure 2.2: Illustration of number, surface, and volume distributions for a typical urban model aerosol adapted from Seinfeld and Pendis. **[13]**

The nucleation and Aitken mode particles account for the majority of atmospheric particles by number, but due to their small sizes, they rarely account for more than a few percent of the total mass. Hence if the toxicological effects are determined

primarily by the number of particles, rather than their mass, these small particles could ultimately prove to be of high importance. The accumulation mode particles account, generally, for a significant fraction of the total aerosol mass and have the greatest surface area. This makes these particles of significant importance to gas phase deposition and atmospheric heterogeneous chemistry. Most of the aerosol mass is usually found in the coarse mode, where large particles contribute significantly to the optical properties of atmospheric aerosols. These modes, in general, originate separately, are transformed separately, and are removed from the atmosphere by different mechanisms, have different lifetimes, have different chemical composition, have different optical properties, and differ significantly in their deposition patterns in the respiratory tract. Therefore, the distinction between nucleation, Aitken, accumulation and coarse particles is a fundamental one in any discussion of the physics, chemistry, measurement, or optical and health effects of aerosols.

2.3.3 Aerosol Chemical Composition

Understanding the formation, composition and behaviour of ambient aerosol particles is of critical importance in order to better quantify the effects of aerosols on visibility, human health and global climate. To date, the impact of aerosol particles on climate is poorly quantified, and the compounds that contribute to adverse health effects have not been accurately established (see section 2.2). This is partly due to the fact that the chemical composition of ambient aerosol particles has not been fully characterised, in particular its organic fraction. Atmospheric aerosols are generally composed of variable amounts of sulphate, ammonium, nitrate, sodium, chloride, trace metals, crustal elements, water and carbonaceous material. The sulphate component is derived predominantly from the atmospheric oxidation of anthropogenic and natural sulphur-containing compounds such as sulphur dioxide (SO_2) and dimethyl sulphide (DMS), respectively. Nitrate is formed mainly from oxidation of atmospheric nitrogen dioxide (NO_2). A large fraction of NO_2 is in turn the result of the oxidation of NO to NO_2. Sulphate and nitrate are initially formed as sulphuric (H_2SO_4) and nitric acids (HNO_3), but are progressively neutralised by atmospheric ammonia forming the corresponding ammonium salts. The main source of chlorides is sea spray even at the locations of hundreds of kilometres from the coast. Chlorides also enter atmospheric particles as a result of ammonia neutralisation of hydrochloric acid

(HCL) vapour, which is emitted from sources such as incinerators and power stations. Crustal materials include soil dust and windblown minerals. They vary in composition according to local geology and surface conditions and reside mainly in the coarse particle fraction. The carbonaceous fraction of the aerosols consists of both elemental and organic carbon. Elemental carbon (EC), also called black carbon, graphitic carbon, or soot, is emitted directly into the atmosphere, predominantly from combustion processes. While particles containing organic carbon (OC) (for example, polycyclic aromatic hydrocarbons, (PAHs) can be directly emitted into the atmosphere (i.e. from primary sources such as biomass burning and combustion processes), they can also be introduced by secondary organic aerosol (SOA) formation. The latter process occurs when volatile organic compounds undergo atmospheric oxidation reactions, forming products that have low enough volatilities to form aerosols via either nucleation or gas-to-particle partitioning to pre-existing particles [20]. Volatile organic compounds (VOCs) are emitted into the atmosphere from anthropogenic vaporisation of volatile organic petroleum products, solvents, from storage distribution system and due to incomplete combustion of fossil fuels and biogenic sources [13]. Biogenic VOC sources include organics such as isoprene, monoterpenes and sesquiterpenes. Aromatics as well as monoterpenes are particularly important constituents of urban and regional atmospheric chemistry and most have been identified as SOA precursors [21].

Understanding the composition of the atmospheric aerosol particles is necessary for identifying their sources and predicting their effect on various atmospheric processes. Although organic compounds typically account for 10-70 % of the total dry fine particle mass in the atmosphere [22], their concentrations, composition and the processes that control their formation and transformation in the atmosphere are not well understood, particularly in relation to the other major fine particle constituents, i.e. sulphate and nitrate compounds. Furthermore, the contributions of the primary and secondary components of particulate organic carbon have long been difficult to quantify. This is because particulate organic matter is part of a complex atmospheric system with hundreds of different compounds, both natural and anthropogenic, covering a wide range of chemical and thermodynamic properties [23]. The presence of semi-volatile compounds complicates the sampling of organic particulate matter. In addition, there is a current lack of a single technique that is capable of analysing the entire range of organics present. The lack of a direct chemical analysis method

for the identification of the composition of organic aerosols and the separation of the primary and secondary sources has led researches to employ several indirect methods. These includes the use of tracer compound for either the primary or the secondary OC , the use of models describing the formation of secondary OC and the use of models describing the emission and dispersion of primary OC [24].

2.3.4 Other Aerosol Properties

Many of the effects of atmospheric aerosols (e.g. radiative effect) depend on their chemical composition, which rarely consists exclusively of a single component. Atmospheric aerosols are generally composed of a mixture of species from a number of sources. The mixing state, i.e. how all the components are distributed among the particles, of these components is one of the important properties of atmospheric aerosols. In an aerosol population, particles are externally mixed if they arise from different sources and have different chemical composition. On the other hand, particles are internally mixed if all particles of a given size contain a uniform mixture of components. Finally, aerosol concentration is most commonly reported in terms of mass or number of particles in a unit volume of aerosol. Common units are μgm^{-3} and number cm^{-3}, respectively. Mass concentration is equivalent to the density of an aerosol, but the latter term is not used in order to avoid confusion with particle density.

2.4 Atmospheric Aerosols and Human Health

The local impact of gaseous and particulate pollutants is gauged by the effect on pollution receptors. For example, deposition of acidic pollutants can speed up the deterioration of building materials, harm vegetation, damage the aquatic ecosystem, and cause breathing problems and even increase the mortality rate among humans [13]. Air pollution has a long history [25]. From at least 13^{th} century up to the mid 20^{th} century, documented air pollution problems were primarily associated with high concentrations sulphur oxide gases and soot particles [26]. This type of pollution is often referred to as "London Smog" because of a severe pollution episode in that city in December 1952, which led to over 4000 deaths. Moreover , the discovery of photochemical air pollution in the Los Angeles area in the mid-1940s have made high

concentrations of ozone and photochemical products and their associated impacts on human health a major issue worldwide [27].

Air quality standards for particulate matter in countries such as the United States were expressed some years ago in terms of the mass of total suspended particulate matter (TSP). The standard was then changed to mass of suspended particulate matter less than 10 μm in size, commonly called PM_{10}, and more recently was modified to include particulate matter less than 2.5 μm in diameter $PM_{2.5}$ [28]. The rational for basing air quality standards on smaller particles relied on the later observation that they penetrate deeper into the lung and hence the potential adverse health effect is much greater [29]. In addition, they have larger surface-to-volume ratios and are commonly produced from gas-to-particle conversion or combustion processes, which are known to produce carcinogens such as polycyclic aromatic hydrocarbons. Many epidemiological studies have observed associations between particulate air pollution and human health [30]. For example, an increase of 1.5 % in the total daily mortality with an increase of 10 μgm^{-3} in $PM_{2.5}$ concentration has been reported [31]. Daily time series studies have observed associations between daily mortality and changes in particulate air pollution [32]. Elevated air pollution has been associated with declines in lung function and increases in respiratory symptoms [33]. Fine particulate matter was associated with lung cancer and cardiopulmonary mortality [4]. Each 10 $\mu g/m^3$ elevation in fine particulate air pollution was associated with approximately a 6 %, and 8 % increased risk of cardiopulmonary and lung cancer mortality, respectively. On the other hand measures of coarse particle fraction and total suspended particles were not consistently associated with mortality [31].

It was widely believed that in the short term air pollution only anticipates unavoidable deaths. Recent studies have shown, however, that this is not the whole story, and that when air pollution increases, the excess mortality due to the anticipated deaths of particularly vulnerable people-called harvesting- is not followed by a deficit [34]. This implies that air pollution not only kills people in a 'high risk pool", but also recruits new individuals to that pool. This is consistent with the results of a study, which showed that short-term inhalation of fine particulate air pollution and ozone at concentrations that occur in the urban environment causes acute conduit artery vasoconstriction in healthy adults [35].

There are too many plausible mechanisms and too few established facts to explain these epidemiological studies [36]. What is particularly interesting from a chemical point of view, however, is that most of the cities included in these studies are quite disparate in terms of location and the type of air pollutants that would be expected to predominate in each region, yet a consistent relationship between adverse health effects and particulate pollution is found. This suggests either that there is a general inflammatory response to inhalation of such particles, which is independent of their specific chemical composition or that there are some common chemical components responsible for the effect. The UK department of health Committee on the Medical Effects of Air pollution concluded that no known chemical substance is of sufficient toxicity given the current level of exposure to particulate matter to explain the observed magnitude of health effects [37].

It is difficult, however, to imagine that the chemical composition does not play a role. Chemical components of the atmosphere are highly diverse. They range from near neutral and highly soluble substances such as ammonium sulphate, ammonium nitrate and sodium chloride through sooty particles made up largely of elemental carbon coated in organic compounds, and essentially insoluble minerals such as particles of clay. Evidence is being presented that trace metals influence the toxicity of airborne particulate matter. Such evidence derives from the toxicological rather than the epidemiological studies and depends mechanistically on the idea that metals are redox-active and can, therefore, induce or catalyse chemical change leading to production of free radicals such as the hydroxyl radical, which have a known ability to cause tissue inflammation [38]. In addition, toxicological studies found that ultra fine particles of less than 100 m appear to have considerably enhanced toxicity per unit mass and that their toxicity increases as particle size decrease [34]. This may be explained either through a greater surface area per unit mass if the toxic components reside solely or partially in the surface of the particles, or via the ability of ultra fine particles to penetrate the pulmonary interstitium [39]. Sieggmann et al [1999] suggested that particles with a diameter below 1 μm act as vehicles transporting toxic chemicals into the human respiratory system [40]. Such findings and suggestions are interesting, but yet far from conclusive. One of the major issues is whether the toxicity of the particles resides in some particular fraction of the particles as defined by the chemical composition, particle size, or surface reactivity [41].

2.4.1 Air Pollution and associated Human Health Outcomes

In urban environments poor visibility is attributed mainly to $PM_{2.5}$. This aersol size fraction is also responsible for respiratory and cardiovascular dieases due to its ability to penetrate through the lungs. Therefore visibility degradation is a good indicator of poor air pollution conditions which is linked adverse health effects. The studies below reveals the health effects associated with air pollution.

Particulate matter and general mortality

There are numerous studies that link exposure to particulate matter with increase in mortality. Pope et.al., (1995) [28] using data from surveys of American Cancer Society volunteers from 151 U.S. metropolitan areas, found a relative risk ratio for mortality from all causes of 1.17 (1.09 to 1.26) for an increase in $PM_{2.5}$ of 1 μgm^{-3}. A later analysis (Schwartz *et al.*, 1996) specifically considers the effect of the fine ($PM_{2.5}$) versus the coarse (PM_{10}-$PM_{2.5}$) fraction. In this study PM_{10}, $PM_{2.5}$, PM_{10} - $PM_{2.5}$ and sulphate concentrations from the "six cities" study were analyzed. PM_{10}, $PM_{2.5}$ and sulphate particles were all significantly associated with increased daily mortality. No association was found with the course (PM_{10} -$PM_{2.5}$) fraction. The most significant association was found with $PM_{2.5}$ with a 1.5 % increase in daily mortality per 10 μgm^{-3} increase in the two day mean $PM_{2.5}$ concentration (95 % CI, 1.1 % to 1.9 %). Researchers in England found that a 10 μgm^{-3} increase in PM_{10} was associated with a 1.1 % increase in mortality for all causes, as well as with a 5 % increase in death due to chronic obstructive pulmonary disease and a 1.7 % increase in deaths from circulatory diseases [29]. Woodruff et.al., 1997 [42] obtained data on almost 4 million infants from 86 U.S. metropolitan areas, and the infants PM_{10} exposures during the first two months of life were classified as high, low or medium using ambient monitoring data (PM_{10} range 11.9-68.8 μgm^{-3}). In normal birth weight infants, high PM_{10} exposure was associated with death from respiratory causes (OR 1.40, 95 % CI 1.05, 1.85) and sudden infant death syndrome (OR 1.26, 95 % CI: 1.14, 1.39). An increased in death from respiratory causes also found in low birth weight infants, though not statistically significant.

Cardiovascular and respiratory mortality

Four of the studies used in Dockery and Pope's review provided a breakdown of mortality by broad cause of death categories. Deaths due to cardiovascular causes had effect estimates ranging from 0.8 % and 1.8 % (95 % CI) for each 10 μgm^{-3} increase in PM_{10} concentrations above 20 μgm^{-3}. Respiratory deaths had effect estimates between 1.5 % and 3.7 % increase for each 10 μgm^{-3} increase in PM_{10}. In all four studies no associations were found with cancer mortality or with other causes.

The increased estimates of effects for respiratory and cardiac causes of death would imply that populations sensitive to the effects of increases in PM_{10} concentrations would include those with pre-existing lung and heart diseases [43]. Dockery and Schwartz (1993) identified individuals over the age of 65 as a sensitive subgroup. While there appears to be a correlation between cardiovascular death and PM_{10} concentrations the cause of this has been unclear. In a recent study by Pope et.al., 2002 [44], long-term particulate matter exposures were most strongly associated with mortality attributable to ischemic heart disease, dysrhythmias, heart failure, and cardiac arrest. For these cardiovascular causes of death, a 10 $\mu g/m^3$ elevation in the fine particulate matter was associated with 8 % to 18 % increases in mortality risk, with comparable or larger risks being observed for smokers relative to nonsmokers. Ostro et.al, 2006 [45] examined the associations between $PM_{2.5}$ and daily mortality in nine heavily populated California counties using data from 1999 through 2002. In this study they considered daily counts of all-cause mortality and several cause-specific subcategories (respiratory, cardiovascular, ischemic heart disease, and diabetes). Their analysis revealed associations of $PM_{2.5}$ levels with several mortality categories. Specifically, a 10 μgm^{-3} change in 2-day average $PM_{2.5}$ concentration corresponded to a 0.6 % (95 CI: 0.2 -1.0) increase in all-cause mortality, with similar or greater effect estimates for several other subcategories, including respiratory and cardiovascular.

Lung cancer

Epidemiological studies over the last 40 years have observed that general ambient air pollution, chiefly composed of the by-products of the incomplete combustion of fossil fuels, is associated with small relative increases in the incidence of lung cancer [46].

The evidence derives from studies of trends in the incidence of lung cancer, and cohort studies using diverse exposure metrics. In a recent cohort study by pope et al [42], fine particulate and sulphur oxide–related pollution were associated with all-cause, lung cancer, and cardiopulmonary mortality. Each 10 μgm^{-3} elevation in fine particulate air pollution was associated with approximately 8 % increased risk lung cancer mortality. A recent Swedish case–control study reported that excess lung cancer was related specifically to exposure to mobile sources of air pollution, with the largest effects observed for exposure occurring 20 years prior to diagnosis [47].

Zanobett et.al, 2000 [48] examined the association between particulate matter PM_{10} and hospital admissions for lung and heart diseases in ten US cities. They found 2.5 % (95 % CI: 1.8 -3.3) increase in chronic obstructive pulmonary disease, 1.95 % (95 % CI: 1.5-2.4) increase in Pneumonia, and a 1.27 % increase (95 % CI: 1 -1.5) in Cardiovascular disease for a 10 μgm^{-3} increase in PM_{10}. They report that the results where stable when controlling for confounding by SO_2, O_3 and CO

Respiratory hospital admissions

A number of studies have assessed the effect of pollution on morbidity by considering increases in hospital admissions. In the US, Canada and Europe, association between daily concentrations of PM_{10} and daily hospital admissions for cardiovascular and respiratory disease were reported for close to 100 cities [49]. In another study, Schwartz et.al, 1996 [29] investigated the relationship between PM_{10} and carbon monoxide (CO) and cardiovascular hospital admissions in Tuscon. Tuscon was chosen because of its low SO_2 concentrations and because the PM_{10} concentrations peak during the winter when ozone concentrations are lowest. Both PM_{10} and CO were associated with increased risk of cardiovascular hospital admissions for the study group, which consisted of persons less than 65 years old. During the period of study a total of 14,665 cardiovascular admissions occurred in this age group. Admissions increased by 2.75 % per 23 μgm^{-3} increase in PM_{10} (95 % CI). In a recent study, Hurley et.al., 2005 [50] used all-ages data both for concentration–response function and for background rates, derived from the APHEIS programme report [51]. These were also based on eight European cities. Together they implied an annual rate of attributable emergency respiratory hospital admissions = 7.03 (95 % CI 3.83–10.30) per 10 $\square gm^{-3}$ increase in PM_{10} per 100 000 people (all ages).

Another study linked PM_{10}, CO, NO_2, and O_3 with hospital admissions for cardiopulmonary illnesses in Los Angeles during. Co showed the most consistently significant ($p < 0.05$) relationship to cardiovascular disease. In addition pulmonary disease admissions associated more with NO_2 and PM_{10} than with CO.

Asthma

A study conducted in Seattle, Washington on the effects of ambient air pollution on symptoms of Asthma found significant associations between change in short-term air pollution levels indexed as Particulate Matter, and the occurrence of Asthma symptoms among children. In this study of 133 children aged between 5-13 years for an average of 58 days (range 28-112 days) using single pollutant models, the population average estimates indicated an 18 % (95 % CI, 5-33 %) increase for a 10 μgm^{-3} increment in same-day particulate matter < 1.0mm ($PM_{1.0}$), and an 11 % (95 % CI, 3-20 %) increase for a 10 μgm^{-3} increment in particulate matter < 10 mm (PM_{10}) lagged 1 day. Conditional on the previous day's asthma symptoms, we estimated 14 % (95 % CI, 2-26 %), and 10 % (95 % CI, 3-16 %) increases in the odds of asthma symptoms associated with increases in $PM_{1.0}$ and PM_{10} respectively. In addition, they found no association between sulfur dioxide (SO_2) and the odds of asthma symptoms. In Los Angeles, California, PM_{10} exposure was associated with daily reporting of cough, shortness of breath and wheeze among African-American children with current, physician-diagnosed asthma [52]. Also in Southern California, PM_{10} exposure from August to October 1995 was associated with asthma symptoms (cough, wheeze, sputum production, shortness of breath, or chest tightness) in panel of 24 asthmatics aged 9-17 years [53]. In another study of 75 physician-dignosed asthmatic children, 6-13 years old, in Port Albemi, British Columbia, PM_{10} exposure was associated with increases in both phlegm, and decreased peak flow [41].

Restricted activity days (RAD)

Most major health impact assessments of air pollution and health include estimates of the effect of air pollution on days when normal activities are restricted; typically using concentration–response functions derived from [54] or [55]. Within USNHIS (United States National Health Interview Survey), restricted activity days (RADs) are classified according to severity as (*a*) bed disability days; (*b*) work or school loss

days; and (*c*) minor restricted activity days (MRADs), which do not involve work loss or bed disability, but do include some noticeable limitation of "normal" activity.

Ostro et.al, 1999 [56] studied both RADs and work loss days(WLDs) among adults aged 18–64 years in separate analyses for each of the six years 1976–1981. Results for RADs, based on about 12 000 subjects per year from 68 metropolitan areas, showed a consistent relationship with $PM_{2.5}$: the coefficient for each of the six years was positive and highly statistically significant (P <0.01). A weighted mean coefficient was linked to estimated background rates of an average of 19 RADs per person per year to give an estimated impact function of: Change of 902 RADs (95 % CI 792–1013) per 10 □gm^{-3} $PM_{2.5}$ per 1000 adults at age 15–64. In the main analyses of CAFE CBA, this impact function was applied to people aged 15–64 years, the original study. In sensitivity analyses, the same as in impact function was used but applied to all ages, on the grounds that it is unlikely that health-related restrictions on activity do not cease at age 65. Fairly recently, Hurley et.al., 2005 [48] also derived impact functions for WLDs from Ostro, 1987 [52] and MRADs from Rothschild, 1989 [53] to give, respectively: Change of 207 WLDs (95% CI 176–238) per 10 □gm^{-3} $PM_{2.5}$ per year per 1000 people aged 15–64 in the general population and Change of 577 MRADs (95 % CI 468–686) per 10 □gm^{-3} $PM_{2.5}$ per year per 1000 adults aged 18–64.

Studies on respiratory effects in children

Dockery et.al, 1993 [4] provided evidence that rates of respiratory illnesses and symptoms are elevated for children living in cities with high particulate pollution. In their study, rates of chronic cough, bronchitis, and chest illness during the 1980-1981 school years were positively associated with all measures of particulate pollution (TSP, PM_{15}, $PM_{2.5}$, and fine fraction aerosol sulphate). They were also positively, but less strongly, associated with concentrations of the two gases SO_2 and NO_2. Frequency of earache was also positively associated with particulate concentrations but no association was found with asthma, persistent wheeze, hay fever, or non-respiratory illness. Results from this study also suggested that increased rates of illness were not associated with permanent loss of pulmonary function. However, further data is needed on the long-term effects of air pollution on lung function and the later development of respiratory disorders.

Cost of health effects of PM_{10}

Dockery and Pope, 1994 reviewed a number of studies with quantified health effects associated with increases in PM_{10}. These indicated increases in daily mortality ranging from 0.5 to 1.5 % (weighted average 1 %) per 10 μgm^{-3} increase in daily PM_{10} concentrations greater than 20 μgm^{-3} [57]. As indicated earlier the presence of a threshold below which there are no observable adverse effects is not conclusive with many studies concluding that no such lower limit has been adequately determined across a range of studies. Notwithstanding this the Dockery and Pope (1994) review has been used to assess the potential health effects associated with particulate pollution based on a no effects threshold of 20 μgm^{-3}. Schwartz et.al, 1996 [29] suggests that while no threshold level appears to exist there is only meagre evidence to support occurrences of effects below a PM_{10} concentration of 20 μgm^{-3}. Dockery and Pope [54] also reviewed the percentage of deaths attributed to cardiopulmonary and respiratory causes. Increases in cardiopulmonary and respiratory deaths associated with a 10 μgm^{-3} increase in PM_{10} ranged from 0.8 to 1.8 % (weighted average 1.4 %) and 1.5-3.7 %(weighted average 3.4 %) respectively. Studies reviewed by Dockery and Pope (1994) quantifying increases in other health effects indicated the following weighted averages for health effects per 10 μgm^{-3} increase in daily PM_{10} concentrations greater than 20 μgm^{-3}: 0.8 % increase in hospitalizations for respiratory illnesses, 1 % increase in emergency room visits for respiratory illnesses, 3.4 % increase in emergency room visits for asthma, 1.9 % increase in hospitalizations for asthma.

The American Lung Association (1995) used a selection of quantitative studies of the health impacts relative to particulate concentrations to assess the cost to society associated with suspended particulate concentrations. Their report indicated that nearly $11 billion US would be saved annually if nation-wide suspended particulate pollution was reduced to meet a standard of 50 μgm^{-3} averaged over 24-hours and annual average of 30 μgm^{-3} [58].

2.5 Atmospheric Aerosols and Global Climate

In their 2001 report, the Intergovernmental Panel on Climate Change (IPCC) concluded that emissions of greenhouse gases and aerosols due to human activities continue to alter the atmosphere in ways that are expected to affect the climate [59]. Greenhouse gases warm the Earth and sulphate aerosols cool it down [11], because aerosol particles in the atmosphere scatter sunlight back into space, reducing the energy that the planet absorbs, keeping it cooler. However, aerosol particles in the real world may also lead to heating of the atmosphere if they contain light absorbers such as elemental carbon and mineral dust [60]. In fact, it was proposed that the warming effect from black carbon in aerosols may balance the cooling effect of the sulphate component, the largest single contributor to aerosol cooling [2]. Scattering and absorbing the solar radiation is known as the "direct" effect of aerosols on the global climate, which can lead to either cooling or warming of the atmosphere depending on the proportion of light scattered to that absorbed.

Aerosols also have an "indirect" effect on climate by altering the properties of clouds, resulting in a change of their scattering properties and longevity [61]. It is very difficult to form cloud droplets without small aerosol particles acting as "seeds or nuclei" to start the formation of cloud droplets. As aerosol concentration increases within a cloud, the water in the cloud gets spread in many more droplets, each of which is correspondingly smaller [62]. This has two consequences: clouds with small droplets reflect more sunlight, and such clouds last longer, because it takes more time for small droplets to coalesce into droplets that are large enough to fall into the ground. The minimum droplet size for rainfall to occur is 18 μm. The latter effect has been supported by certain observations indicating that aerosols from forest fires and urban air pollution can suppress rain and snow fall [60]. In this way, changing aerosols in the atmosphere can change the frequency of cloud occurrence, cloud thickness, and rainfall. These changes in cloud droplet's number concentration and size and their longevity are, respectively, known as the "first" and "second" indirect effects of aerosol on climate and they are both believed to increase the amount of sunlight that is reflected into space without reaching the Earth's surface, resulting in a cooling effect.

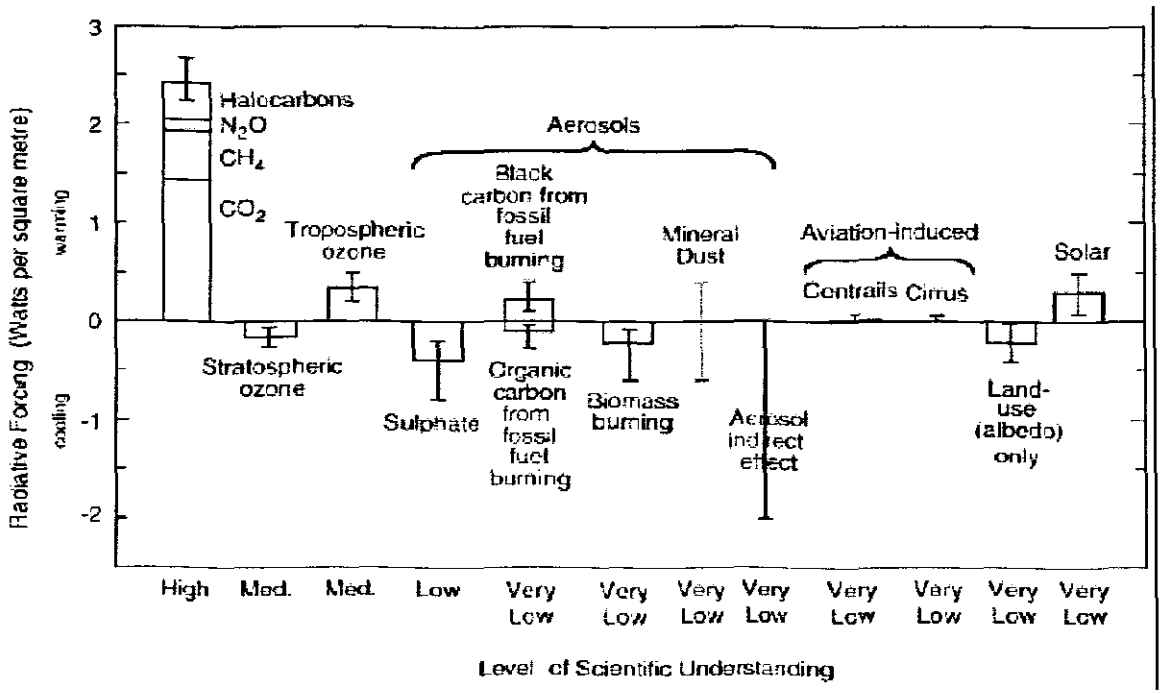

Figure 2.3: The global mean radiative forcing of the climate system for the year 2000, relative to 1750. Also shown are the external factors and their estimated radiative forcing on the global energy balance (source www.ipcc.ch).

Figure 2.3 summarises the state of scientific knowledge of the effects of various external factors on the global climate as reported by the Intergovernmental Panel on Climate Change (IPCC) [57]. The figure presents the global, annual mean radiative forcing due to a number of factors for the period from pre-industrial time to a recent year (1750-2000). Radiative forcing is a measure of the influence a factor has in altering the balance of incoming and outgoing energy in the Earth-atmosphere solar - system, and is an index of the importance of the factor as a potential climate change mechanism. It is expressed in Watts per square meter, Wm^{-2} [59]. The heights of the rectangular bars denote central or best estimates of the contributions of these forces some of which yield warming, and some cooling, while its absence denotes no estimate possible at present. The vertical line about the rectangular bars indicates a range of estimates, guided by the spread in the published values of the forcings and physical understanding. All the forcings shown have distinct spatial and seasonal features such that the global, annual means appearing on this plot do not yield a complete picture of the radiative perturbation. Some of the forcings possess a much greater uncertainty than others. For example, because of their long lifetimes, the principal greenhouse gases (e.g. CO_2) are well mixed over the globe thereby perturbing the global heat balance. Aerosols, on the other hand, represent

perturbations with stronger regional influences because of their spatial distribution, which prevents a simple sum of positive and negative effects to be expected to yield the net effect on the global climate system. Models have been used to estimate the direct radiative forcing for five distinct aerosol species. The global annual mean radiative forcing is estimated to be -0.4 W m^{-2} for sulphate, -0.2 W m^{-2} for biomass burning aerosols, -0.1 W m^{-2} for fossil fuel organic carbon and +0.2 W m^{-2} for fossil fuel black carbon aerosols and in the range -0.6 to +0.4 W m^{-2} for mineral dust aerosols. The level of scientific understanding for sulphate aerosol is low while for biomass burning, fossil fuel organic carbon, fossil fuel black carbon, and mineral dust aerosols the level of scientific understanding is very low. The sign of the effects due to mineral dust aerosols is itself an uncertainty [63].

The indirect aerosol radiative forcing through their effect on clouds is believed to have a cooling effect, although of very uncertain magnitude. Models have been used to estimate the "first" indirect effect of anthropogenic sulphate and carbonaceous aerosols (namely, a reduction in the cloud droplet size at constant liquid water content) yielding global mean radiative forcings ranging from -0.3 to -1.8 W m^{-2}. The lack of the best estimate for this effect is due to the large uncertainties in understanding aerosol and cloud processes and their parametisations in models, the incomplete knowledge of the radiative effect of black carbon in clouds, and the possibility that the forcings of individual aerosols types may not be additive [64]. The "second" indirect effect of aerosols (their effect on cloud lifetime, which is believed to also lead to a negative forcing) is conceptually important, but there exists very little confidence in the simulated quantitative estimates and therefore it is not shown in Figure 2.3

This summary confirms that there is lack of confidence in quantifying the total aerosol direct and indirect effects on the global climate than that for the greenhouse gases. This is likely because the radiative forcing of aerosols differs from that of greenhouse gases in several important ways [11]. Unlike the gases, aerosol particles are relatively short lived in the troposphere, resulting in spatial and temporal non-uniformity of forcing. Aerosol forcing is greatest in daytime and in summer, whereas greenhouse gas forcing acts over the full diurnal and seasonal cycles. Unlike gases whose sunlight absorption varies from one molecule to the other, the single particle optical properties of aerosol particles depend on particle size and composition. These

differences make it difficult to treat the radiative influences of aerosols compared to that of greenhouse gases. Aerosols have most likely made a significant negative contribution to the overall radiative forcing, but cannot be considered simply as a long-term offset to the warming influence of greenhouse gases. This discussion suggests that scientist have a lot to learn about the way aerosols affect regional and global climate.

2.6 Optical effects of Aerosols

Aerosols are directly responsible for the reduction of visible light in the atmosphere. Atmospheric pollutants (aerosols and gases) achieve visibility reduction by absorbing or scattering of visible light. This phenomenon of light extinction due to absorption and scattering by aerosols and gases is described in depth in Chapter 3. Chapter 3 also provides a method for the quantification of light extinction as well as translation of quantified light attenuation into a visibility measurement. Digital Image Processing is also discussed as a viable method of measuring real-time visibility.

Chapter 3: Aerosols and Visibility Reduction

3.1 Factors affecting Visibility in the Atmosphere

3.1.1 Optical Properties of Aerosols and Gases

When solar radiation enters the Earth's atmosphere, a part of the incident energy is removed by scattering and a part by absorption. Both gases and particles scatter and absorb radiation and contribute to the light extinction coefficient (b_{ext}) of the atmosphere such that:

$$b_{ext} = b_{sp} + b_{ap} + b_{sg} + b_{ag} \tag{3.1}$$

where b_{sp} and b_{ap} refer to scattering and absorption of light by particles, and b_{sg} and b_{ag} refer to scattering and absorption by gases (all are wavelength dependent). The scattered radiation is often referred to as diffuse radiation, with a portion going back to space and a portion reaching the ground. The net radiation that arrives at the ground without being scattered or absorbed is called direct radiation. The following subsections describe all the four components of the light extinction coefficient.

Gas Scattering

An extinction coefficient, $b_{scat,g,\lambda,q}$ for a gas q and incident radiation wavelength λ may similarly be defined for the attenuation of light due to gas scattering [2]:

$$b_{scat.g.\lambda.q} = N_q A_{scat}(\lambda) \tag{3.2}$$

where N_q is the number concentration of gas q molecules (molecules cm^{-1}) and A_{scat} is the scattering cross-section of the gas molecule. The only important gas scattering process is Rayleigh scattering, the scattering of light by gas molecules (primarily N_2 and O_2) with molecular radius much smaller than light wavelengths. That is, a Rayleigh scatterer has a molecular radius r much smaller than visible wavelength λ = 0.38 to 0.75 μm; $2\pi r/\lambda << 1$. Therefore, the gas extinction coefficient given by equation (3.2) is due to Rayleigh scattering of incident radiation by air molecules.

The scattering cross-section due to air may be estimated from [2]:

$$A_{scat,air} = \frac{32\pi^3(n_{air,\lambda}-1)^2}{3\lambda^4 N_{air,o}^2} f(\delta) \tag{3.3}$$

where $n_{air,\lambda}$ is the real index of refraction of air for wavelength λ, $N_{air,0} = 2.55 \times 10^9$ molecules cm^{-3} is the number concentration at standard temperature and pressure (288 K, 1 atm) and $f(\delta)$ 1.05, the anisotropic correction term.

An empirical equation for the real index of refraction as a function of wavelength is [2]:

$$n_{air,\lambda} = 1 + 10^{-8}\left(8342.13 + \frac{2406030}{130-\lambda^{-2}} + \frac{15997}{38.9-\lambda^{-2}}\right) \tag{3.4}$$

Equations (3.2, 3.3 and 3.4) may be used to estimate the $b_{scat,\ air}$, the scattering extinction coefficient for air at a given wavelength, at a given number density, temperature and pressure.

Gas Absorption

Light absorption by gases in the visible spectrum is due to three atmospheric gases namely nitrogen dioxide (NO_2) and Ozone (O_3) and nitrate (NO_3). Nitrogen dioxide appears yellow, brown or red because it absorbs blue light preferentially and green light to a lesser extent. Absorption by ozone is relatively weak in the visible spectrum and concentrations of the nitrate radical are relatively low, except when sunlight is absent. Most visibility degradation studies have focused their attention in remote areas due to concerns over the viewing of scenic vista [65]. In urban areas however, ozone is the main contributor to the formation of photochemical smog and hourly ozone concentrations are frequently even higher than nitrogen dioxide hourly concentration levels. In such environments it becomes imperative to apportion ozone also as a contributor to light absorption. Therefore this work will include the study of the effects of ozone on the extinction coefficient and try to estimate its absorption efficiency using multiple regression methods.

Table 3.1: Of the gases listed in this table, only ozone, nitrogen dioxide and nitrate absorb in the visible spectrum (λ = 0.38 to 0.75 μm) [2]

Gas	Absorption Wavelengths (μm)	Gas	Absorption Wavelengths (μm)
N_2	<0.1	N_2O_5	<0.38
O_2	<0.245	HNO_3	<0.33
O_3	0.17-0.35, 0.45-075	HO_2NO_2	<0.33
CO_2	<0.21	HCHO	0.25-0.36
H_2O	<0.21	CH_3CHO	<0.345
H_2O_2	<0.35	$CH_3CO_3NO_2$	<0.30
NO_2	<0.71	HCL	<0.22
N_20	<0.24	$CFCL_3$	<0.23
NO_3	0.41-0.67	CF_2CL_2	<0.23
HONO	<0.4	CH_3CL	<0.22

The gas absorption extinction coefficient $b_{abs,g,\lambda}$ for a gas q is the product of the number concentration of the gas N_q (subscript q for a gas q) and the absorption cross-section of the gas $A_{abs,\,q}$. $A_{abs,q}$ is a function of incident wavelength and absolute temperature T [2]:

$$b_{abs,g,\lambda,q} = N_q A_{abs,q}(\lambda, T) \tag{3.5}$$

the units of N_q are molecules cm^{-3} and those of A_q are cm^{-2}.

Thus, the gas absorption extinction coefficient $b_{abs,g,\lambda,q}$ with units of $length^{-1}$ (cm^{-1}, m^{-1} or km^{-1}) is a function of the absorbing gas, the wavelength of the incident light and the absolute temperature.

The absorption cross-section of the gas A_q is the effective cross-section of the gas that results in radiance reduction through a column of gas of known path length and number concentration.

The gas absorption extinction coefficient $b_{abs,g,\lambda,}$ for a wavelength λ, due to all gases in the atmosphere is the sum of the extinction coefficients [2]:

$$b_{abs,g,\lambda} = \sum_q b_{abs,g,\lambda,T} = \sum_q N_q A_q(\lambda\lambda T) \tag{3.6}$$

Particle Absorption and Scattering

Particle absorption and scattering extinction coefficients can be modeled as [2]:

$$b_{a,a,\lambda} = \sum_{i=1}^{N_B} n_i A_{a,a,i,\lambda} \quad \text{and} \quad b_{s,a,\lambda} = \sum_{i=1}^{N_B} n_i A_{s,a,i,\lambda} \tag{3.7}$$

respectively, where n_i is the number concentration of aerosols of a given size (particles cm^{-3}), N_B is the number of aerosol sizes, $A_{a,a,i,\lambda}$ is the effective absorption cross section of a single aerosol, and $A_{s,a,i,\lambda}$ is the effective scattering cross-section of a single aerosol.

For spherical aerosols, the effective absorption and scattering cross sections are

$$A_{a,a,i,\lambda} = \pi r_i^2 Q_{a,i,\lambda} \quad \text{and} \quad A_{s,a,i,\lambda} = \pi r_i^2 Q_{s,i,\lambda} \tag{3.8}$$

respectively, where πr_i^2 is the actual aerosol cross-sectional area, $Q_{a,i,\lambda}$ (unit-less) is the single-particle absorption efficiency, and $Q_{s,i,\lambda}$ is the single particle scattering efficiency. The absorption and scattering efficiencies are functions of the complex index of refraction m_λ and of the size parameter [2]

$$\alpha_{i,\lambda} = 2\pi r_i / \lambda \tag{3.9}$$

The absorption/scattering efficiency strongly depends on wavelength and particle composition and the size parameter depends on the particle size and wavelength.

3.1.2 Atmospheric Conditions

Relative Humidity

Sulphates, nitrates and other hydroscopic species, form solution droplets that increase in size as a function of relative humidity (RH) [66]. Therefore, if scattering is measured at various relative humidity's, the relationship between measured scattering and hydroscopic mass can be quite non-linear. A number of authors have attempted to linearize the model, in an empirical way, by multiplying the hydroscopic species

by such factors as (1/ (1-RH) to account for the presence of water mass. However Malm and Gebhart proposed a different approach, whereby they multiplied the hydroscopic species by a relative humidity scattering enhancement factor, f (RH). Since changes in visibility effects are non-linear with increasing relative humidity, the relative humidity factor is estimated using a polynomial equation, which is obtained from fitting annual and seasonal RH data. An example of such an equation is given below:

$$f(RH) = b_0 + b_1(100/\ (100 - RH)) + b_2(100/\ (100 - RH))^2 \qquad (3.10)$$

where b_o, b_1 and b_2 are regression coefficients and are equal to 0.33713, 0.58601 and 0.09194 respectively with an R-square value of 0.93 annually. Figure 3.1 below shows a growth response visual model of an ammonium sulphate particle.

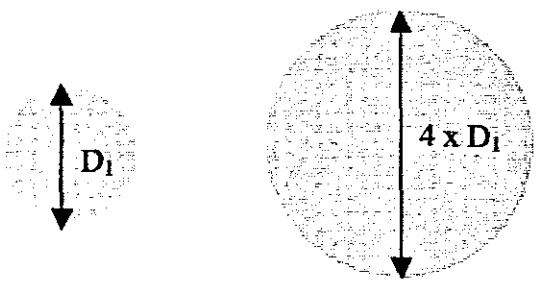

RH = 50 % RH = 90 %

Figure 3.1: Effects of water uptake on an ammonium sulphate particle as RH increases from 50 % to 90 %. The increase in diameter of the particle is approximately a factor of 4.

Gebhart and Malm noticed that measurements of hydroscopic species growth as a function of relative humidity reveal that species such as ammonium sulphate show zero growth until a relative humidity, referred to as the deliquescent relative humidity, is reached [67]. At this relative humidity increases, the species spontaneously form a solution droplet that is in equilibrium with water molecules in the ambient atmosphere. Figure 3.2 below shows that the relative humidity growth factors corresponding to relative humidity's below 40 % shows no change in growth whereas above 40 % they show a change that increases steeply in a non-linear fashion.

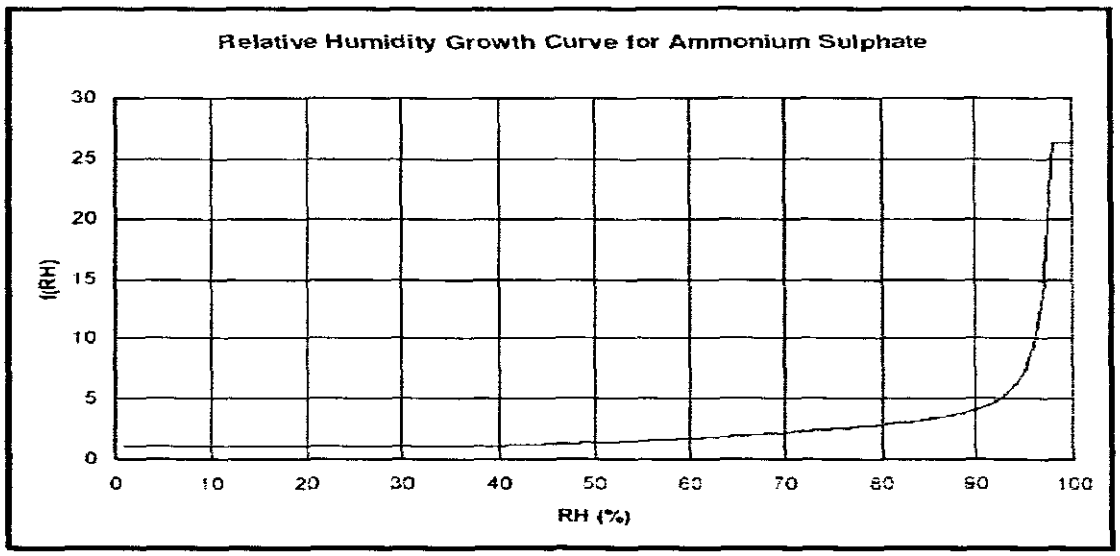

Figure 3.2: Relative humidity growth factor function f (RH) for ammonium sulphate generated using equation 3.10.

The work done by Malm and others in the derivation of relative humidity factors [*f* (RH)] appears to be the best approach in addressing the problem of hydroscopicity of fine particles. The *f* (RH) model is derived for non-ideal multi-component solutions using theoretical and semi-theoretical thermodynamic relationships for water uptake by soluble species. This work will therefore limit itself to the application of the relative humidity factors when modelling and addressing the problem of hydroscopicity by fine species such as ammonium sulphates, ammonium nitrates and soluble organic compounds.

Sun angle and cloud cover

The effect of sun angle and clouds on visibility is complex. An object is visible if the difference in brightness between it and the background (the contrast) is more than about 2 %. For example, when the sun is above and behind the observer, the sun shines on the object, making it brighter, so that it contrasts less with the background. This makes it less visible, but more detail can be seen. When the sun is behind the object, however, the object will be in shadow (relative to the observer). In this situation, the object contrasts more strongly with the background and is hence more easily visible, but the detail in the object is less visible because it is in shadow. This example shows that the direction of sunlight will influence how an object is perceived, in terms of both contrast and detail. Different conclusions could be

reached on how visible an object is depending on which method is chosen as a measure of visibility.

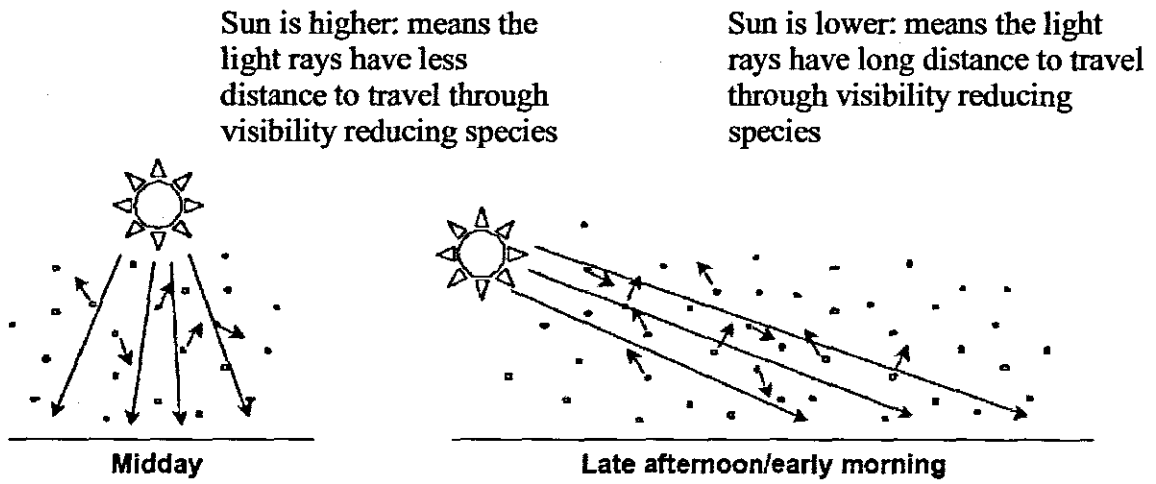

Figure 3.3: Effect of the sun angle on visibility.

In addition, even without the effect of other influences, visibility may be perceived to change during the day. In the morning and evening, haze may appear to be worse. This is partly due to the sun being lower in the sky and light having further to travel through the particles in the haze, causing more light scattering to occur [68] (see Figure 3.3). An observer's position will also affect their perception of visibility, depending on whether a haze is being viewed in the forward scatter (sun in the observer's field of view) or back scatter (sun behind the observer) mode. Particles mainly scatter light in the forward scatter direction, and therefore haze viewed in the forward scatter mode will appear brighter than haze viewed in the back scatter mode. Particle and gas concentrations, and hence the amount of light scatter, will also vary during the day due to photochemistry and meteorological conditions and those times of day when contaminants are emitted into the air.

Cloud cover affects the amount of light shining on the horizon, the foreground and any objects in the view of the observer. The particular location of the clouds also affects how objects can be seen. For example, if there are clouds behind an object being viewed, then the horizon may appear darker and the contrast between the object and the horizon less, so the object is less visible, [66]. For cities with high levels of particulate, clouds in the field of view between the object and horizon can cast a shadow over particles that would normally scatter light, and the light from the object will be easier to see [66].

Weather pattern

Warm, dry weather conditions favour secondary particle formation. They also provide suitable conditions for long-distance transportation of air contaminants. Rain washes out suspended particles, which are quickly deposited on the earth's surface. While rainfall thus acts to remedy the effects of particles on visibility, it can act as a transport mechanism for water-soluble components to enter waterways and biological processes.

3.2 Light Attenuation and Visibility Impacts

3.2.1 Interaction of Visible Light with the Atmosphere

Electromagnetic radiation, in particular visible or near visible light, interacts with the atmosphere through a number of processes - absorption, reflection, refraction, dispersion and diffraction. The scattering of light in the atmosphere occurs through a combination of several of these processes (reflection, refraction, diffraction), and is caused by both particulate matter and gases. Light scattering occurs in the forward, backward and lateral directions. The figure below (figure 3.4) shows the light scattering processes that take in a particle. Light waves D and E undergo a combination of reflection and diffraction, A and B undergo reflection and refraction respectively whereas C undergoes refraction.

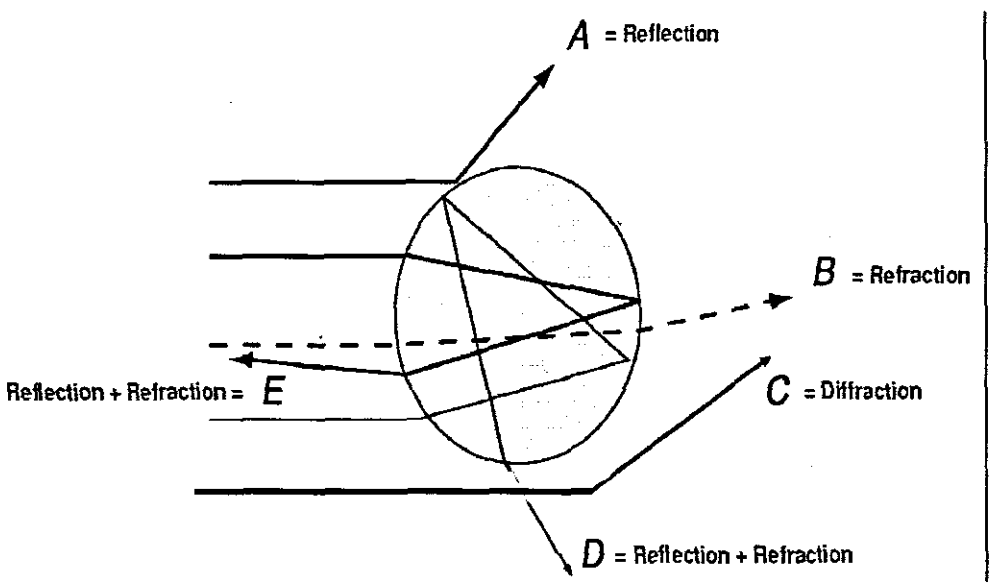

Figure 3.4: The 3 basic light scattering processes with E and D being a combination of reflection and refraction.

Both absorption and scattering result in the attenuation of the incident beam (light) and a reduction of visibility. Particles and gases absorb and scatter visible radiation at specific wavelengths.

The extinction of a beam of parallel monochromatic radiation (I_o) through a homogenous medium can be evaluated by the Beer-Lambert law, which states that the attenuation of light through a medium is proportional to the distance traversed in the medium and to the optical characteristics of that medium [69]:

$$\frac{dI}{dx} = b_{ext} I \tag{3.11}$$

Rearranging and integrating equation above (eqn 3.11):

$$\int_{I_o}^{I} \frac{dI}{I} = \int_{o}^{x} b_{ext} dx \tag{3.12}$$

Simplifying the integral:

$$I = I_o \exp(-b_{ext} x) \tag{3.13}$$

In equations 3.11, 3.12 and 3.13,

- I is the flux emerging from the medium after traversing distance x
- b_{ext} is the total extinction coefficient
- x is the optical path length (also called the relative optical air mass)

The Beer-Lambert law accurately represents the process of scattering by gases, and scattering and absorption by aerosols; however, absorption by gases is highly complex and is not adequately represented by the law. In the portion of the solar spectrum this work is focused on the visible spectrum (wavelength 380–700 nm), light absorption by gases is primarily attributed to Nitrogen dioxide (NO_2) and Ozone (O_3).

Light scattering by gases (also called Rayleigh scattering) is well understood and can be easily accounted for in radiative transfer calculations. Light absorption by fine particles is predominately due to Elemental Carbon (EC), along with minor contributions by mineral dust, and normally accounts for 5 % - 10 % of total light extinction in rural areas [14]. Several studies have shown that light scattering by fine particles usually dominates light extinction in most settings (e.g. [63] [70] [64]).

3.2.2 Light Attenuation and Visibility Measurement

Several terms describe visibility. The meteorological range is the distance from an ideal dark object at which the object has a 0.02 liminal contrast ratio against a white background. The liminal or threshold contrast ratio is the lowest visual perceptible brightness contrast a person can see. It varies from individual to individual. Although Koschmeider selected a value of 0.02, Middleton in 1952 tested 1000 people and found a threshold- contrast range of between 0.01 and 0.20 with the mode of the sample between 0.02 and 0.03[2]. Nevertheless, 0.02 has become an accepted liminal contrast value for meteorological-range measurements. Another measure of visibility, visual range, is the actual distance at which a person can discern an ideal dark object against the horizon sky rather than a white background.

The meteorological range is typically used for visibility calculations. It is related to the light attenuation by aerosols and gases through the total light extinction coefficient, and is derived in the following manner. Suppose a perfectly absorbing dark object lies against a white background at a point x_o. Since the object is perfectly absorbing, it reflects and emits no visible radiation; thus, its visible radiation at x_o is zero ($I_o = 0$). As the viewer moves away from the object, background white light scatters into the field of view, increasing the background that the viewer sees. Some of this light is scattered out of the field of view or is absorbed along the field of view by gases and particles. At some distance away from the object, so much background light has entered the field of view such that the viewer can barely differentiate the object against the background light. If I_B is the background intensity of light, the change in background intensity with distance is

$$\frac{dI}{dx} = b_b I_B - b_{ext} I \tag{3.14}$$

where I, is the incident radiation and b_{ext} is the extinction coefficient (along a field of view) due to absorption and scattering of incident radiation I by gases and particles. The product $b_{ext}I$ is the total attenuation of radiation along the field of view due to these absorption and scattering processes.

The change in background intensity I_B is given by

$$\frac{dI}{dx} = b_b I_B - b_{ext} I_B = 0 \tag{3.15}$$

If the background intensity is assumed to be constant with respect to x; $b_b = b_{ext}$.

Substituting $b_b = b_{ext}$ into equation (3.15) and rearranging gives:

$$\frac{dI}{I_B - I} = b_{ext} dx \tag{3.16}$$

Integrating (3.16) from I_0 (x = 0) to I (x = x) yields the contrast ratio

$$\int_0^I \frac{dI}{I_B - I} = \int_{x_0=0}^{x=x} b_{ext} dx \tag{3.17}$$

$$C_{ratio} = \frac{I_B - I}{I_B} = e^{-b_{ext} x} \tag{3.18}$$

C_{ratio} is the ratio of light intensity between an object and a background.

Therefore the distance x, the visual range can be easily computed by manipulating equation 3.18 and we have:

$$x = \frac{\ln(C_{ratio})}{- b_{ext}} \tag{3.19}$$

where $\ln(C_{ratio})$ is the natural log of C_{ratio}

When the conventionally accepted contrast ratio of 2% is used, the visual range is given by the Koschmeider equation below:

$$Vr = \frac{3.912}{b_{ext}} \tag{3.20}$$

3.3 Use of Digital Image Processing for Visibility Measurement

Monitoring of visibility is conducted on two complementary fronts - optical monitoring of visibility and monitoring the concentration and composition of the aerosols and gases in affected areas. For optical monitoring, two measurements are generally used, extinction (b_{ext}) measured by transmissometers, an instrument that directly measures light attenuation between a transmitter and receiver along a path length of 500 m to 1500 m or even greater distance; visual range may also be measured by use of human beings to observe the furthest distance they can see a dark object against a white background. The first method is precise and accurate. However the instrument used is expensive, and the measurement is confined to a fixed light path, and may not be sufficiently representative of visibility throughout the area of interest, nor does it account for sun angle. On the other hand, the use of human observers is inexpensive but the trade-off is that it is imprecise as different observers can provide significant varying results; this method (observation) cannot yield a continuous scale of visibility. Some approaches to measuring visibility have applied photograph processing methods to calculate or improve various model parameters related to atmospheric visibility ([71], [72], [73] and [74]). Such efforts have also tried to discern the influence of numerous important factors affecting visibility: size distribution and scattering properties of suspended aerosols; weather interference; chemical composition of pollutants, etc. However, the complicated procedures are not adequate for describing the real-time atmospheric visibility.

Therefore attempts have been made to look for alternative optical monitoring methods that are relatively inexpensive as well as providing precise and accurate results. In this thesis, Digital Image Processing (DIP) is proposed as a suitable

relatively precise and accurate technique for monitoring the optical properties of the atmosphere.

3.3.1 Background Theory on Digital Image Processing

The term "image" refers to a two dimensional light-intensity function, denoted by $f(x; y)$, where the value or amplitude of f at spatial coordinates (x; y) gives the intensity (brightness) of the image at that point. Since light is a form of energy, $f(x; y)$ must be non-zero and finite, that is

$$0 < f(x; y) < \square \tag{3.21}$$

Perceived digital images by the human eye consist of light reflected and or emitted from objects. The basic nature of $f(x; y)$ is characterised by two components. One component is the amount of light incident on the scene being viewed, while the other is the amount of light reflected by the objects in the scene. These components are appropriately called illumination and reflectance components, and are denoted by $i(x; y)$ and $r(x; y)$, respectively. The functions $i(x; y)$ and $r(x; y)$ combine as a product to form $f(x; y)$, that is:

$$f(x; y) = i(x; y)\, r(x; y) \tag{3.22}$$

where: $$0 < i(x; y) < \square \tag{3.23}$$

and: $$0 < r(x; y) < 1 \tag{3.24}$$

Equations 3.23 and 3.24 indicates the fact that reflectance is bounded by 0 (total absorption) and 1 (total reflection). The nature of $i(x; y)$ is determined by the light source, while $r(x; y)$ is determined by the characteristics of the object in a scene (the ratio of r(x, y) to i(x; y) is called reflectivity or albedo). Therefore, the values in equation (3.23) and (3.24) are theoretical bounds. The following average numerical figures illustrate some typical ranges of $i(x; y)$. On a clear day, the sun may produce in excess of 96875 lumen/m^2 of illumination on the surface of the earth [75]. This figure decreases to less than 10764 lumen/m^2 on a cloudy day. On a clear evening, a full moon yields about 0.11 lumen/m^2 of illumination. The typical illumination level in a commercial office is about 1076 lumen/m^2 [73]. Similarly, the following are some typical values of $r(x; y)$: 0.01 for black velvet, 0.65 for stainless steel, 0.80 for flat-white wall paint, 0.90 for silver-plated metal, and 0.93 for snow.

The intensity of a monochrome image *f* at coordinates (x; y) is mostly referred to as a gray level (□) or brightness of the image at that point. From equations (3.22) to equation (3.24) it is evident that (□) lies in the range:

$$L_{min} \square \square \square Lm_{ax} \tag{3.25}$$

In theory, the only requirement on L_{min} is that it is positive, and on L_{max} that it be finite. In practice, $L_{min} = i_{min}r_{min}$ and $L_{max} = i_{max}r_{max}$. Using the above values of illumination as a guideline, one may expect the values $L_{min} \sim 0.005$ and $L_{max} \sim 100$ for indoor image applications. The interval $[L_{min}, L_{max}]$ is called the gray scale. It is common practice to shift this interval numerically to the interval [0, L], where □ =0 is considered black and □ =L is considered white in the scale. All intermediate values are shades of gray varying continuously from black to white.

A gray level image can be presented by one component, brightness, while a colour image requires three components (red, green, and blue). Brightness difference in environmental images is an important factor in measuring visibility. Visual recognition by human perception requires signal change emitted from a target. This signal is primarily the target's brightness or gray level. A digital image acquired in the field provides the data for space dimension and gray level (digital brightness). These data may be represented in a M X N matrix [76]:

$$f(x,y)=\begin{bmatrix} f(0,0) & .... & f(0,N-1) \\ : & & \\ f(M-1,0) & ... & f(m-1,N-1) \end{bmatrix} \tag{3.26}$$

Each value in the matrix function represents the gray level at location *(x, y)*. Each element in the matrix is a pixel (or image element). A *k*-bit image gray level digital image has 2^k levels. All images for urban atmospheric visibility measurements in this study are 8-bit; their gray level values thus range from 0 to 255. The gray level value of 0 is set as perfect black. Brightness increases as the gray level value increases.

Since a colour image is produced in three standard components (red, □ = 700 nm; green, □ = 546 nm; and blue, □ = 436 nm), any pixel in the colour image consists of

brightness values for three colours: L_R (red), L_G (green) and L_B (blue). The wavelength of a component is represented by □. A colour image is converted into a gray level image (brightness L) with:

$$L = \frac{L_R + L_G + L_B}{3} \tag{3.27}$$

3.3.2 Direct Measurement of Light Attenuation from Inherent and Apparent Contrast measurements

Cleary, in his study on the influence of smoke on visibility, showed that pixel image intensities (gray levels) could be used to compute Weber's contrast ratio (C_w) using video detection and monitoring of smoke conditions[77]. The Weber's contrast ratio (C_w) is given by the expression below:

$$C_W = {}^{L_o}\!/_{L_b} - 1 \tag{3.28}$$

where L_o and L_b are the object and background brightness respectively.

Light extinction coefficient may therefore be estimated using equation 4.2 by computing, on clear and hazy days, the inherent and apparent contrast ratios, using pixel image intensities. Inherent contrast is calculated from a clear image where there is no influence of anthropogenic air pollution.

Over the years, numerous studies have been carried out to investigate the suitability of using still camera images to judge visibility. These images have been analysed using a technique known as photographic densitometric measurement, where the contrast between target and sky are measured quantitatively using a microdensitometer. This was found to be an effective and economical method for measuring visibility. The physical record makes it possible to go back to the images and investigate the effects of clouds or lighting, which would not be readily, identified using other measurement techniques.

Studies that have used Digital Image Processing for Visibility measurement

To date, two studies have made advancements in the use of digital image processing for visibility measurement. The paragraphs below discuss these studies in detail and summarize the methods used as well as their shortcomings.

Recently, Luo, Liu and Yuan (2003) used a digital image processing technique aimed at computing visual range from translated digital image data [73]. They used a 'nearly perfect target', an urban skyscraper, to obtain values of specific brightness (the brightness difference between the skyscraper and its background). Digital images were analyzed according to brightness. High frequency components of the image were extracted to calculate the index values by employing the Sobel operator. An explanation of how the Sobel operator works is given in the explanation below:

Consider a 3X3 mask (a mathematic matrix) illustrated below:

$$\begin{bmatrix} w_1 & w_2 & w_3 \\ w_4 & w_5 & w_6 \\ w_7 & w_8 & w_9 \end{bmatrix} \tag{3.29}$$

Response (R) of every pixel on the digital image is processed by the following equation:

$$R = w_1 z_1 + w_2 z_2 + \ldots + w_9 z_9 = \sum_{i=1}^{9} w_i z_i \tag{3.30}$$

where w_i's are the weighting coefficients in the 3 x 3 mask and z_i's are the gray level values (digital brightness) of corresponding points in the image. Sobel masks are shown as

$$\begin{bmatrix} -1 & -2 & -1 \\ 0 & 0 & 0 \\ 1 & 2 & 1 \end{bmatrix} \text{ or } \begin{bmatrix} -1 & 0 & 1 \\ -2 & 0 & 2 \\ -1 & 0 & 1 \end{bmatrix} \tag{3.31}$$

G_x G_y

i.e.,

$$Gx = (z_7 + 2z_8 + z_9) - (z_1 + 2z_2 + z_3) \tag{3.32}$$

$$Gy = (z_3 + 2z_6 + z_9) - (z_1 + 2z_4 + z7) \tag{3.33}$$

The G value of the pixel located by the center point of the mask can be computed by

$$G = \nabla f = |Gx| + |Gy| \tag{3.34}$$

The computations in Eqs. (3.32)–(3.34) are repeated pixel by pixel around the whole image. Finally, an index value for the Sobel operation is expressed by the average of G values for all points in an image. Because brightness noises improve the occurrence of high-frequency components, the Sobel operator can identify the discrepancy and gradient between any two points in the image in the spatial domain).

Finally, the correlation between the sobel index and the visual range estimated by trained investigators were evaluated. The two extraction processes were tested with a synthetic image shown in Fig. 3.5(a). In the spatial domain, the Sobel mask screens high-frequency components of the artificial image, and then the gradient mapping shown in Fig. 3.5(b) were utilized. Next, FFT transfers the same image into the frequency domain. The low frequency components in the frequency spectrum are cut off with a defined radius (CR =30 pixels). Fig. 3.5(c) presents the remaining map which is finally transferred to high-frequency pass information of, Fig. 3.5(d), in the spatial domain.

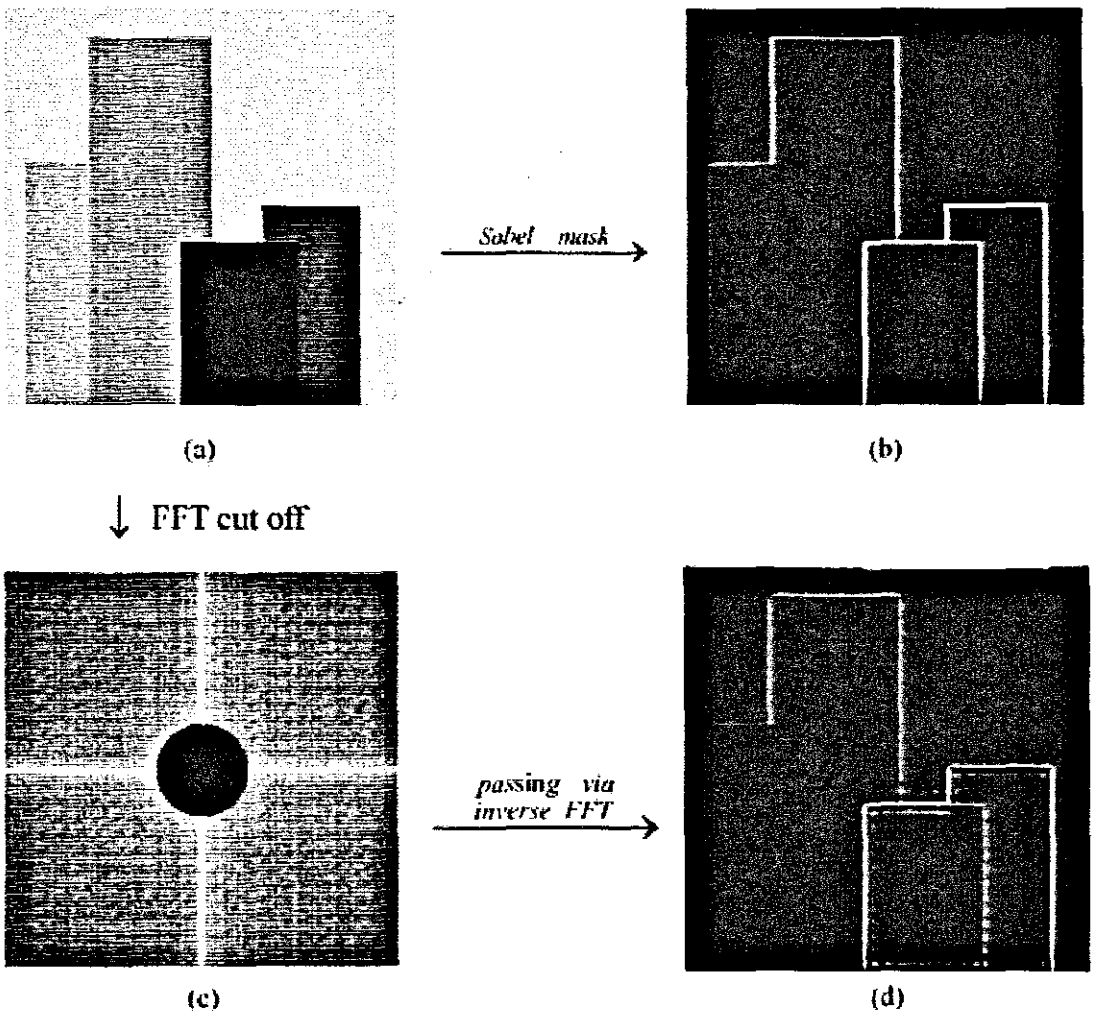

Figure 3.5: The two extraction processes: Sobel mask and FFT. (a) a synthetic image; (b) the result of spatial filtering by Sobel mask; (c) the result of low-frequency cut-off (radius = 30 pixels, solid black core) artificially operated after FFT; and (d) high-frequency information pass via inverse FFT. Figure adapted from Luo et al [73]

A good linear correlation between specific brightness and visual measurements obtained by trained investigators was established for a visual range of 5–10 km. A major advancement in the work of Luo, Liu and Yuan was to provide real-time measurement of visibility and characteristic images in particular areas. However the selection and appearance of an ostensibly perfect target is still a difficult problem in this approach as well as the fact that some outliers were observed compared with human observer's results.

Budgett and Mason (1998) [78] developed a software for visibility monitoring by digital camera. This software applied two methods to quantified visibility. A global approach quantified the sharp edges in the whole image using Fourier analysis. The ratio of the high to low frequencies was computed. Variable parameters are the radii

of both the high and low frequency zones. The second method manually divided the image into multiple (e.g. 10) regions. The distance to objects within each region was specified a-priori. If the variance of the pixel intensities within a region exceeded a threshold value, that region was deemed to be resolved. The visibility was taken to be the distance to the most distant region resolved. Results from a small database of images analyzed with the software suggested that both methods were capable of producing visibility predictions that varied considerably from human observation of visibility. Both methods were also limited in the sense that only visibility up to 10 km was measured owing to large uncertainties associated with human observation with improving visibility. As a result the mean absolute error between individual and average readings was 4.33 km, and the root mean squared (RMS) error was 6.63 km.

Chapter 4: Materials and Methods

4.1 Location of Study Site

Cape Town is an ideal location for this study. The impact of air pollution on visibility is well established [6], and it has a well established air pollution and meteorology monitoring network. It is an urban city with reasonable tall and big objects that can be used as targets (e.g. mountains). These mountains when observed are relatively dark of which they contrast significantly with the background sky. This is another important feature which facilitates this study.

The cameras used to monitor visibility for this investigation are located at the top of the Electrical Engineering Building at the Cape Peninsula University of Technology (Bellville campus). The altitude of this site is 15 metres (calculated using a global positioning system device, GPS) above ground level. This building, because of its height and perfect position relative to the chosen distant landmarks (objects), makes it an ideal location for our camera network. Three distant landmarks (target objects), Table Mountain (West), the Tygerberg Hills (North) and the 'Hottentots Holland' Mountains (East) were orientated with GPS (global positioning system). The distances between the target objects and the camera network building are 25, 27 and 9 km for west, east and north respectively. The distance of each pre-identified object relative to the camera station is calculated from coordinates generated from MAPSA (map based program). To ascertain that the distances obtained where accurate, global positioning system (GPS) coordinates data was used to compare the distance from the observation site to each object with an error less than 50m. These objects were also selected on the basis of their size as well as their position relative to the air pollution monitoring station in all three directions. For each camera-object path, an air pollution and meteorology monitoring station was identified. The Khayelitsha, Goodwood and City Centre monitoring stations were chosen for the East, North and west camera-target path respectively. The monitoring stations in all three directions were either along the camera-object path or slightly away from the path. It was assumed that air pollution levels and meteorology observed at the monitoring stations were a reflection of air pollution and meteorology across the whole camera-object

path. The location of the objects as well air pollution and meteorology monitoring stations enabled the simultaneous real time image, air pollution and meteorology sampling. The location of the study building, the monitoring stations and the chosen landmarks is illustrated by Figure 4.1 given below.

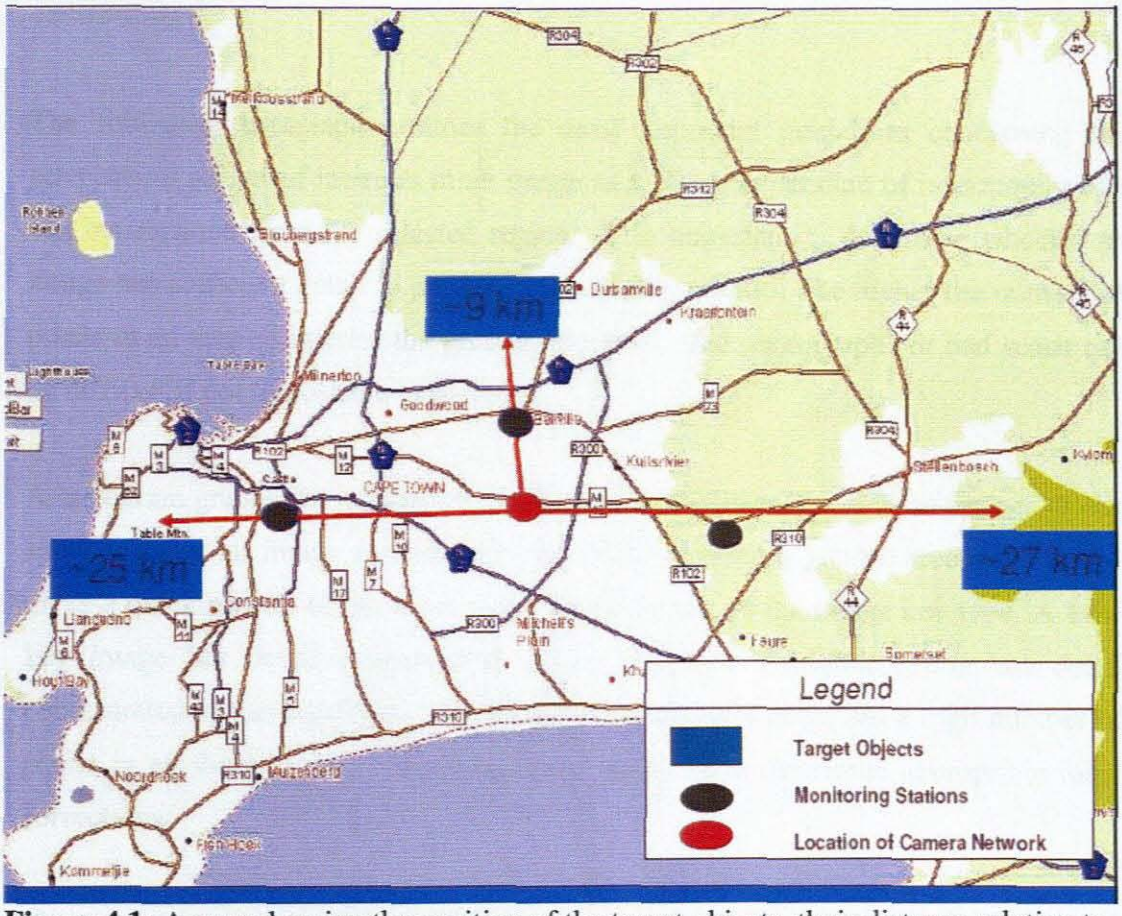

Figure 4.1: A map showing the position of the target objects, their distance relative to the camera network building as well as the black dots which represent the positions of the air pollution and meteorology monitoring stations. The map was generated from MAPSA (local map program).

4.2 Digital Image Processing

4.2.1 Image Capturing

The visual range is measured by taking snapshots (image sampling/capturing), every hour. These time- stamped images are archived for subsequent digital image processing. A digital image consists of pixels of varying levels of brightness over a range spanning 0 to 255 (8 bit). Brightness is a relative measure proportional to the luminance or intensity of the visible radiant energy from the sun. For the purpose

here, pixel brightness is considered to be a measure of normalized (non-dimensional) luminance. Thus, contrast measurements may be computed from the pixel brightness values. Therefore, average image intensities of selected areas (region of interest) of each image are computed from the histogram function results generated by digital image processing software (Photoshop™ 7.0), to obtain the inherent and apparent contrast ratios

The following paragraph outlines the most important guidelines concerning the selection of region of interests in an image as well as the amount of information that can be obtained from the selected region. It is important to determine whether an image has sufficient detail to produce high-quality output. The higher the number of pixels in an area of interest the greater the detail. Bad photographs or bad scans can be difficult if not impossible to correct.

A histogram graphs the number of pixels at each brightness level in an image. It can show whether an image contains enough detail to make a good correction. It also gives a quick picture of the tonal range of the image, or the image key type. A low-key image has detail concentrated in the shadows, a high-key one has detail concentrated in the highlights. An image with full tonal range has a high number of pixels in all these areas. Identifying tonal range helps determine appropriate tonal corrections.

If part of the image is selected, the histogram represents only the selected pixels. In addition, the histogram for an adjustment layer depends on the visibility of the layers beneath it.

The numerical values at the lower left of the Histogram dialog box in figure 4.2 display the following statistical information about the colour values of the pixels:

- Mean is the average brightness value.
- Standard deviation (STD) represents how widely the values vary.
- Median shows the middle value in the range of colour values.
- Pixels represent the total number of pixels used to calculate the histogram.
- Cache Level shows the setting for the image cache. If the Use Cache for Histograms option is selected in the Memory & Image Cache Preferences dialog

box, the histogram is based on a representative sampling of pixels in the image (based on the magnification), rather than on all of the pixels.

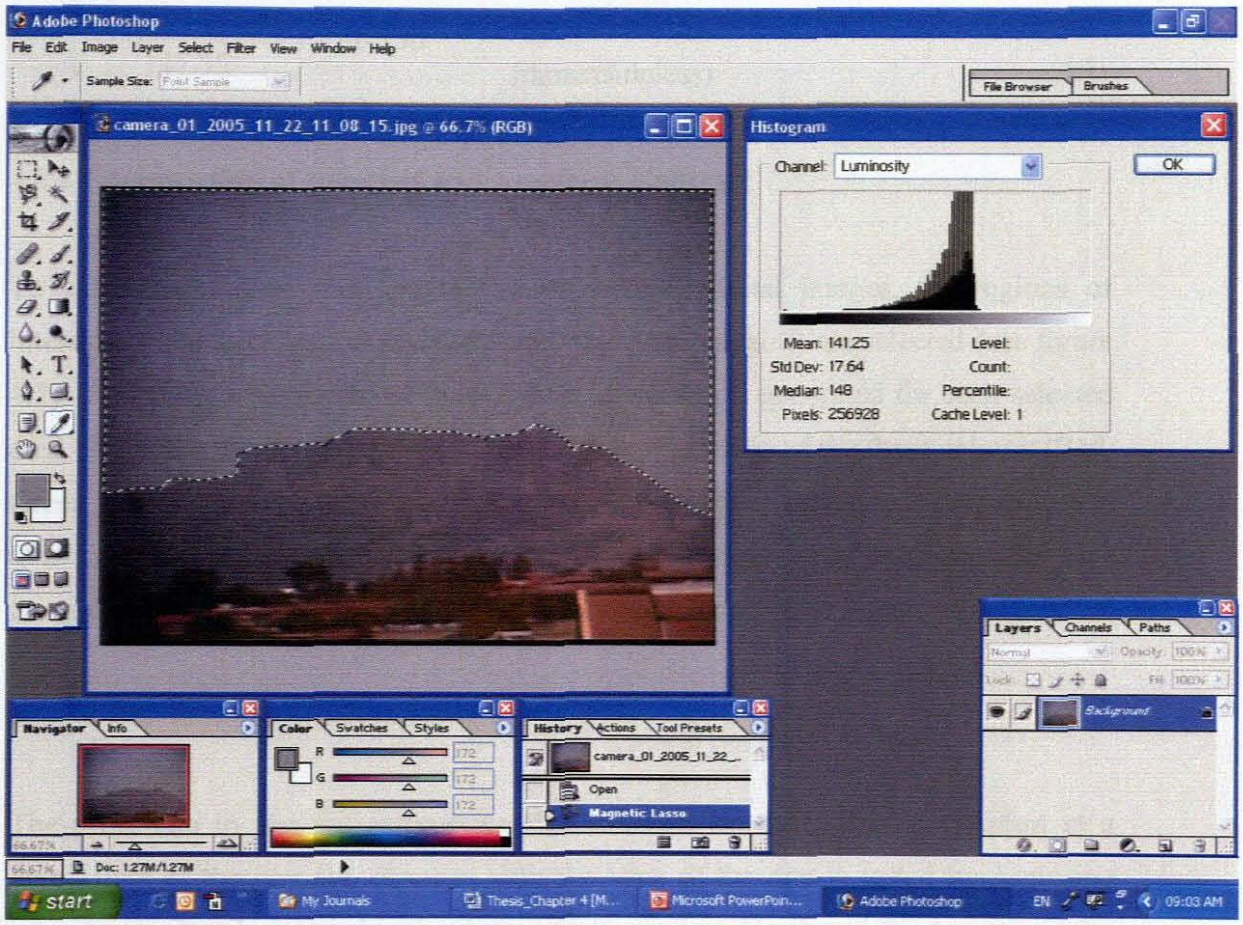

Figure 4.2: A screen printout of the digital image processing software (Photoshop^{TM}). Inside the dotted line is the selected region of interest (in this case, the background sky). On the right hand side of the image is the histogram dialog box.

The x-axis of the histogram represents the colour values from darkest (0) at the far left to brightest (255) at the far right; the y axis represents the total number of pixels with a given value. From the Histogram dialog box, it is possible to plot either the colour values in the individual channels or the luminance of the composite channel (with the Luminosity option). The values at the lower right of the dialog box change to display the gray level (Level) of the point (from 0 to 255), the total number of pixels at that level (Count), and the percentage of pixels at or below that level (Percentile).

Consider two regions of interest from an image, one is the sky background and another is the target object (mountain). I_{sky} (147.55) represents brightness level of the background sky and I_{object} (124.57) represents the brightness level of the

mountain. Contrast (C) is calculated from Io and I using the Weber's contrast ratio (equation 3.28) as follows:

$$C = \left(\frac{124.57 - 147.55}{147.55} \right) = -0.156 \quad \text{(dimensionless)} \tag{4.1}$$

4.2.2 Computation of Inherent and Apparent Contrast

To calculate inherent and apparent contrast from digital images, the regions of interest (i.e. the background sky and target object (mountain)) are selected (see figure 4.2). Secondly, a histogram of Pixel Image Intensities is generated for each selected area. From the histogram, the mean pixel image intensities of the three colours (Red, Green and Blue) are captured. A mean gray level is then calculated using equation (3.27). Selections of regions of interests as well as generation of histogram are done using digital image processing software called Photoshop™ 7.0.

4.2.3 Calibration of Inherent Contrast

The procedure to test the assumption that inherent contrast remains constant at a given time of the day and changes with the time of the day is tested by capturing images at an hourly interval in the three directions, East, North and West respectively. At a given hour, 5 images are sampled at varying distances in succession for each direction. In order to calculate inherent contrast, one needs to have a pristine environment. Therefore, Inherent contrast measurements are done in a remote area which is 10km South of Touwsriver, Western Cape. A Canon Camera (5 mega-pixels and 12x optical zoom Camera) was used to sample the images. The distance between the landmarks and the point of image capture were measured using co-ordinates generated by a GPS (Global Positioning System). Measured distances are 9 km's, 11 km's and 14 km's for west, north and east respectively. This calibration is done to take into account the effects of sun angle on visibility. To simulate the same time period used in apparent contrast measurements, the image sampling period was also between 08:00 and 18:00.

4.2.4 Computation of b_{ext} from Inherent and Apparent Contrast

In order to estimate light attenuation from digital images, equation 4.2 is used to estimate the light extinction coefficient (b_{ext}). Mean pixel intensities obtained from image analysis of sampled digital images are used to compute Inherent (C_o) and apparent (C_r) contrast values. These contrast values are then used as inputs to equation 4.2. The theoretical derivation of equation 4.2 is available under appendix A.

$$b_{ext} = \frac{1}{r}\ln\left(\frac{R_n C_o}{C_r}\right) \tag{4.2}$$

Sample calculation of b_{ext}

Consider an image of the Table Mountain (west direction) sampled at 10H 00 with an inherent contrast (C_o) of -0.4803 when pollutant-free, and an apparent contrast (C_r) of -0.00456 at that time. The distance (r) between target (Table Mountain) and the subject (camera station) is 25 km. R_n can be assumed to be 1 (see section 4.2.5) for rationale). Calculating the light extinction coefficient from this data we get:

$$b_{ext} = \left(\frac{1}{25}\right) \times \ln\left(\frac{1 \times -0.4803}{-0.00456}\right) = 0.186\ \text{km}^{-1} \tag{4.3}$$

4.2.5 Calculating the Uncertainty in b_{ext} associated with Digital Image Processing

In order to calculate the uncertainties associated with the estimation of light extinction coefficient from digital image processing, it is observed that the relative precision (uncertainty U_x) of the mean ($\bar{x}$) of a set of measurements of some variable is defined as

$$U_x = \frac{SD_x}{\bar{X}} \tag{4.4}$$

Where: SD_x is the standard deviation and $\bar{x}$ is the mean of a measurement

Applying standard procedures to equation 4.4, the propagation of uncertainty through it can be expressed as [79].

$$U_{bext} = \left[\frac{\left(U_{R_N}^2 + U_{C_o}^2 + U_{C_r}^2\right)^{0.5}}{\ln\left(\frac{R_N C_o}{C_r}\right)} \right] \quad (4.5)$$

Equation 4.5 also shows that the actual values and uncertainties in R_n, C_o, and C_r are all equally important and cannot be ignored when estimating the uncertainty in calculated b_{ext}.

Relative Uncertainty in Sky Radiance Ratio (R_n) estimates

Typically, when calculating b_{ext} from target/sky contrast measurements, the sky radiance ratio is not measured but is assumed to be equal to 1.0 [80]. Lack of R_n measurement has been due to unavailability of a method to measure b_{ext}. With digital image processing, the calculation of R_n has been made possible through the use of mean pixel intensities. Previous empirical studies on visibility have found the relative uncertainty in estimated R_n to be about 30 %. This was observed from field measurements using instruments such as the Tele-radiometer as well as modelling efforts. Therefore the relative uncertainty in R_n can be reasonable assumed to be about 30 % [78]:

$$U_{R_N} = 0.3 \quad (4.6)$$

Relative Uncertainty in Inherent Contrast (C_o) Estimates

In estimating b_{ext} from target/sky contrast measurements, the inherent contrast is not measured but is estimated from historical analyses of the cleanest days at a monitoring site. C_o is a function of the illumination of the target, solar/observer geometry, and the background extinction. Thus, C_o varies with time of the day, time of the year, cloud cover, target surface reflectance, and ambient extinction. Inherent contrast can vary from -0.2 for a granite cliff in direct solar illumination with a backscattering solar geometry to -1.0 for a dark coniferous forests shaded by clouds with a bright forward scattering background sky. In practice, a standard C_o is estimated for a target at a particular time of the day from the cleanest day available. This C_o is then used in all subsequent b_{ext} calculations. Analyses of historic tele-radiometer and slide contrast data have indicated that the uncertainty in the C_o

estimates for reasonable dark targets (tree covered ridges) is typically 10%, 20% for grass covered targets, and 40% for bare rock [81] and [71]

U_{Co} = 0.1 for tree covered targets

U_{Co} = 0.2 for grass covered targets

U_{Co} = 0.4 for bare rocks

Relative Uncertainty in Apparent Contrast (C_r) Measurements

The apparent target contrast is calculated from the density measurements made on 35mm colour slides or analysis of calibrated digital images. For colour slides this requires a transformation of measured slide densities to the exposures on the slide which are directly related to the onsite radiances by employing published film response curves. The uncertainty of Cr from 35 mm slides has been examined by comparing measured slide Cr from slide densitometry versus simultaneous onsite radiometric measurements of Cr [82] and [83]. The analysis indicates that the uncertainty is about +/- 0.04 in contrast. This means that the relative uncertainty varies from over 100 % for targets just barely visible to about 10 % on very clean days.

$$U_{C_r} = \frac{0.04}{C_r} \tag{4.7}$$

4.2.6 Camera Network Set-up

Instruments used include: three video cameras (Eagle Technology, E-6311xP-H cameras equipped with E-50500D 20 to 100mm Variable-focal Auto Iris Lenses). These cameras secured in weather protection housings are mounted on top of the Electrical Engineering building of the CPUT Bellville campus (latitude: 18°38'34": longitude: - 33°55'56") 15 meters above ground level (measured using GPS). The front of the housing is cleaned occasionally to avoid dust and debris from hindering the sight of view for the cameras. All the cameras are connected to a personal computer. This was achieved by connecting the camera data cables to a four channel video card (PICOLO Pro 2™).

The PICOLO Pro 2™ board support the acquisition of full resolution images (640 x 480 or 768 x 576). It allows for full-image real-time sampling from 1 to 4 cameras.

Individual images as well as video sequences are captured directly to the PC memory. Any image format is supported, thanks to a high-quality hardware scaler. The board generates image formats in all popular colour formats such as RGB, planar or packed.

The PICOLO Pro 2™ card is operated with FRAMEGRABBER software for image sampling. FRAMEGRABBER is supported by Multicam driver which enables consistent control of PICOLO Pro 2™ board and allows for defining channels linking cameras to buffers in the PC memory. FRAMEGRABBER software is written specifically to automatically sample images at selected time intervals for a four channel (four camera connection) card. The user can specify the time-interval at which the cameras can sample images. Since the air pollution and meteorology stations sample on an hourly basis, an hourly time interval is selected for image sampling. Image sampling was performed hourly between 08:00 and 18:00 daily, from 1 October to 30 November 2005. The images with a resolution of 768 x 576 were archived as JPEGs. In this study three cameras are connected to the PICOLO Pro 2™ card. Figure 4.3 below summarizers the camera set-up used for image sampling in this study. To simulate the photopic perception of far-gazing human eyes, camera focus is set to infinity (□), and the camera's flash is not applied.

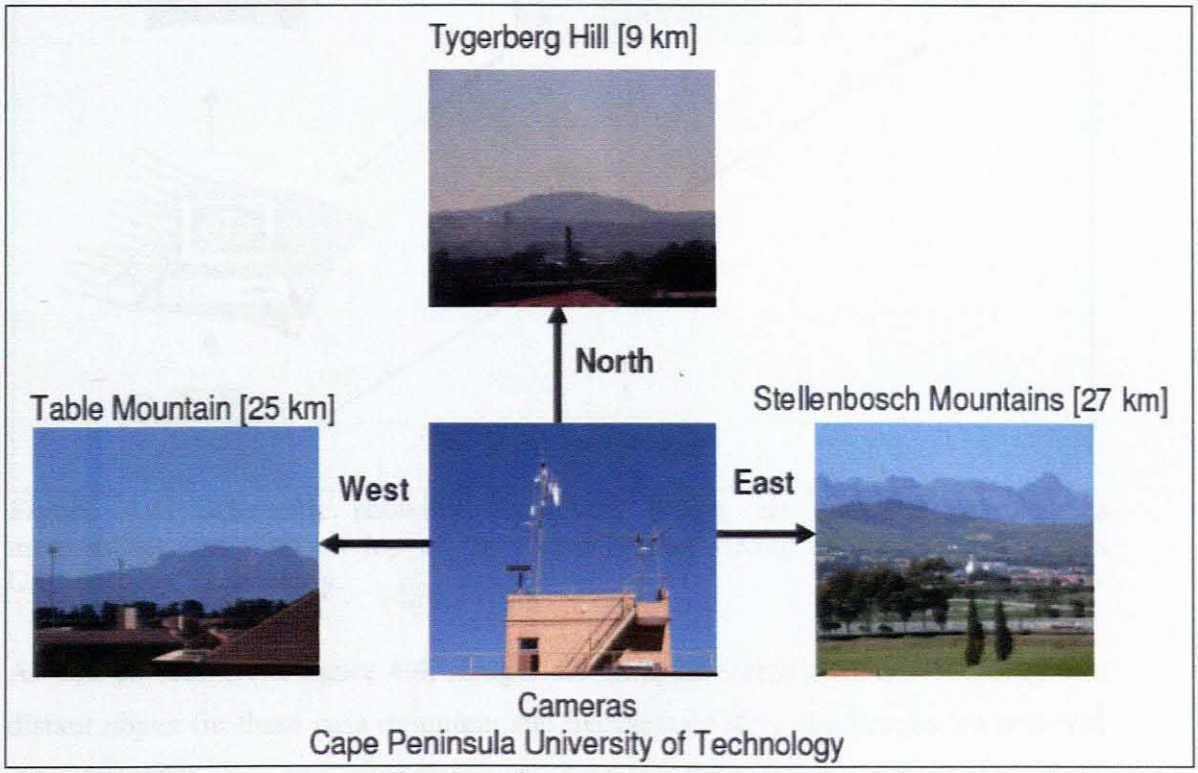

Figure 4.3: Camera set-up showing the camera station positioned on top of the electrical engineering building (CPUT) as well as the three target objects in the east, north and west direction.

4.3 Visibility Model Development

4.3.1 Air Pollution and Meteorology Sampling

After the visual range estimates have undergone the uncertainty tests using the method outlined in section 4.2.5, they are used as in the development of a real-time visibility models. The total extinction coefficient (b_{ext}) in the Koschmeider equation is computed from modelled air pollutant concentrations derived from air pollution monitoring station data as well as the Brown Haze I species data [84]. Also, the $PM_{2.5}$ mass fraction is computed from the $PM_{2.5}/PM_{10}$ ratio average for individual air pollution monitoring station.

Capturing and transmission of images and visual observation results is processed at the same time, and schematically shown in figure 4.4. as well as a computer with software for image capturing as well as software for digital image processing.

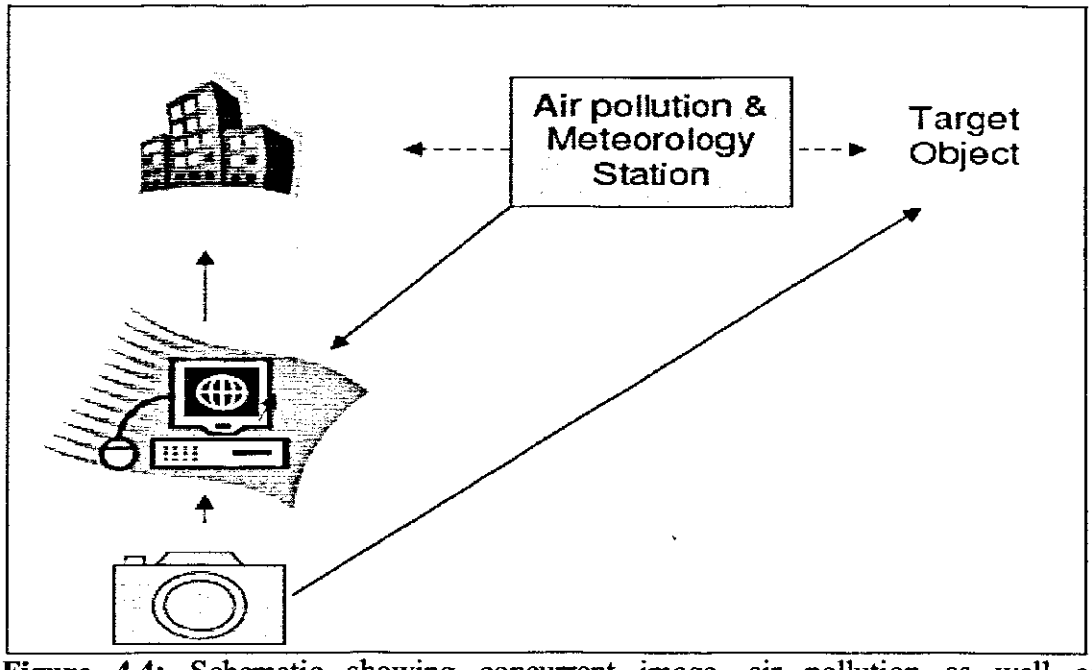

Figure 4.4: Schematic showing concurrent image, air pollution as well as meteorology sampling on top of the electrical engineering at the Cape Peninsula University of Technology.

As can be seen from figure 4.4, images are sampled using a camera focusing at a distant object (in these case mountain and background sky), the images are archived in a processing computer, simultaneously the air pollution and meteorology stations samples air pollutants, wind speed as well as relative humidity. The camera and the

processing computer are positioned on the same building. The air pollution and meteorology station is positioned between the building and the target object path.

This study is based on both regular and intensive observations of atmospheric visibility in Cape Town. Regular observation is conducted to elucidate the temporal and spatial variation of atmospheric visibility, while intensive observation is conducted to elucidate the diurnal variation of daytime atmospheric visibility. During regular observation of atmospheric visibility, images were sampled each day at 08:00 and 18:00 from March 2005 to August 2005. A total of 1300 images were sampled during this period. Furthermore, intensive observation of atmospheric visibility is conducted during September-November 2005; during which images are sampled each hour from 08:00 to 18:00. During this intensive observation period, a total of 3670 images were sampled. In addition, atmospheric aerosols and gases are sampled in situ and meteorological data is obtained from the three air pollution monitoring stations for further statistical analyses. In this way six data points are collected based on the direction [East, North and West] of the target object as well as the season [winter or summer]. Visual range measurements using from digital image processing are compared against visual range estimated by using the light extinction equation 4.9.

4.3.2 Sampling Equipment

Real- time air pollution data (SO_2, NO_2, O_3 and PM_{10}) all in μgm^{-3} is sampled using instruments belonging to the Scientific Services of Cape Town. These instruments are situated in the three monitoring stations described under the location section. Maintenance and calibration of all instruments is performed by the scientific services of Cape Town. Principles of operation of these equipments as well as calibration procedures are outlined in Appendix E.

4.3.3 Development of Real-Time Visibility Model

In this study, a multiple regression model is developed to correlate atmospheric visibility with air pollutants and meteorological factors. Among the air pollutant factors, NO_2 and SO_2 are the precursors of secondary nitrate and sulphate aerosols. Relative humidity represents the moisture content of aerosol particles. Although fine

particles (0.90 μm < dp <0.26 μm) were thought of as the most efficient aerosols to scatter visible light, PM_{10} is used as the input variable since it is routinely measured in situ. Initially, simple multiple linear regression is used to construct the model. Variable selection methods (stepwise regression) are used to further refine the model by eliminating significant variables. Furthermore, multiple regression diagnostics methods are employed to eliminate influential observations and outliers.

$$Log(Vr) = a_1 PM_{10} + a_2 NO_2 + a_3 SO_2 + a_4 O_3 + a_5 RH + a_6 Ws + a_7 \quad (4.8)$$

where Vr: atmospheric visibility (km); PM_{10}: particulate matter with dp □ 10 μm (μ gm^{-3}); NO_2, SO_2, O_3; concentration gaseous pollutants (μgm^{-3}); RH: relative humidity (%); Ws: wind speed (ms^{-1});

Equation (4.8) is then used to determine the atmospheric visibility with known input variables and can be further compared with atmospheric visibility from light extinction model (equation 4.9).

4.3.4 Software for Multiple Linear Regression Analysis

In order to construct a real-time visibility forecasting model using air pollution, visibility as well meteorological data, a statistical software program called Stata is used. Stata is a command based statistical program capable of performing both descriptive as well as inferential statistical tests. In this study, Stata is used for performing Multiple Linear Regression (MLR) analysis. Furthermore, Stata is used for variable selection procedures to remove significant variables as well MLR model diagnostics to eliminate outliers and influential observations. In this way a real-time visibility forecasting model is developed using air pollution, meteorology, and visibility data. The advantage of using this statistical software program is that it allows the user to perform the entire MLR analysis step by step by feeding it with commands. This means that at any given step of the analysis, the user is aware of what the program is performing as well as being able to interpret the results accordingly. A list of commands used for MLR analysis, Variable selection as well as MLR model diagnostics are provided under Appendix I.

4.3.5 Validating Visual Range estimates from Real-Time Measurements

Since it is the only means of measuring visibility, the following equation is central to this work since it is used for the purpose of validating the digital image processing visibility measurements from digital images as well as a standard from which real-time visibility estimates are compared against. This equation is an extension of equation (3.1) and is derived from a combination of theoretical as well as empirical reasoning [66].

$$b_{ext} = a_1\{f(RH)\}[SO_4^{-2}] + a_2\{f(RH)\}[NO_3^-] + a_3\{f(RH)\}[VO\ Cs] + a_4[soil] + a_5[coarse\ mass] + a_6[EC] + a_7[NO_2] + a_8[O_3] + bo_2 + bn_2 + b_{rg} \quad (4.9)$$

The quantities in brackets [] represent pollutant concentrations (mass/ volume: μgm^{-3}); the effect of humidity on hydroscopic particles is given by the relative humidity factors ($f_{i,(RH)}$) for sulphates, nitrates and organics; the coarse mass is the (PM_{10}-$PM_{2.5}$) concentration. The ($b_{i's}$) are the light scattering co-efficiencies for nitrogen, oxygen and the remainder of the gases (<1 %)) in the atmosphere and the constants ($a_{i's}$,) with units of m^2g^{-1} are dry mass absorption and scattering efficiencies.

The extinction efficiencies for soil and coarse mass are taken from a literature review by [85]. For soil, the dry extinction efficiency of 1 m^2g^{-1} is used, and for coarse mass, a value of 0.6 m^2g^{-1} is used. For both nitrate and sulphate, a dry extinction efficiency of 3 m^2g^{-1} is based on literature reviews by [86] and by [87]. Trijonis' best estimate for sulphates and nitrates is 2.5 m^2g^{-1} with an error factor of 2, while White's average low and high estimates for the rural West are 3.0 and 3.7 m^2g^{-1} respectively. For organic carbon mass, Trijonis estimates a dry extinction efficiency of 3.75 m^2g^{-1}, again with an error factor of 2, and White's low and high average estimates for the rural West are 1.8 and 4.1 m^2g^{-1} respectively. Based on these estimates, Chow et al (2002) [88] used a dry extinction efficiency of 4 m^2g^{-1} is used. Chow et al (1993) ([89] demonstrated that the assumption of the dry specific scattering values yielded good agreement between measured and calculated extinction across the entire IMPROVE monitoring network. Using Thermal Optical Reflectance (TOR), Chow et al [87] measured an extinction coefficient of 10 m^2g^{-1} for elemental carbon. Studies by Watson et al (1983) [77] and Richards et al (1989) [90] also estimated an

extinction efficiency of 0.17 m^2g^{-1} for nitrogen dioxide. Later on this extinction efficiency was used by Chan et al (1998) [1] in their source apportionment of visibility degradation study in Brisbane Australia.

The table below summarizes the theoretical mass extinction efficiencies that are obtained from the studies mentioned above and used by Malm in his study of visibility in both urban and remote areas in the IMPROVE network. These extinction efficiencies are wavelength dependent and for simplification purposes are derived at a wavelength of 550 nm. Extinction efficiency for ozone is calculated using theoretical data from Jacobson (1999) [2], since no study has calculated ozone mass extinction efficiency empirically. Compared to human subjects on validation of visibility measurements, this model performs extremely well [see results section]. It is for this reason that this equation has been used for DIP measurement output validation

Table 4.1: Extinction efficiencies developed by theoretical as well as empirical methods. The extinction efficiencies are wavelength dependent and therefore those presented in this table are for visible light at 550 nm.

Pollutant	Extinction efficiency constant	Extinction efficiency value (m^2g^{-1})
SO_4^{2-}	a_1	3
NO_3^-	a_2	3
VOCs	a_3	4
Soil	a_4	0.6
Coarse mass [PM_{10}-$PM_{2.5}$]	a_5	1
Elemental Carbon [EC]	a_6	10
NO_2	a_7	0.17
O_3	a_8	0.21

4.4 Converting Light Extinction Coefficient into Visual Range

When the conventionally accepted value of $C_{ratio} = 0.02$ at λ (radiation wavelength = 0.55μm) is used in equation 3.09, the resulting distance is the visual range (Vr) given by the Koschmeider equation [2]. The Koschmeider relationship (equation 3.20) gives a valid approximation of visual range only under a limited set of conditions. Important assumptions and limits are listed below [10] [64]:

1. Sky brightness at the observer is similar to the sky brightness at object observed;
2. Homogeneous distribution of pollutants;
3. Radiation wavelength of 550 nm
4. Horizontal viewing distance;
5. Earth curvature can be ignored;
6. Large black objects; and
7. Threshold contrast of 0.02.

Appendix B discusses these assumptions in detail.

4.5 Setting up a Haze Index

The proposed haze index proposed in this study differs significantly from haze index scales that currently exists (i.e. deciview index). The approach used to develop the haze index in this study recognises the non-linear nature by which visibility conditions change with light extinction by basing visibility in the form of an exponential function given below:

$$V_r = b^{V_i} \tag{4.10}$$

Where b is the visual range in km

b is the base (constant) visual range equivalent to 1.53 km

V_i is the exponent by which the base visual range is raised to obtain the corresponding value of V_i, the Visibility Index.

V_r is the visual range in km

Based on fundamentals of visibility laws (Koschmeider equation) as well as established practices of visibility monitoring, atmospheric visibility has been divided into four visibility levels. Each level is provided with a visibility descriptor to communicate the extent of visibility or conversely, visibility degradation.

The visibility levels and descriptors are derived from the following arguments.

- 70 km has historically been taken as representing almost perfect visibility. The ultimate visibility in the atmosphere is determined by fundamental Rayleigh

scattering of the natural gaseous constituents of the air, and is around 290 km. However, few people would be able to distinguish between 290 km and 70 km [13].

- 20 km has been, and is, used by many countries as the defining line between "good" and "degraded" visibility. For instance, in Australia the 20 km distance has been used as a primary visibility indicator for attainment purposes.
- 11 km is regarded as the minimum acceptable ambient visual air quality and also based on the concept, arising from meteorology, of visibility sufficiently degraded to have an impact on some activities, such as viewing of scenic vistas
- 2 km is used consistently by the aviation industry as the minimum acceptable Runway Visual Range (RVR) as set by the International Civil Aviation Organization (ICAO) [91]

Furthermore, a visibility index (V_i) scale of 1 to 10 is assigned to an atmospheric visibility range of 0 to 70 km (based on arguments above). The haze index which describes the extent of visibility degradation in a scale of 10 to 1 is then derived from the visibility index. In order to convert from visibility index scale to haze index scale, it follows that:

$$H_i = 11 - V_i \tag{4.11}$$

Expressing equation 4.11 in terms of the visibility index we have:

$$V_i = 11 - H_i \tag{4.12}$$

Substituting equation 4.12 into equation 4.10 we observe:

$$V_r = b^{(11-H_i)} \tag{4.13}$$

Applying natural logarithm and rearranging equation 4.13 to solve for H_i we have:

$$H_i = 11 - \left[\ln V_r / \ln b \right] \tag{4.14}$$

where H_i is the haze index

Vr is the visual range in km in the following range [70 > Vr > 0 km]

b is the base visual range (b= 1.53 km)

Alternative equation 4.14 can be expressed in terms of the light extinction coefficient by substituting equation 3.20 (Koschmeider equation):

$$H_i = 11 - \left[\ln(3.912/b_{ext}) / \ln b \right] \quad (4.15)$$

Where b_{ext} is the light extinction coefficient in km^{-1}

Chapter 5: Results

5.1 The effect of Sun Angle on Inherent Contrast (C_o)

A series of field experiments were conducted to evaluate the effect of the sun angle on inherent contrast. This was achieved by sampling digital images hourly. This image sampling time interval also corresponded to air pollution, meteorology and visibility monitoring records. For each direction (East, North and West) and time (hour), five images were sampled at varying distances (from 0 m to 400 m). In a separate experiment, further data were collected to demonstrate that measured inherent contrast remains constant with distance over a range 0 to 2.8 km (see figure 5-2). These images were then analysed using the Digital Image Processing method described under section 4.4.2. In this way, sun angle corrected inherent contrast calibration curves were generated and were later used in the calculation of light extinction using equation 4.2 (DIP equation). The generated calibration curves are available under appendix F:

Figure 5-1 illustrates the effect of sun angle on measured inherent contrast by plotting the numerical value of inherent contrast with the time of the day in the east direction. Inherent contrast remains constant as the subject moves away from the object at a given hour. In the morning, inherent contrast decreases from 0.667 at 08:00 to 0.314 at 12:00 and increases to 0.441 at 18:00. In the morning when the sun is positioned in the east, inherent contrast is high and thus poor visibility conditions are observed. As the day progresses, the sun shifts to the west and consequently measured inherent contrast decreases and thus the visibility conditions improves. As the angle of the sun changes observing that the sun rises from the east and sets on the west, the illumination properties of the object are influenced and thus the inherent contrast is also influenced. It is also observed that inherent contrast remains constant as the subject moves from 0 m to 400 m. For example a mean inherent contrast of 0.667 with a standard deviation of 0.0099 at 08:00 is observed.

Figure 5-2 illustrates how inherent contrast remains constant as the subject further moves away from the target object. In this plot of change in inherent contrast with

the subject's distance away from the object, the subject moved a distance of almost 3 km (2804 m) away from the object. The furthest distance that the subject could observe was limited by the size of the target object. A mean inherent contrast value of 0.746 was observed with a standard deviation of 0.0001. This small standard deviation proves that in pristine environments, inherent contrast remains constant.

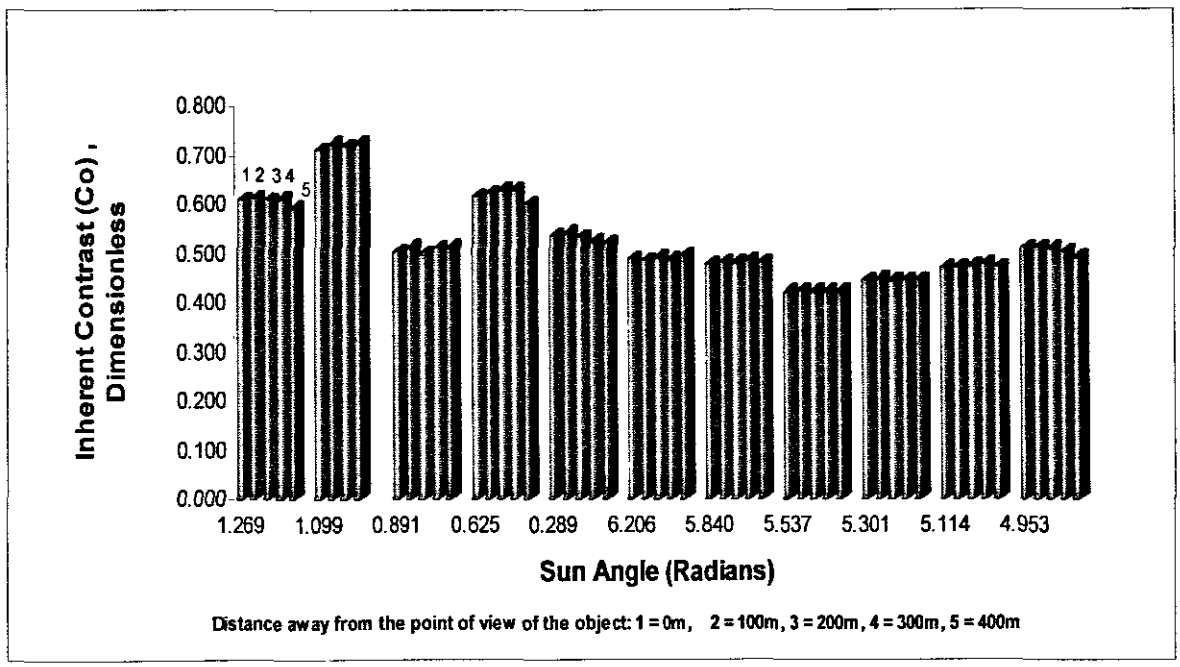

Figure 5-1: Inherent Contrast (C_o) calibration curve to correct for the influence of the sun angle on the illumination properties of the object as viewed by the subject.

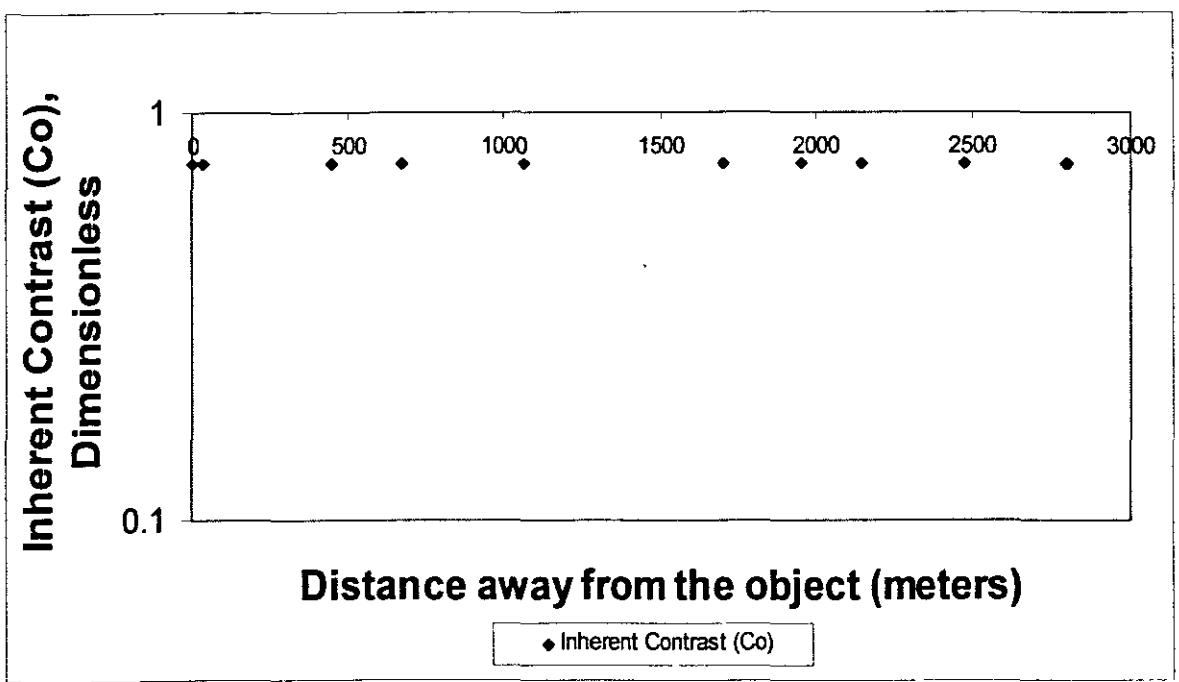

Figure 5-2: Change in measured Inherent contrast as the subject moves away from the target object [This set of data was collected at 14:00].

5.2 Computing Visual Range using Digital Image Processing

Figure 5-3 shows a comparison between visual range estimates using digital image processing and visual range measurements from the light extinction model. In the morning (10:00) and in the afternoon (14:00 -1600), there is disagreement between the two methods. This is a result of not accounting for the effect of the sun angle on the calculation of the visual range from digital image processing. In the mornings and afternoons the sun is lower and therefore sun rays have further distance to travel. However, during midday (10:00 to 14:00), there is a strong agreement between the two methods. During midday the sun rays have less distance to travel.

Figure 5-4 shows an improved comparison between the two methods after the visual range estimates from DIP were corrected for sun angle through the measurement of inherent contrast. In the mornings and afternoons there is a strong agreement in the visual range values whilst during midday results remains unaffected.

Table 5-1 summarizes the data used in the light extinction model. The regression efficiencies used in the light extinction model are for wavelength of light equivalent 550 nm are those used by Malm in his IMPROVE project [92].

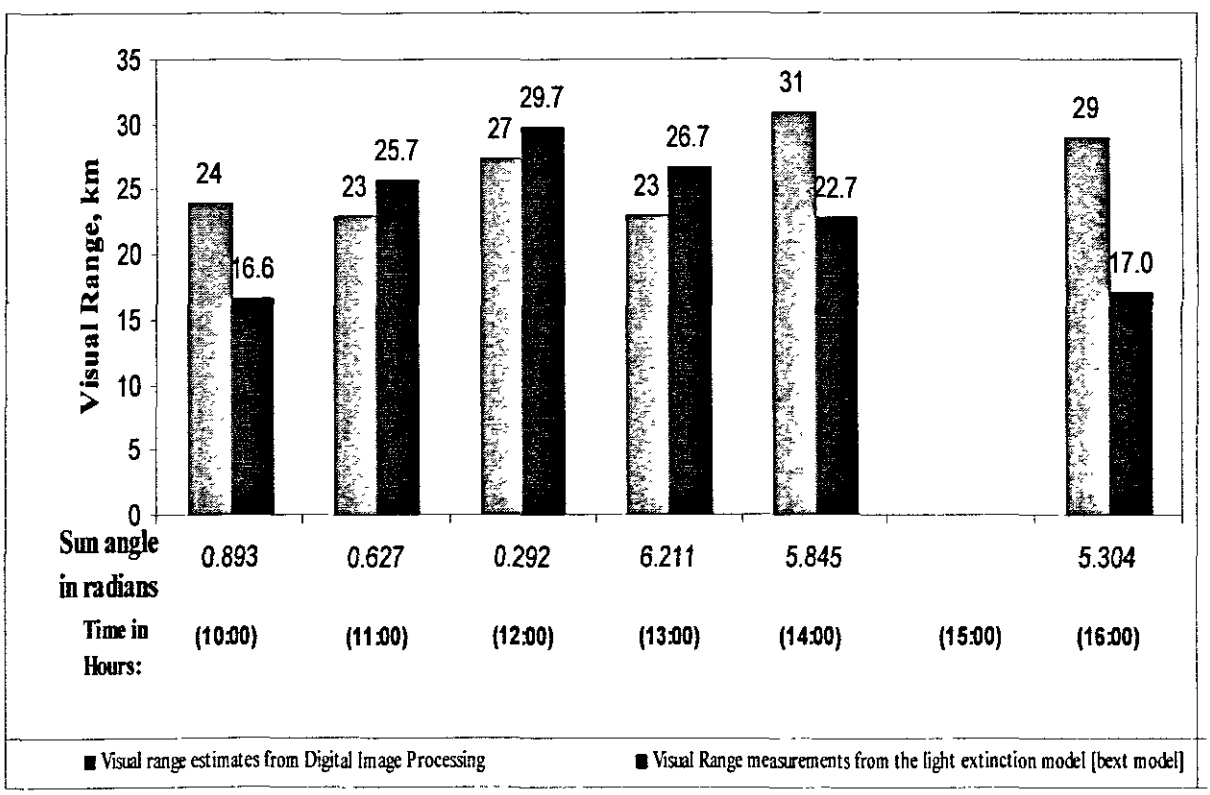

Figure 5-3: Results of Visual Range measurements using Digital Image Processing [DIP] compared to visual range estimates from light extinction model [equation 4.9].

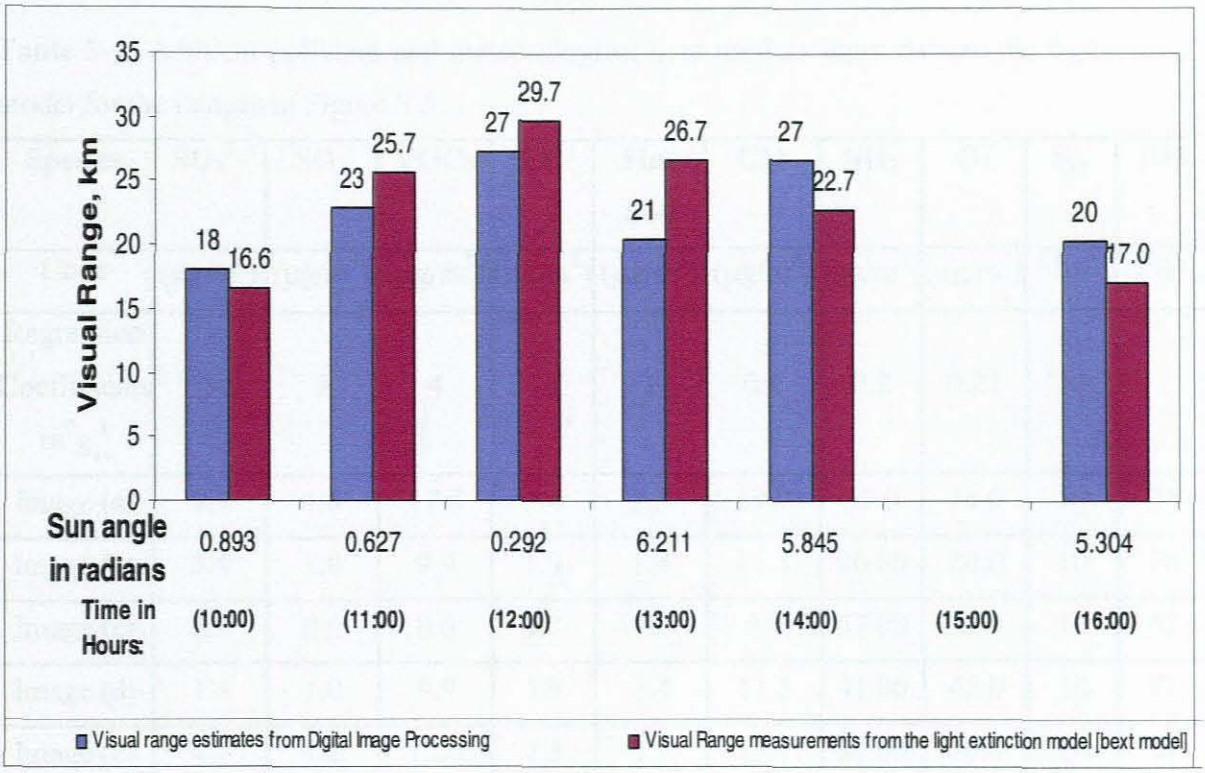

Figure 5-4: Results of Visual Range measurements using Digital Image Processing [DIP] compared to visual range estimates from light extinction model after correction for sun angle.

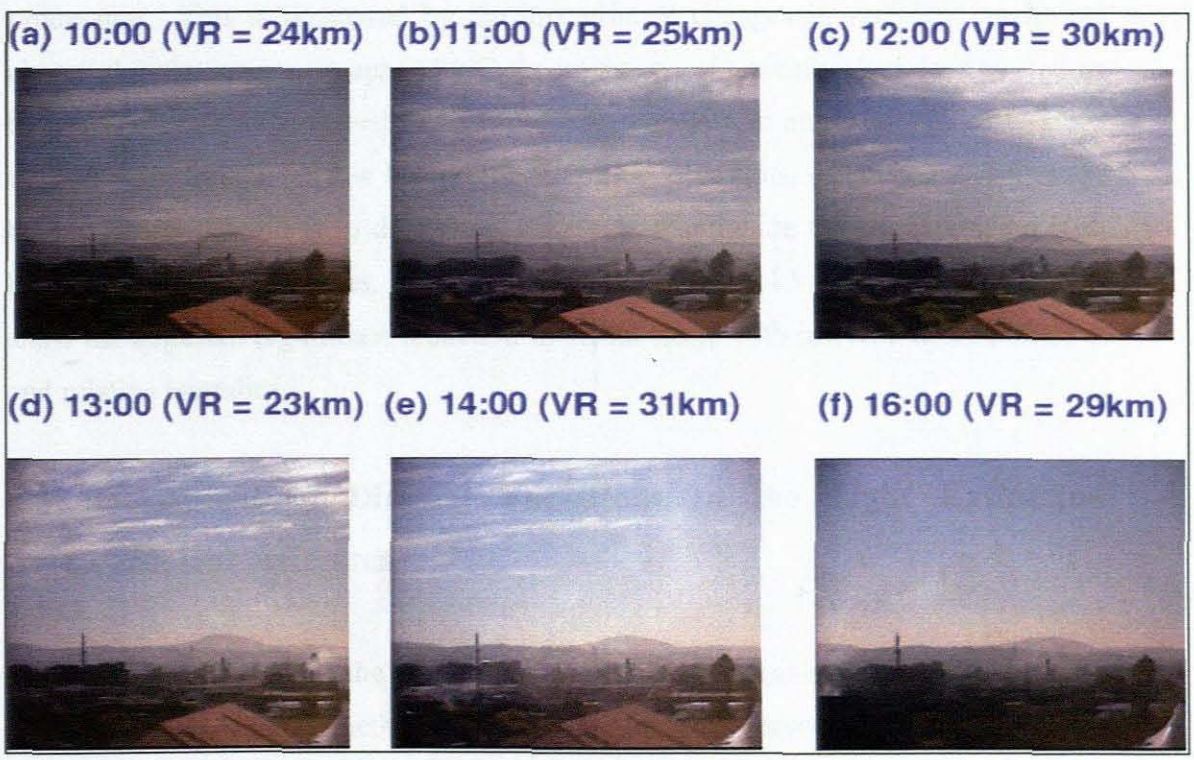

Figure 5-5: Images corresponding to the visual range measurements from Digital Image Processing

Table 5-1: Ambient pollutant and meteorological data used as input data in the b_{ext} model for the images in Figure 5-5.

Species	SO_4^{2-}	NO_3^-	VOCs	EC	Fine Soil	CM	NO_2	O_3	b_{rg}	RH
Units	($\mu g/m^3$)	($\mu g/m^3$)	($\mu g/m^3$)	($\mu g/m^3$)	($\mu g/m^3$)	($\mu g/m^3$)	($\mu g/m^3$)	($\mu g/m^3$)	Mm^{-1}	(%)
Regression Coefficients m^2g^{-1}	3	3	4	10	1	0.6	0.2	0.21	10	
Image (a)	5.9	1.8	17.5	3.4	2.5	19.9	59.0	14.0	10	75
Image (b)	3.4	1.0	9.9	1.9	1.4	11.3	90.00	20.0	10	76
Image (c)	2.9	0.9	8.6	1.7	1.2	9.8	57.00	32.0	10	62
Image (d)	3.4	1.0	9.9	1.9	1.4	11.3	41.00	42.0	10	75
Image (e)	4.1	1.2	12.0	2.3	1.7	13.7	37.00	50.0	10	64
Image (f)	5.7	1.7	16.8	3.3	2.4	19.1	55.00	31.0	10	82

Figure 5-5, shows precision in the estimation of visual range from digital image processing. This is illustrated by the insignificant changes in visibility conditions observed in the images. In appendix C, a comparison of typically clear days as well as hazy days in all three directions is provided. Panels a, c and e of Figure C-1 are typical video images on low haze (high visibility) occasions, calculated visual range 80 to 120 km, for the three directions. Panels, b, d and e are the corresponding high haze (low visibility) images, with calculated visual range 13 to 19 km. The results show the expected significant reduction in visual range with increase in air pollution and relative humidity.

5.3 Assessment of Diurnal Variations in the Light Extinction Coefficient estimates

Figures 5-6 and 5-7 show the variation in the light extinction coefficient estimates by digital image processing method for winter and summer seasons respectively. In the mornings (between 08:00 and 10:00), there b_{ext} values are observed to be relatively higher than the rest of the day. This is a result of the inversion layer that occurs

frequently in winter and thus impairs visibility. In this case the light extinction coefficient increases and consequently the visual range decreases (poor visibility conditions). In figure 5-6, in the north direction at 09:00, the light extinction coefficient is equally to 173 Mm^{-1} (Vr =19 Km) and thus poor visibility condition is observed. It is also observed that between 12:00 and 16:00, visibility conditions improves as the inversion layer disappears due to photochemical reactions in the atmosphere. However, between 16:00 and 18:00, visibility conditions began to deteriorate again due to vehicle emissions. About 72 % NOx, 88 % VOC's, and 54 % PM is contributed by motor vehicles in Cape Town [[93]. In the afternoon, a high b_{ext} value of 152 Mm^{-1} (21 km) is observed for the west direction in Figure 5-6. This is due to the effect of the sun setting in the west direction and thus degrading visibility conditions. In figure 5-7, a high morning b_{ext} value of 83 Mm^{-1}(39 km) is observed whilst in the afternoon a high value of b_{ext} of 89 Mm-1 (36 km) observed for the west direction.

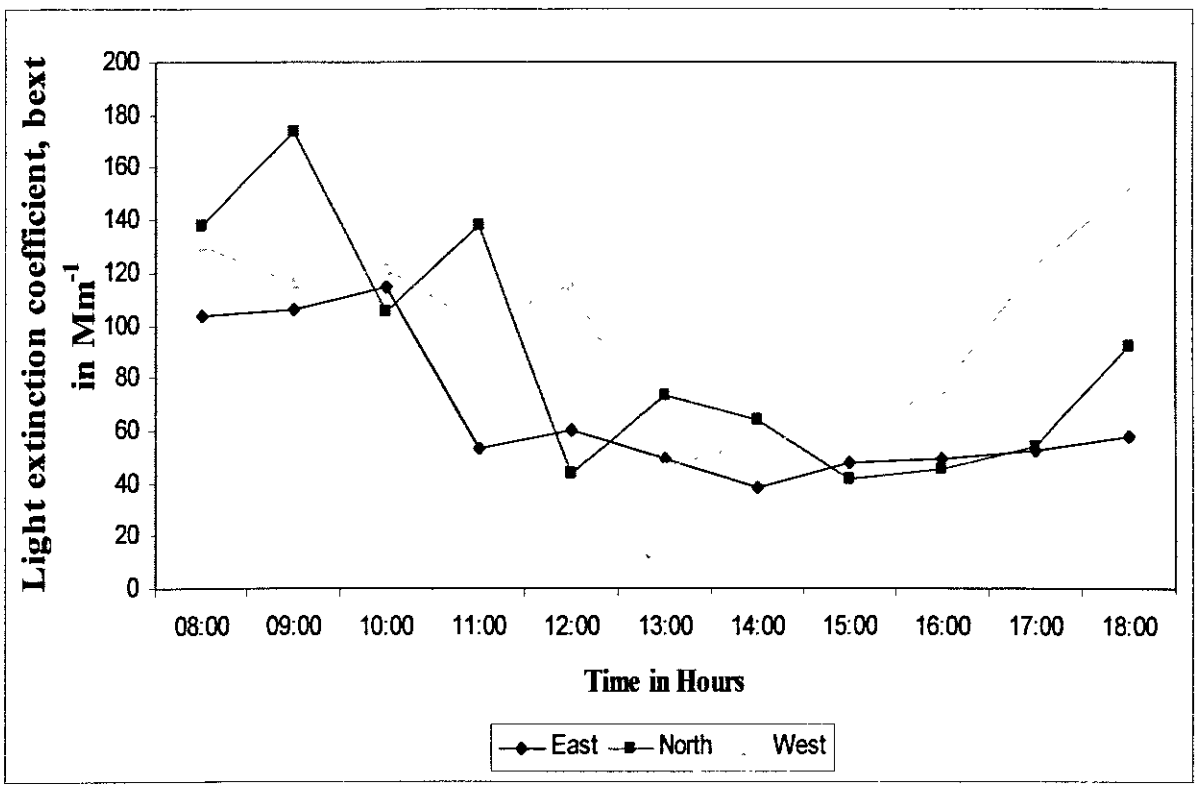

Figure 5-6: Diurnal variation in the light extinction coefficient, b_{ext} (Mm^{-1}) (29/07/2005) (winter).

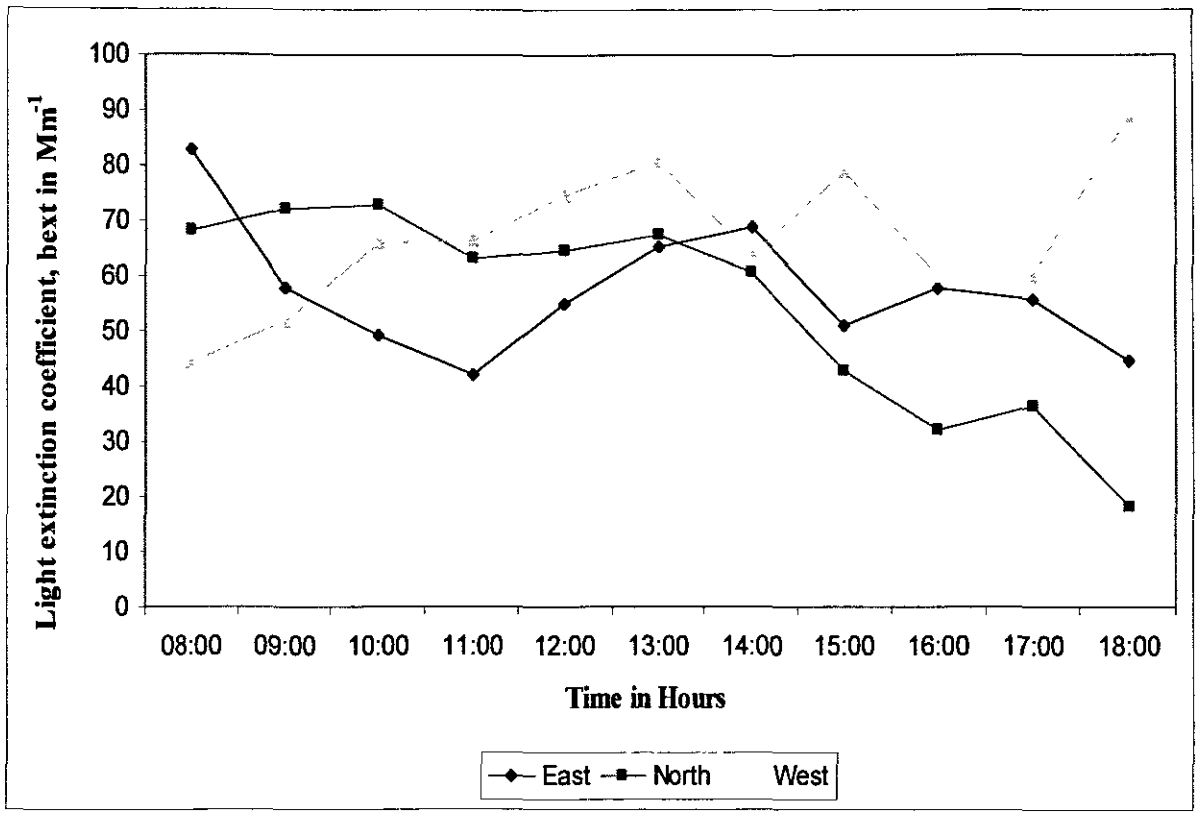

Figure 5-7: Diurnal variation in the light extinction coefficient, b_{ext} (Mm^{-1}) (05/10/2005) (summer).

5.4 Measuring Uncertainty in Contrast Measurements for Target/Sky Combination

Following the arguments assumptions described under section 4.2.5, it follows that equation 4.5 can be further simplified into the form given in equation 5.1:

$$U_{bext} = 100\left[\frac{\left(0{,}09 + U_{C_o}^2 + \frac{0{,}0016}{C_r^2}\right)^{0,5}}{\left(\ln\frac{C_o}{C_r}\right)}\right] \qquad (5.1)$$

Figure 5-8 plots the estimated uncertainty in calculated *bext* from digital image analysis as a function of true ambient extinction. In the b_{ext} range of 30 to 120 Mm^{-1} [110 to 27 km], which is typical of the three directions [East, North and West] in winter, the digital image analysis extinction uncertainty is in the range 2 to 12 %. In terms of visual range, this means that for a visual range of 27 km the uncertainty is in

the range of ± 3.1 km and for a visual range of 110 km, the uncertainty is in the range of ± 3.3 %. It is also evident from the plot that as the visibility conditions deteriorate (high b_{ext} values or low visual range values), the percentage uncertainty in the estimated b_{ext} also increases. However the percentage uncertainty range from digital image processing is considerable low when compared to uncertainties observed from other visibility measuring methods such as slide densitometry and Transmissometer. In Figure 5-9 which is a plot of uncertainties for summer time, the uncertainty range is observed to be significantly lower because of generally better visibility conditions in summer. The uncertainty range is between 1.5 to 8 percent. Table 5-2 compares the uncertainties obtained from digital image processing, slide densitometry and from a transmissometer. It is observed from the table that uncertainties associated with digital image processing are significantly lower when compared to other methods at the respective ambient light extinction values.

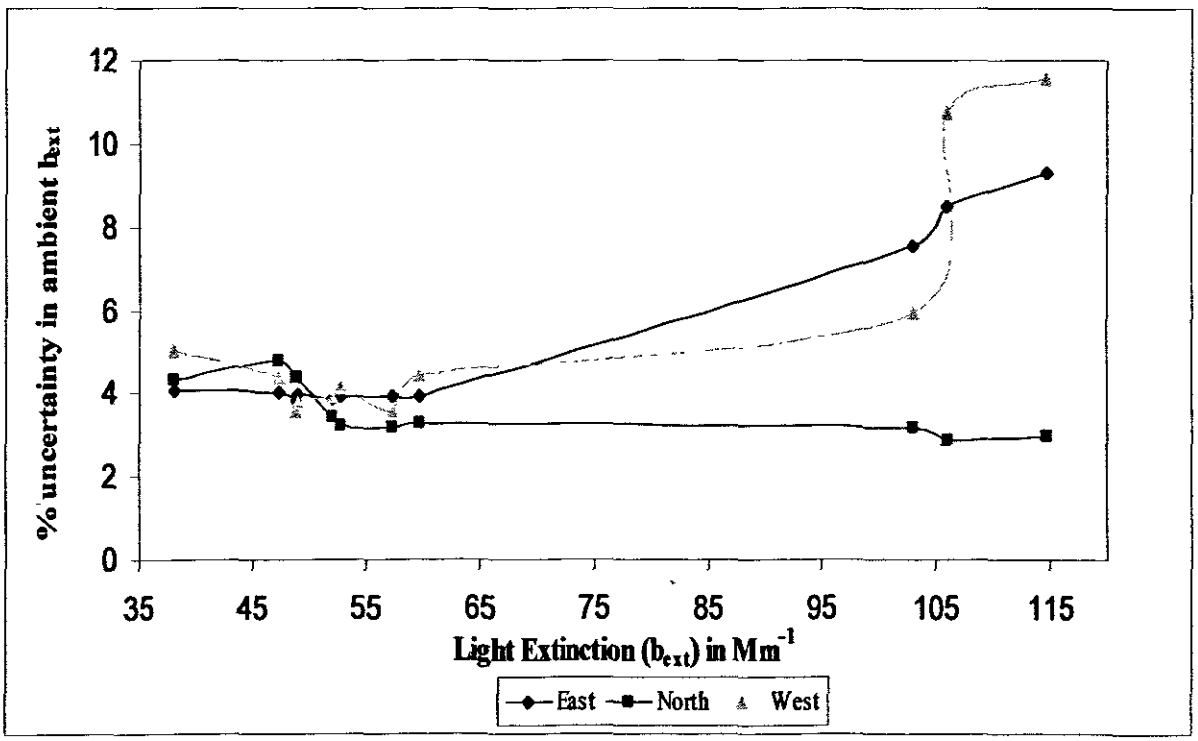

Figure 5-8: A plot of % uncertainty in the estimation of b_{ext} by digital image processing as function of ambient b_{ext} estimated from light extinction model. This plot is for the winter season.

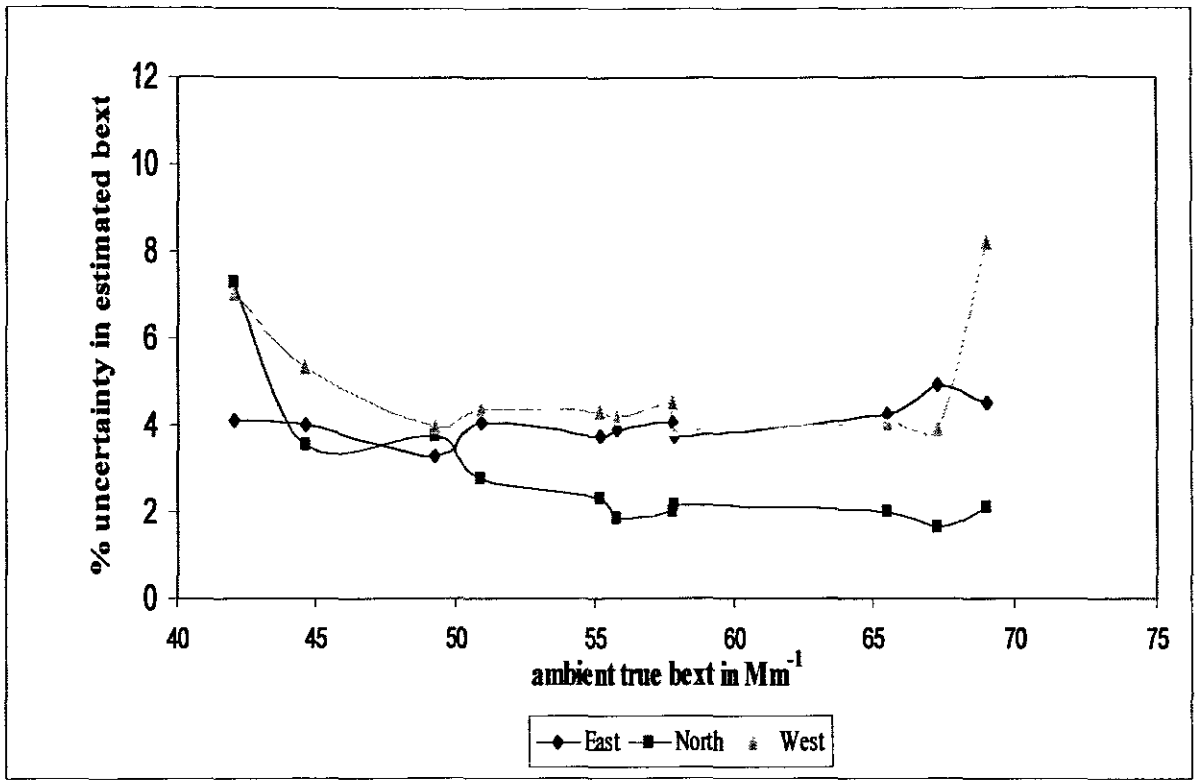

Figure 5-9: Plot of % uncertainty in the estimation of b_{ext} by digital image processing as function of ambient b_{ext} estimated from light extinction model. This plot is for the summer season.

Table 5-2: Comparing uncertainty associated with three different methods of calculating the light extinction coefficient (b_{ext}).

b_{ext} measurement method	**Slide Densitometry**	**Transmissometer**	**Digital Image Processing**
Ambient Extinction (b_{ext}) in Mm^{-1}	**(% Uncertainty)**		
40	30	15	4.3
50	26	11	4.1
60	22	10	3.6
70	23	8	3.4
80	26	8	3.4
90	28	5	3.2
100	30	4.3	2.5
110	43	4.1	2.6

5.5 Comparison of DIP Visual Range estimates with b_{ext} Model Results

In order to ascertain the strength of visual range estimates from digital image processing, visual range measurements from light extinction model were used for correlation plots. These plots were generated for each direction [East, North and West] and for each season [summer and winter]. These plots were later used to correct visual range estimates from digital image processing used in the development of the real-time visibility forecasting models.

Figure 5-10 and Table 5-3 illustrates the relationship between visual range estimates from digital image processing and visual range measurements using the light extinction model. In figure 5-10, the relationship is for a plot of summer data for the east direction. There is strong correlation between the two observations ($R^2 = 0.789$) depicting that there is a strong agreement between the two measurement methods. There results for other conditions are presented in table 5-3.

Figure 5-11 shows an improved relationship between the methods after the visual range estimates from DIP were corrected for sun angle. The correlation coefficient is observed to increase from 0.789 (Figure 5-10) to 0.825.

In all cases (the plots are available under appendix G) the correlation coefficient is observed to be significantly higher with the east winter plot showing the strongest correlation ($R^2 = 0.824$) and the summer west data showing the least correlation strength ($R^2 = 0.614$). Compared to other studies elsewhere, correlations between visual range estimates from traditional methods and visual range measurements obtained from target object observation by human subjects. Jackson for example reports a poor correlation coefficient of 0.161 for a plot of general visibility versus distance visible [94].

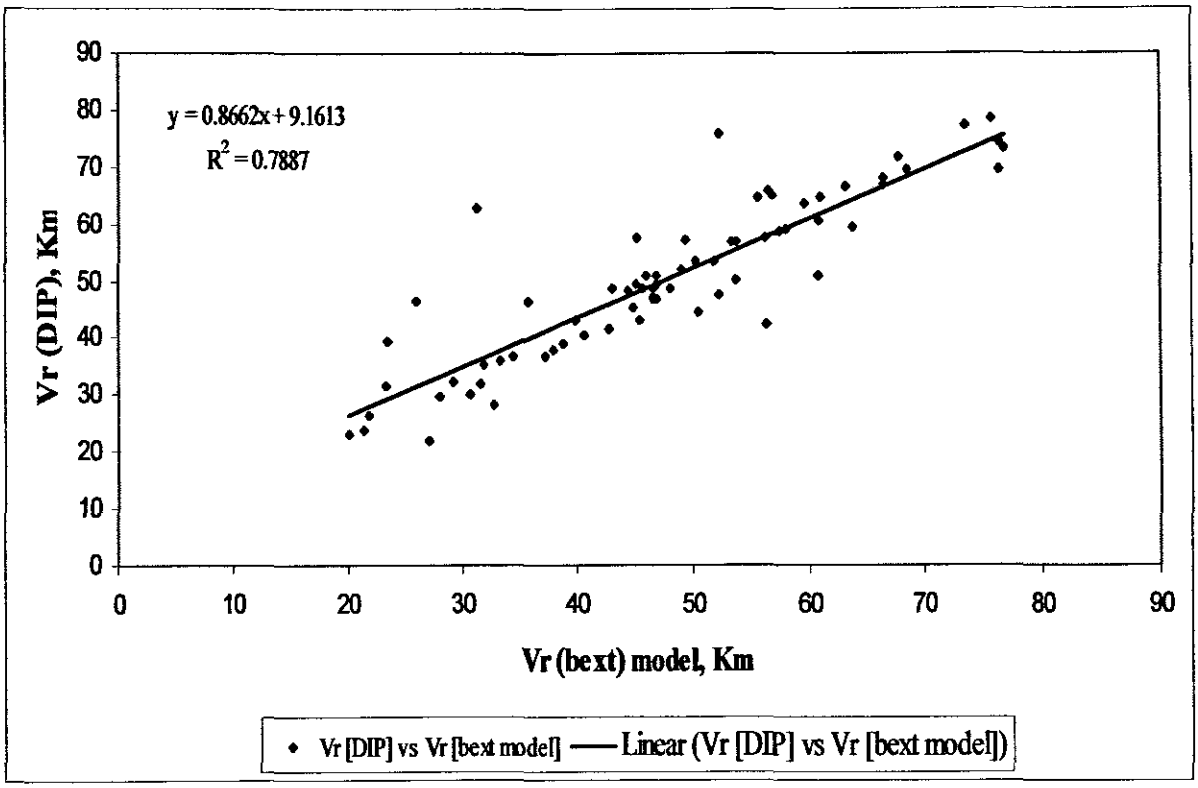

Figure 5-10: Correlation between digital image processing measurements and estimates from the light extinction model for east direction and summer season.

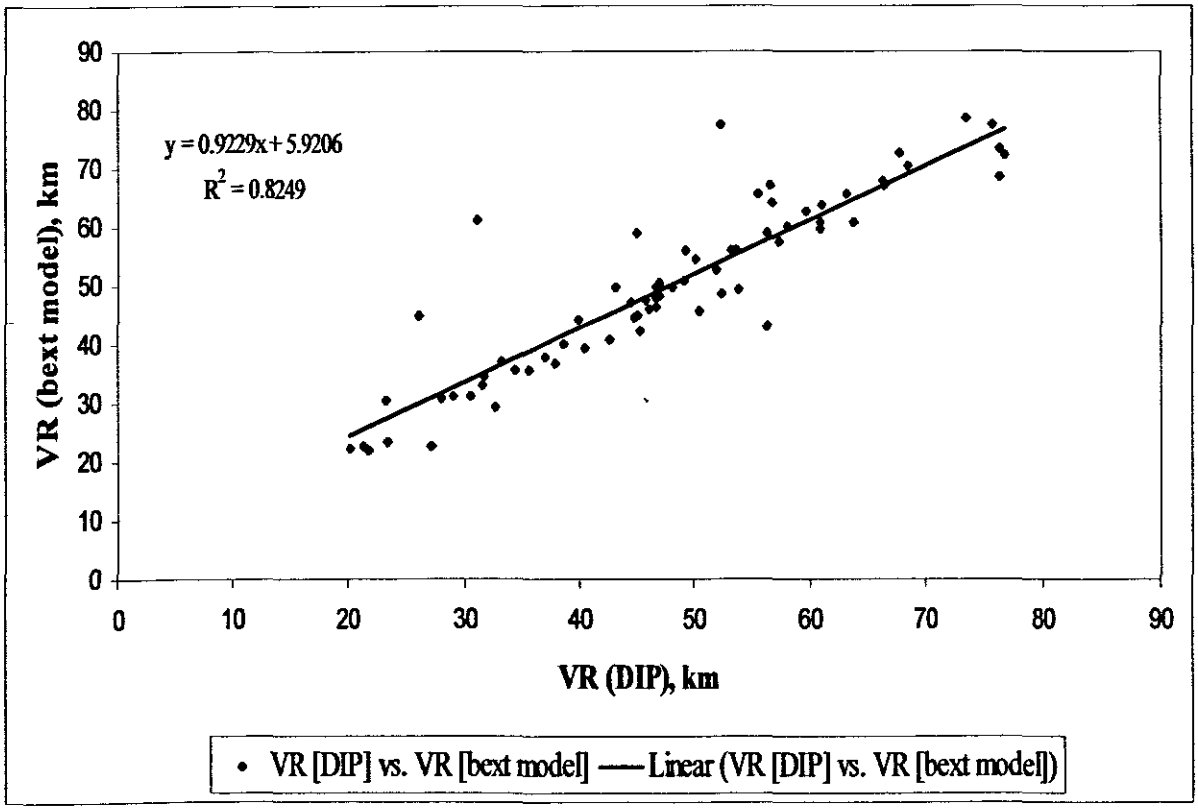

Figure 5-11: Sun Angle corrected calibration curve for east direction and summer season.

Table 5-3: Complete Results of correlation between visual range estimates from digital image processing and visual range measurements from the light extinction model.

Season	Direction	Constant (a)	Slope (b)	Correlation coefficient (before correction for sun angle)	Correlation coefficient (After correcting for sun angle)
Summer	East	9.16	0.87	0.789	0.825
	North	5.87	0.96	0.728	0.751
	West	7.98	0.93	0.614	0.675
Winter	East	1.09	1.02	0.824	0.857
	North	5.37	0.97	0.753	0.816
	West	2.81	1.06	0.793	0.864

5.6 Evaluation of Light Extinction Coefficient Components

In order to access and compare the various components contributing to the total light extinction coefficient, the four components of light attenuation were computed for the three directions [East, North and West] and two seasons (summer and winter). Extinction efficiencies used in the extinction coefficient model as well air pollution and meteorological data obtained from monitoring stations were used for this exercise. Air pollution data was further modelled using Brown Haze I speciation data to compute species concentrations of the pollutants contributing to light extinction.

Table 5-4 illustrates the percentage contribution of the four light extinction coefficients towards total light extinction for the six cases. In all six cases, light scattering by particles (b_{sp}) is observed to be the major contributor to light extinction with the east direction (in winter time), having the highest percentage of 93 % and the west direction (in summer time) having the least contribution of 70 %. This observation is also confirmed by all studies done elsewhere that light scattering by particles (b_{sp}) in the largest contributor to total light extinction (see table 5-5). It is also observed that absorption by gases is the second contributor. A contribution of 17 % is observed in the west direction (summer time).

Table 5-4: % Contribution of light extinction components towards total light extinction coefficient.

Season	Direction	Scattering gases, b_{sg} (%)	Scattering particles, b_{sp} (%)	Absorption particles, b_{ap} (%)	Absorption gases, b_{ag} (%)
Winter	East	2	93	3	2
	North	3	88	4	5
	West	5	82	4	9
Summer	East	5	81	6	8
	North	6	79	6	9
	West	8	70	5	17

Table 5-5 shows a comparison of the contribution of the four light extinction coefficient in Cape Town with those observed in studies conducted in other cities. Cape Town is observed to have the highest contribution of particle scattering with a contribution of 79 %, although some of this studies where done one or two decades ago. It is also observed that although light scattering by particles is the largest contributor, the percentage proportion of the four components varies substantially from one city to another city. It is however expected that scattering by particles in some cities would have been decreased because of intervention to reduce vehicle, biomass burning or industrial emissions. In Cape Town the situation is likely to escalate unless something is done to improve the transport system or to introduce environmental friendly energy sources for the poor communities.

Table 5-5: Comparison of percentage proportions of extinction coefficients from different studies [1].

Extinction coefficients	Brisbane 1993	Sydney 1978	Denver 1978	Los Angeles 1982	Cape Town 2005 (This Study)
b_{sp} (%)	49	70	59	78	79
b_{ap} (%)	26	26	27	12	4
b_{sg}(%)	19	0	8	4	5
b_{ag} (%)	6	4	6	6	9

Cape Town data is based on winter data of 2005 since all these studies were done during winter time.

5.7 Development of Real-Time Visibility Forecasting Models using Multiple Regression Models

Table 5-6 shows the results of real-time visibility model development using multiple linear regression techniques. In six cases the adjusted regression coefficients are observed to reasonable higher after simple multiple regression and variable selection. After influential observations and outliers are removed from the data, the adjusted regression coefficients increased significantly with summer west data having the maximum regression coefficient of 0.838 confirming a strong relationship between the dependent variable and independent variables. In all six cases, there were no significant improvements in the regression coefficients when variable selection methods were employed. This was a result of stepwise regression accepting all the six independent variables used. These results compared well with results of visibility forecasting models development conducted elsewhere. In a study done in Taipei by Yang, an adjusted regression coefficient of 0.75 was observed [95]

Table 5-7 summarizes the regression efficiencies in equation 4.8 for all the six cases. After these regression efficiencies were obtained, equation 4-8 was used to compare forecasted visibility versus observed visibility from measurements using the light extinction coefficient model. It is also interesting to note that for the same direction (e.g. west) but different season, the regression efficiencies are different. This confirms that physical and chemical properties of air pollutants change from season to season.

Table 5-6: Results of various multiple regression techniques in the development of the real-time visibility forecasting models.

Season	Direction	Multiple Linear Regression	Variable Selection Methods	MLR Diagnostics Methods
		R-adj	R-adj	R-adj
Winter	East	0.618	0.618	0.801
	North	0.658	0.659	0.750
	West	0.623	0.623	0.799
Summer	East	0.554	0.555	0.747
	North	0.721	0.721	0.832
	West	0.734	0.734	0.838

Table 5-7: Regression coefficients obtained from multiple linear regression methods were applied to visibility, air pollution and meteorological data.

Season	Direction	a_1	a_2	a_3	a_4	a_5	a_6	a_7
Winter	East	-6.920	-1.210	-0.716	-0.303	-.9.961	11.9	2.223
	North	-7.980	0.316	-0.562	-0.0124	-8.723	0.114	2.214
	West	-1.050	-1.140	1.49	-0.153	-9.452	6.013	2.317
Summer	East	-7.070	2.380	2.780	2.902	-8.911	3.290	2.002
	North	-12.20	2.110	-0.843	-0.843	-0.7.08	14.6	2.132
	West	-11.50	-1.090	1.82	-0.351	-5.910	10.2	2.150

The true values of columns a_1 to a_6 are the values multiplied by 10^{-3}

5.8 Forecasting of Atmospheric Visibility

Once the real-time visibility forecasting models were developed from multiple linear regression methods, the models were used to compare forecasted visibility with observed visibility. Atmospheric visibility was forecasted every hour between 08:00 and 18:00 each day with the aforementioned multiple regression model. Based on two hundred and fifty three effective forecasted atmospheric visibility data from October 07th to October 30th, the correlation coefficient of the forecasted visibility was 0.896 (see figure 5.12). In general the, the variation of forecasted atmospheric visibility was consistent with the observed atmospheric visibility although a mean error was 4.9 km was observed.

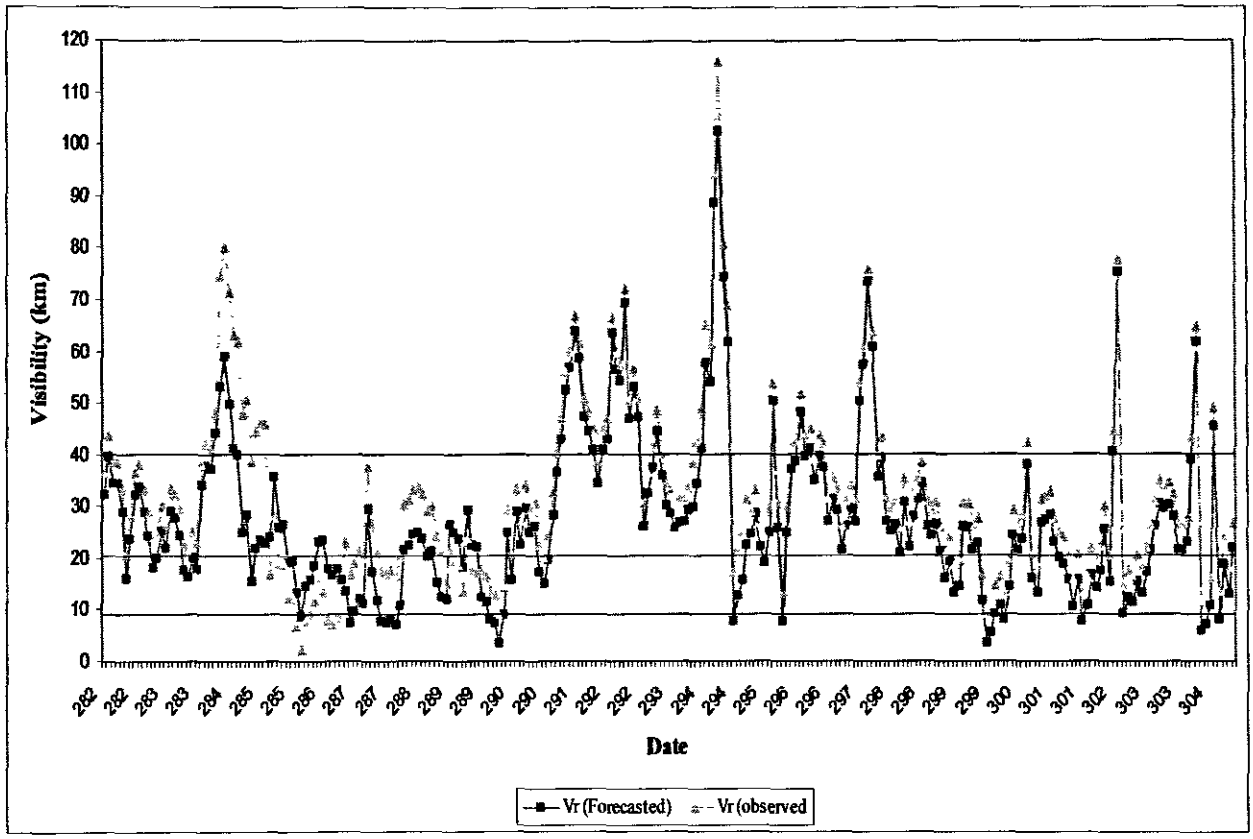

Figure 5-12: Comparison of forecasted visibility versus observed visibility.

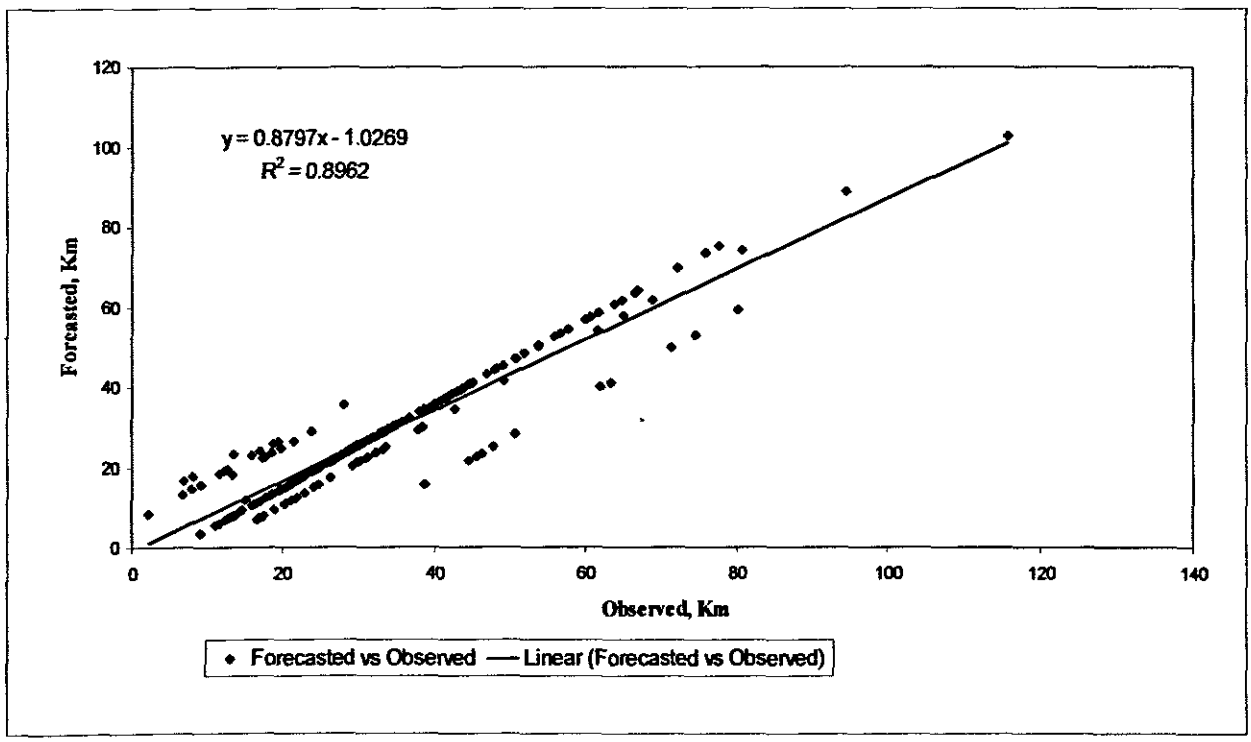

Figure 5-13: Forecasted visibility versus observed visibility.

5.9 Results of Haze Index Development

The application of equation 4.14 as well as the four arguments listed under section 4.5 to a visibility range of 0 – 70 km's provide means of developing a haze index scale. Table 5-8 is a result of this application. Based on the arguments given under section 4.5, it has five visibility descriptors which qualitatively communicate the extent of visibility. Table 5-9 summarises the visibility descriptors and their applicable visibility ranges based on the arguments on section 4.5. The haze index is a quantitative measure of visibility degradation. Therefore for a given visual range there will be a quantitative as well as a qualitative assessment of visibility degradation.

For example, if the visual range is 16 km, it falls under the descriptor ***Good,*** and has a haze index value of 4.8. Thus in terms of a Haze Index this visual range of 16 km is interpreted as 16 (good).

Table 5-8: Haze Index based on visual range, with visibility descriptors.

Haze Index (H_i)	5	4	3	2	1
Visibility Index (V_i)	6	7	8	9	10
Visual Range (b, V_r)	$8.4 \leq Vr \leq 13$	$13 \leq Vr \leq 20$	$20 \leq Vr \leq 30$	$30 \leq Vr \leq 45$	$45 \leq Vr \leq 70$
Visual Descriptor	Acceptable		Good		
Descriptor Thresholds based on Visual range	$8.4 < Vr < 20$		$20 < Vr < 70$		

Descriptor threshold boundaries for very poor, poor and good visibility conditions are based on modifying the last two arguments under section 4.5 so as to correspond to a Haze Index integer. For example the last arguments says that 2 km is regarded as an upper threshold boundary limit, however this corresponds to a haze index of 9.4. Therefore, to set it at 1.5 km, this results in a haze index of 1. Similarly for the third argument, 11 km sets the upper and lower boundary limits for poor and good visibility respectively. However 11 km corresponds to a haze index of 5.4. Therefore to set it at 8.4 km results in a haze index of 6.

The numerical value of the haze index indicates the extent of visibility degradation due to air pollution whilst the visibility descriptor part describes how acceptable are the visibility conditions. In the figure 5-12, 3 % of the forecasted visibility was less than 1.5 km (very poor visibility level), 6 % (poor), 32 % (acceptable) and 55 % (good) and 4 % was above 70 km (excellent).

Table 5-9: Proposed visibility descriptors.

Category (Descriptor)	**Visual range**
Excellent (E)	> 70 km
Good (G)	20 < Vr < 70 km
Acceptable (A)	8.4 < Vr < 20 km
Poor (P)	1.5 < Vr < 11 km
Very Poor (VP)	< 1.5 km

Chapter 6: Discussion

This study found digital image processing to be an effective method of estimating visual range. Estimated uncertainties associated with light extinction coefficient from contrast measurements were observed to be lower than 12 % in winter and lower than 9 % in summer. These uncertainties are significantly lower when compared to those observed in other methods used to estimate light extinction. Molenar for example reported uncertainties in the range of 30 to 100 % for contrast measurements using slide densitometry methods and uncertainties less than 15 % for light extinction measurements using a Transmissometer [79].

Although a limitation in this study was that the calibration of visual range estimates by digital image processing was performed by using the light extinction coefficient model, there is a strong agreement between visual range estimates from both methods particularly during midday. In the calibration curves generated by comparison of visual range estimates from digital image processing versus visual range measurements from the light extinction model, high correlation coefficients were observed.

During midday (11:00 and 13:00) there is good agreement between visual range estimates from both methods. This is inline with suggestions made by Malm suggesting that the light extinction model is only effective midday between 10:00 and 14:00 [64]. This is attributed to the effect of the sun angle. In the mornings and afternoons, the sun is lower in the east (morning) and west (afternoon). The sun being lower in the sky and light having further to travel through the particles in the haze, increase in light scattering occurs. Hence the estimates from image processing were corrected for sun angle. The situation in the morning and afternoon improved significantly after the DIP visual range estimates were corrected for sun angle. It has also been demonstrated that inherent contrast remains constant as the subject moves away from the target object at a given time. The results clearly demonstrate that C_o remains constant as the subject moves 2.8 km away from the target object. A standard deviation of 0.0001 was observed in the plotted C_o data.

Diurnal variations in the light extinction coefficient (b_{ext}) for winter months suggest that visibility conditions are worse in the mornings and afternoons. Thus high b_{ext} values are observed in the morning and afternoons. During midday b_{ext} values are low. These high b_{ext} (low Vr) values in the mornings and afternoons are due mainly to vehicle emissions.

In this study it was revealed that in Cape Town light attenuation is dominated by particle scattering more than anywhere else were light attenuation studies were performed. Cape town is observed to have a high percentage of particle scattering (% b_{sg} = 79 %) when compared to other cities such as Los Angeles (% b_{sg} = 78 %) and Sydney (% b_{sg} =70 %). These studies where done two decades ago, suggesting that in the present these percentages are likely to be lower because of interventions introduced to lower air pollution in those areas.

The study was also successful in developing real-time visibility forecasting models using multiple linear regression, variable selection and model diagnostic methods. In all six cases (models for two seasons and three directions), over 74 % of variability in visual range was explained by its linear relationship with air pollution and meteorological variables included in equation 4.8. This was achievable through the removal of influential observation and outliers by model diagnostic methods. Results also reveals that there is no significant increase in the regression coefficients after variable selection methods were applied because no variables were removed in all six models. However after model diagnostics were applied, there was a significant increase in the regression coefficients. It was possible to remove influential observations and outliers due to a high number of data points in all six cases.

Results from this study also revealed that for the same direction (e.g. west) but different seasons, the regression constants differ significantly. These regression constants give an indication of how efficient do pollutants scatter or absorb light as well as how influential are meteorological variables towards visibility degradation. Because of this, they are often referred to as regression efficiencies. Different seasons present different patterns of air pollution. The summer months in Cape Town are characterised by a high south-easterly air flow. This is caused by a ridging anticyclone over the south Atlantic [96]. This means high wind velocity and consequently high atmospheric turbulence which dilutes and disperses pollutants

efficiently. During the winter months the wind is generally from the north-west. This is caused by a pre-frontal system that also causes low temperatures and overcast conditions. The high wind velocity again performs a diluting function on pollutants in the area. This cause air pollution emission rates to fluctuate from season to season. Economical as well social factors also contribute to changes in air pollution patterns. This has an influence on physical and chemical properties of pollutants and consequently air pollution concentrations. Thus, the regression constants vary from season to season.

Results of visibility forecasting using the developed real-time forecasting visibility models demonstrates a strong relationship with measured visibility. A regression coefficient of 0.896 was achieved by plotting forecasted visibility versus measured visibility. However a systematic error was observed which may be attributed to uniform visibility conditions experienced in that period when visibility forecasting was performed. Therefore for similar observed visual range values, a series of forecasted visual range values was observed.

This study proposes a novel yet simple haze index scale as a means of reporting the extent of visibility degradation in Cape Town, but applicable, with minor adaptations, to any city or area of interest. With its two components (Haze Index and visibility descriptor) this haze index scale provides a linear interpretation of perceived visibility degradation by means of communicating visual range measurements using a numerical scale as well as the level of visibility degradation. The level of visibility degradation is based on the sampled images. While there is no one definition of visibility that meets all the criteria of "seeing" of landscape features, this haze index is based on a number of arguments based on fundamental laws (e.g. Rayleigh scattering) and accepted means of assessing visibility. Due to this lack of a uniform definition of visibility, a number of indices have evolved. Extinction, in the form of inverse mega meters (Mm^{-1}), is proportional to the amount of light lost as it travels over a million meters and is most useful for relating visibility directly to particle species concentrations, while deciviews are related to extinction but scaled in such a way that it is perceptually correct. For example, a one deciview change on a 20 deciview day will be perceived to be the same as on a 5 deciview day [97]. However this is not the case for extinction or visual range. For reference, Figure 6.1 compares the deciview index (*Dv*) to the haze index (*Hi*) developed in this study for a range of

light extinction and visual range values. For instance, 10 Mm^{-1} corresponds to about 400 km visual range and 0.0 dv, while 1000 Mm^{-1} is about 4 km visual range and 46 dv.

b_{ext} (Mm^{-1})	10	20	30	40	50	70	100	200	400	500	700	1000
VR (km)	400	200	130	100	80	60	40	20	10	8	6	4
Dv	0	7	11	14	16	19	23	30	37	39	42	46
Hi	1	1	1	1	1	2	3	4	5	6	6.5	7.5

Insignificant Change in visibility degradation

Significant Change in visibility degradation

Visibility degradation increases exponentially, this change is reflected in the *Hi*

Figure 6.1: Comparison of different measures of visibility: extinction (Mm-1), deciview (dv), and visual range (km) [7].

From figure 6.1, it is observed that there is a significant change in *Dv* of about 16 deciviews, for a visual range change form 400 km to 70 km. Theory however suggests that the human eye can not detect significant changes in visibility degradation from 400 km to 70 km. This theory is supported by *Hi*, which simply treats any visual range above 70 km with a haze index value of 1 (*Hi* = 1). Furthermore, a visual range change from 8 km to 4 km is very noticeable.

Chapter 7: Conclusions and Recommendations

This study shows that the digital image processing method, as developed during the work reported on, is an effective method of measuring visibility as compared to conventional methods such as slide densitometry or using a Transmissometer. The percentage uncertainty associated with b_{ext} estimates for summer and winter from digital image processing were low compared to b_{ext} estimates from slide densitometry or using a Transmissometer. In addition, the equipment required for the DIP method of measuring visibility is considerably less costly than a Transmissometer, and provides an objective and acceptably precise measure of visibility considerably more representative of the visibility of actual scenic vistas of, for example, the mountains surrounding the City of Cape Town.

This study has also confirmed that the effect of sun angle on visibility cannot be ignored. It has been shown that as the day progresses, inherent contrast values varies with the time of the day as the sun angle change due to the sun moving from east to west. Thus illumination of the target object varies with the angle of the sun. In addition, correction for sun angle in the DIP estimates improved the visual range estimates during the morning and afternoons when compared against b_{ext} model measurements.

The study successfully developed real-time visibility models that use air pollution and meteorological variables. In all six cases (two seasons: winter and summer, three directions: east, north and west), after using model diagnostics, the adjusted regression coefficients were all above 0.70, thus confirming the strong relationship between visibility, air pollution and meteorological variables used in the models. The advantage of using these models lies in their input variables. The model uses ambient data as well as meteorological data which are readily available from daily ambient monitoring stations. Thus, the nature of these models allows for a measure of visibility to be calculated using ambient pollution data and meteorological data, thus making it possible, when combined with pollution and meteorological forecasting models, to forecast visibility continuously. Furthermore, it has been shown that the visibility forecasting models provide accurate results with a high regression coefficient of 0.986 between forecasted visibility and observed visibility.

The haze index scale developed in this study differs significantly from conventional visibility scales currently in use. It recognizes that observed visibility is strongly non-linear with respect to visual range. Thus it takes into account the interpretation of visual range as well as the extent of visibility impairment by making use of arguments based on theory and experienced visibility (human observation).

The use of visibility forecast models directly related to air pollution concentrations, and the proposed haze index and visibility scales enables the development of an air quality management plan that relates a desired (target) level of visibility to required air pollution reduction measures.

The visibility and haze indices proposed are significant improvements on visibility indices currently in use. Firstly, the visibility index presents a scale that is linear with respect to changes in perceived visibility whilst its exponential basis recognizes the non-linear relationship relative to visual range as a measure of visibility. Secondly, the haze index, based on the visibility index reflects the non-linear nature of visibility degradation in a simple linear scale.

The work of Luo et.al, has similar features to that presented in this thesis, but is limited by the use of human subjects for estimating visual range, limiting visual range measurements to poor visibility conditions, for distances less than about 10km.

Budgett and Mason's work on the other hand appears to lack calibration. The study is also not based on natural targets, therefore it is site specific. Therefore effort is required shift away from site-specific method into a method that is universal encompassing natural targets, and then a method for calibration needs to be devised.

Compared to the two studies described above, the digital image processing method presented in this study is simple and precise. However refinement of the method of calibration (using, for example, a transmissiometer) as well as the real-time visibility modeling is required. The major advantages of the DIP method are that it has a firm theoretical basis, it is not site specific, and it is based on comparatively inexpensive image capturing equipment. It is also not restricted to poor visibility conditions, and

is thus sensitive to the visibility range bounded by Rayleigh scattering as well as zero visibility.

7.1 Further Research Issues

This study has identified the following issues as requiring further research:

- Use of Transmissometer measurements to validate digital image processing outputs
- Seasonal air pollution sampling and chemical analysis to extend the database used to calculate b_{ext}
- The validation of haze and/or visibility forecasting against an extended database of measurements.
- Study the effect of size distribution of fine particulates on light extinction for local conditions
- Evaluation of a haze index scale based on the extraction of high frequency components in digital images using Fast-Fourier transforms or Sobel mask. The advantage of such an index scale is that it is based on ambient elements captured by an image.

APPENDICES

CONTENTS OF APPENDICES

APPENDIX A: Theoretical Analysis: Estimation of Light Attenuation from Contrast measurements

A.1 Derivation of underlying equation

The contrast of a given feature at a specific wavelength is determined by the radiance of that feature and the radiance of the background or adjacent feature against which is viewed. Target/Sky contrast is defined as the ratio of the difference between the feature (target) and the background sky radiance to the background sky radiance.

$$C = \frac{({}_tN - {}_sN)}{{}_sN} \tag{A.1}$$

where N stands for radiance, t and s represent target and background sky respectively. Two important definitions are:

Inherent Contrast: C_o The contrast of the target at zero distance

Apparent Contrast: C_r The contrast of the target as viewed at a distance r

For an atmospheric sight path with average extinction coefficient (b_{ext}), the apparent contrast (C_r) to an observer who is viewing an object of inherent contrast (C_o) is rigorously defined:

$$C_r = C_o\left(\frac{{}_sN_o}{{}_sN_r}\right)\exp(-b_{ext}r) \tag{A.2}$$

where ${}_sN_o$ and ${}_sN_r$ represent the radiance of the identical sky reference position as measured at the target location (distance = o) and at the observation point (distance = r) respectively [64].

Equation above can be rearranged to solve for b_{ext}:

$$b_{ext} = \frac{1}{r}\ln\left[\left(\frac{{}_sN_o}{{}_sN_r}\right)\times\left(\frac{C_o}{C_r}\right)\right] \tag{A.3}$$

Equation above can be simplified by defining a sky radiance ratio as:

$$R_n = {}_s N_o \Big/ {}_s N_r \tag{A.4}$$

Then

$$b_{ext} = \frac{1}{r} \ln\left(\frac{R_n C_o}{C_r}\right) \tag{A.5}$$

Thus the average light extinction coefficient can be calculated from measurements of apparent contrast (C_r) and target distance (r) provided estimates of inherent contrast (C_o) and sky radiance ratio (R_n) are made.

A.2 Extract of data for the calculation of Visual range from DIP data

I sky	Iobject	Cx	Co	Iosky	Isky	Rn	ln(Rn*Co Cx)	x	tx	bext	Vr
Unitless	Unitless	Unitless	Unitless	Unitless	Unitless	Unitless	Unitless	km	km^{-1}	km^{-1}	km
248.23	247.3	-0.0037	-0.4184	218.164	248.23	1	4.586	27	0.0274	0.1255	26 2
190 18	176.98	-0.0694	-0.4590	190.354	190.18	1	1.890	27	0.0274	0.0517	63 6
153 66	145 86	-0.0508	-0.4803	211.472	153.66	1	2.567	27	0.0274	0.0702	46.9
138.5	136.58	-0.0140	-0.3636	205.926	138.5	1	3 653	27	0.0274	0.0999	32.9
141 24	135 12	-0.0433	-0.3929	197.398	141.24	1	2.540	27	0.0274	0.0695	47.4
135.81	131.27	-0.0334	-0.3784	206.776	135.81	1	2.847	27	0.0274	0.0779	42.3
138.06	131 11	-0.0503	-0.3789	195.544	138.06	1	2.367	27	0 0274	0.0647	50 8
141.77	139.12	-0.0187	-0.3469	217.202	141.77	1	3.348	27	0.0274	0.0916	35.9
145.07	136.83	-0.0568	-0.3578	216.492	145.07	1	2.241	27	0.0274	0.0613	53.7
138.34	137.89	-0.0033	-0.3716	212.104	138.34	1	5.166	27	0.0274	0.1413	23.3
137.01	130.02	-0.0510	-0.3683	224.438	137.01	1	2.470	27	0.0274	0.0676	48.7
236.16	236.1	-0.0003	-0.4184	218.164	236.16	1	7.327	27	0.0274	0.2005	16.4
193.6	183.05	-0.0545	-0.4590	190.354	193.6	1	2.114	27	0.0274	0.0578	56 9
151.32	134.52	-0.1110	-0.4803	211.472	151.32	1	1.799	27	0 0274	0.0492	66 9
140.39	124.26	-0.1149	-0.3636	205.926	140.39	1	1.535	27	0.0274	0.0420	78.4
137.87	127.54	-0.0749	-0.3929	197.398	137.87	1	2.016	27	0.0274	0.0552	59.7
143 03	135.89	-0.0499	-0.3784	206.776	143.03	1	2.394	27	0.0274	0.0655	50.2
137.78	131.84	-0.0431	-0.3789	195.544	137.78	1	2.524	27	0.0274	0.0690	47.7
146.94	135 22	-0.0798	-0.3469	217.202	146.94	1	1 861	27	0.0274	0.0509	64 6
138 48	129.11	-0.0677	-0.3578	216.492	138.48	1	2.112	27	0 0274	0.0578	57.0
137 67	127.41	-0.0745	-0.3716	212.104	137 67	1	2 039	27	0 0274	0.0558	59 0
143 6	127.39	-0.1129	-0.3683	224.438	143.6	1	1 629	27	0 0274	0.0446	73 8
215 81	215.3	-0.0024	-0.4184	218.164	215.81	1	5.187	27	0 0274	0.1419	23.2
174 13	163.25	-0.0625	-0.4590	190.354	174.13	1	2.083	27	0.0274	0.0570	57.7
149 38	134.96	-0.0965	-0.4803	211.472	149.38	1	1.952	27	0.0274	0.0534	61.6
142 02	127.67	-0.1010	-0.3636	205 926	142.02	1	1.652	27	0.0274	0.0452	72.8
143 96	129.74	-0.0989	-0.3929	197.398	143.96	1	1.696	27	0.0274	0.0464	70.9
141 58	129.91	-0.0824	-0.3784	206.776	141.58	1	1.903	27	0.0274	0.0521	63.2
146 95	133 68	-0.0903	-0.3789	195.544	146.95	1	1 720	27	0.0274	0.0471	69 9
137.08	129 63	-0.0543	-0.3469	217.202	137.08	1	2 314	27	0.0274	0 0633	52 0
139.97	126.28	-0.0978	-0.3578	216.492	139.97	1	1.733	27	0.0274	0.0474	69 4
135.02	124.15	-0.0805	-0.3716	212.104	135.02	1	1.981	27	0.0274	0.0542	60.7
143.92	128.47	-0.1074	-0.3683	224.438	143.92	1	1.677	27	0.0274	0.0459	71 7
252.01	249.89	-0.0084	-0.4184	218.164	252.01	1	3.762	27	0.0274	0.1029	32 0
210 43	209.87	-0.0027	-0.4590	190.354	210.43	1	5.050	27	0.0274	0.1382	23 8
165 75	163.87	-0.0113	-0.4803	211.472	165.75	1	3.989	27	0 0274	0 1091	30.2
138.6	135.5	-0.0224	-0.3636	205.926	138.6	1	3.184	27	0.0274	0.0871	37.8
142.7	135.94	-0.0474	-0.3929	197.398	142.7	1	2.440	27	0.0274	0.0668	49 3
141 77	131.73	-0.0708	-0.3784	206.776	141.77	1	2.053	27	0.0274	0.0562	58.6
140 38	134.64	-0.0409	-0.3789	195.544	140.38	1	2.558	27	0 0274	0.0700	47.0
136 39	123 52	-0.0944	-0.3469	217.202	136.39	1	1 767	27	0 0274	0.0484	68.1
147.16	132.14	-0.1021	-0.3578	216.492	147.16	1	1.640	27	0 0274	0.0449	73.3
145.72	129 39	-0.1121	-0.3716	212.104	145.72	1	1.574	27	0.0274	0.0431	76.4
138 56	123.95	-0.1054	-0.3683	224.438	138.56	1	1 733	27	0.0274	0.0474	69 4
136 77	129 89	-0.0503	-0.4184	218.164	136.77	1	2.585	27	0 0274	0 0707	46 5
134 46	142 42	0.0592	-0.4590	190.354	134.46	1	2.564	27	0.0274	0.0778	42 8
141 86	137.2	-0.0328	-0.4803	211.472	141 86	1	3.082	27	0 0274	0.0843	39.0
138.82	136.01	-0.0202	-0.3636	205.926	138.82	1	3 283	27	0.0274	0.0898	36.6
133.93	135 55	0.0121	-0.3929	197.398	133.93	1	3.455	27	0.0274	0.0876	37.4
132 28	128.57	-0.0280	-0.3784	206.776	132.28	1	3 049	27	0.0274	0.0834	39.5
140.35	135.81	-0.0323	-0.3789	195.544	140.35	1	2 792	27	0.0274	0.0764	43.1
142.99	133.46	-0.0666	-0.3469	217.202	142.99	1	2.068	27	0 0274	0.0566	58 2
142 58	123.96	-0.1306	-0.3578	216.492	142.58	1	1 425	27	0.0274	0 0390	84 4
155 87	136.15	-0.1265	-0.3716	212.104	155.87	1	1.385	27	0.0274	0.0379	86 8
146.16	138.37	-0.0533	-0.3683	224.438	146.16	1	2.362	27	0 0274	0.0646	50 9
150 57	135.95	-0.0971	-0.4184	218.164	150.57	1	1.831	27	0.0274	0.0501	65.7
154 43	127.13	-0.1768	-0.4590	190.354	154.43	1	1.163	27	0 0274	0.0318	103.4
152.61	134.95	-0.1157	-0.4803	211.472	152.61	1	1 749	27	0.0274	0.0479	68 8
149 66	130.07	-0.1309	-0.3636	205.926	149.66	1	1.341	27	0.0274	0.0367	89.7
152.78	129.87	-0.1500	-0.3929	197 398	152.78	1	1 219	27	0 0274	0.0334	98.6
145.09	127 39	-0.1220	-0.3784	206.776	145.09	1	1.486	27	0 0274	0.0407	80.9
146.23	133.53	-0.0868	-0.3789	195.544	146.23	1	1.764	27	0.0274	0.0483	68.2
140.11	128.99	-0.0801	-0.3469	217.202	140.11	1	1 904	27	0 0274	0 0521	63 2
138.39	128 06	-0.0746	-0.3578	216.492	138.39	1	2.015	27	0 0274	0 0551	59 7
138 07	129.79	-0.0600	-0.3716	212.104	138.07	1	2.253	27	0.0274	0.0616	53 4
136 61	122.37	-0.1042	-0.3683	224.438	136 61	1	1.759	27	0.0274	0.0481	68.4
210 45	207.37	-0.0146	-0.4184	218.164	210.45	1	3.389	27	0.0274	0.0927	35 5
166.23	152.22	-0.0843	-0.4590	190.354	166.23	1	1.830	27	0.0274	0.0501	65 7
147 52	130 25	-0.1171	-0.4803	211 472	147.52	1	1.772	27	0 0274	0.0485	67 9
140.48	125.14	-0.1092	-0.3636	205 926	140 48	1	1.585	27	0 0274	0 0434	75 9
138 67	125.94	-0.0918	-0.3929	197.398	138.67	1	1 807	27	0.0274	0.0494	66 6
138.63	126.49	-0.0876	-0.3784	206.776	138.63	1	1 863	27	0 0274	0 0510	64 6
141 23	132.17	-0.0642	-0.3789	195 544	141.23	1	2 101	27	0 0274	0.0575	57 2
143.2	133.88	-0.0651	-0.3469	217.202	143.2	1	2 090	27	0.0274	0 0572	57.6
140.99	128.94	-0.0855	-0.3578	216.492	140.99	1	1 861	27	0.0274	0.0509	64.7

APPENDIX B: Implications of assumptions made in the Derivation of the Koschmeider Equation

Assumption 1:

The effect on visual range of inhomogeneous illumination, such as that under scattered clouds, is difficult to analyze by elementary methods. Limited experimental evidence indicates that this effect may not be great for short visual ranges (less than 50 km). Visual range has been found to correlate with the reciprocal of the scattering coefficient, bscat*, as illustrated in figure B-1. The correlation coefficients are commonly in the neighbourhood of 0.9, with values for bscat times Vr in the range 2 to 4 as compared to 3.9 in the Koschmieder equation. The studies were conducted in relatively polluted conditions. The effect of scattered clouds or differing sky brightness on visual range in clean areas should be further investigated.

Assumption 2:

The Koschmieder equation can be utilized in a non-homogeneous atmosphere (e.g., a ground level plume) if the extinction coefficient in and outside the plume is known. Otherwise, measurements of bext in areas with strong pollution gradients will produce inaccurate visual range estimates.

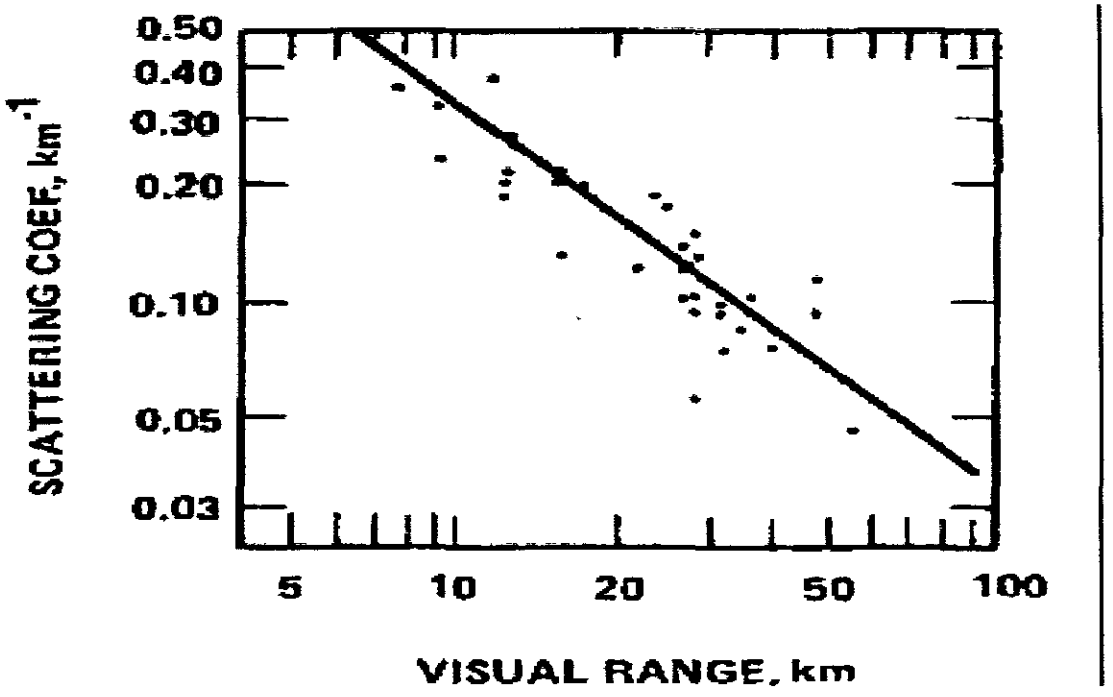

Figure B-1. Inverse proportionality between visual range and light scattering coefficient (bscat) measured at the point of observation. The straight line shows the Koschmieder formula for non-absorbing (bext =bscat) media, V = 3.9/bscat. The linear correlation coefficient for V and bscat is 0.89. [64]

Assumptions 3 & 4:
Requirements for horizontal viewing distance and curvature of the earth limit the validity of the Koschmieder calculation to cases where visual range is less than about 150-200 km (Figure B-2). Where no proper targets exist and the extinction coefficient is measured, however, the calculation of visual range is useful in expressing visual air quality in units (miles or kilometres) more readily comprehended by the layman.

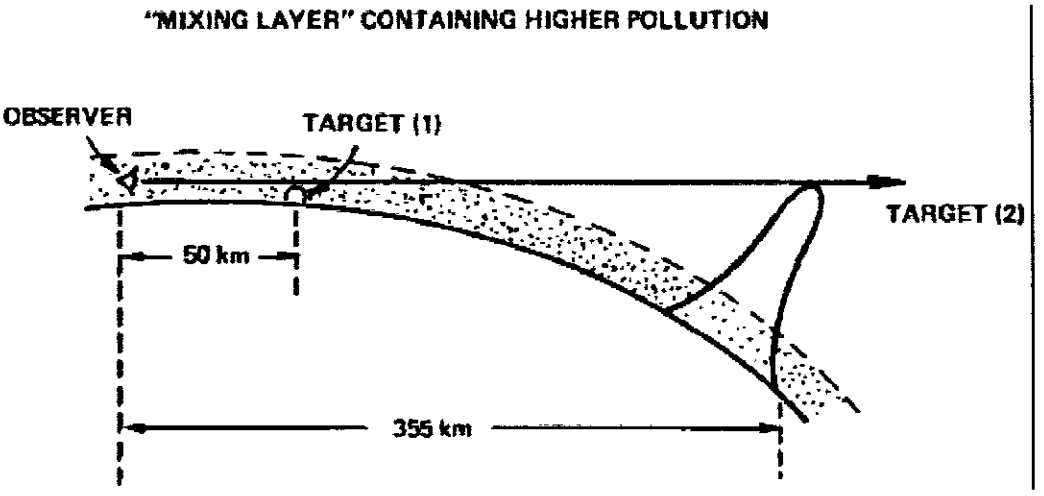

Figure B-2. Limitations of Koschmieder relationship. When visual range is short (1), extinction and illumination through sight path is uniform. When true visual range is high (2), Koschmieder equation underestimates visual range because extinction decreases with altitude and illumination (sun angle) at target is different from that at observer. (Dimensions and earth curvature exaggerated for clarity) **[64].**

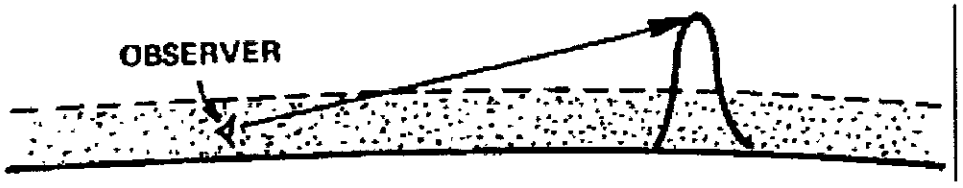

Figure B-3. Similarly, when viewing angle is not horizontal, extinction through the site path is non-uniform. Koschmieder equation will underestimate visual range **[64].**

Assumption 5:
The visual range for non-black objects depends strongly on initial contrast, which in turn depends on amount and angle of illumination or if at night depends on the power of the light source. As a result of this ambiguity, visual ranges for non-black objects or for lights at night cannot be related simply to each other or to optical air quality.

Assumption 6:
The effects of target size, texture, and sensitivity of observer are related to the nature of human perception. In general the "visual range" for small targets or contrast detail is significantly less than that for large objects (Table B-1). [64]

				Visual range (km)	
Detail of objects	Angular size (minutes)	Characteristics sizes at 10 km (m)	Examples for a hillside at 10 km	West Vr = 100 km	East Vr = 20 km[b]
Very coarse (Form)	> 30'	> 100	Hills, valleys, ridgelines	79-100	16-20
Coarse (Line)	17-30'	50-100	Cliffs faces smaller valleys	76	15
Medium (Texture)	9-17'	25-50	Clumps of large vegetation, clearings on forested slopes	62	12
Fine (Texture)	< 9'	< 25	Individual large trees, clumps of small vegetation	22	4

Table B-1: Visual Range of Contrast Detail[a]. [a]Based on calculations using MTF model of eye-brain response and mathematical transformation of scenic features into a spatial frequency [98]. [b]Vr sit he assumed background visual range (for large black targets).

APPENDIX C: Comparison between typically Clear (less hazy) days and Hazy days in the Three Directions [East, North and West]

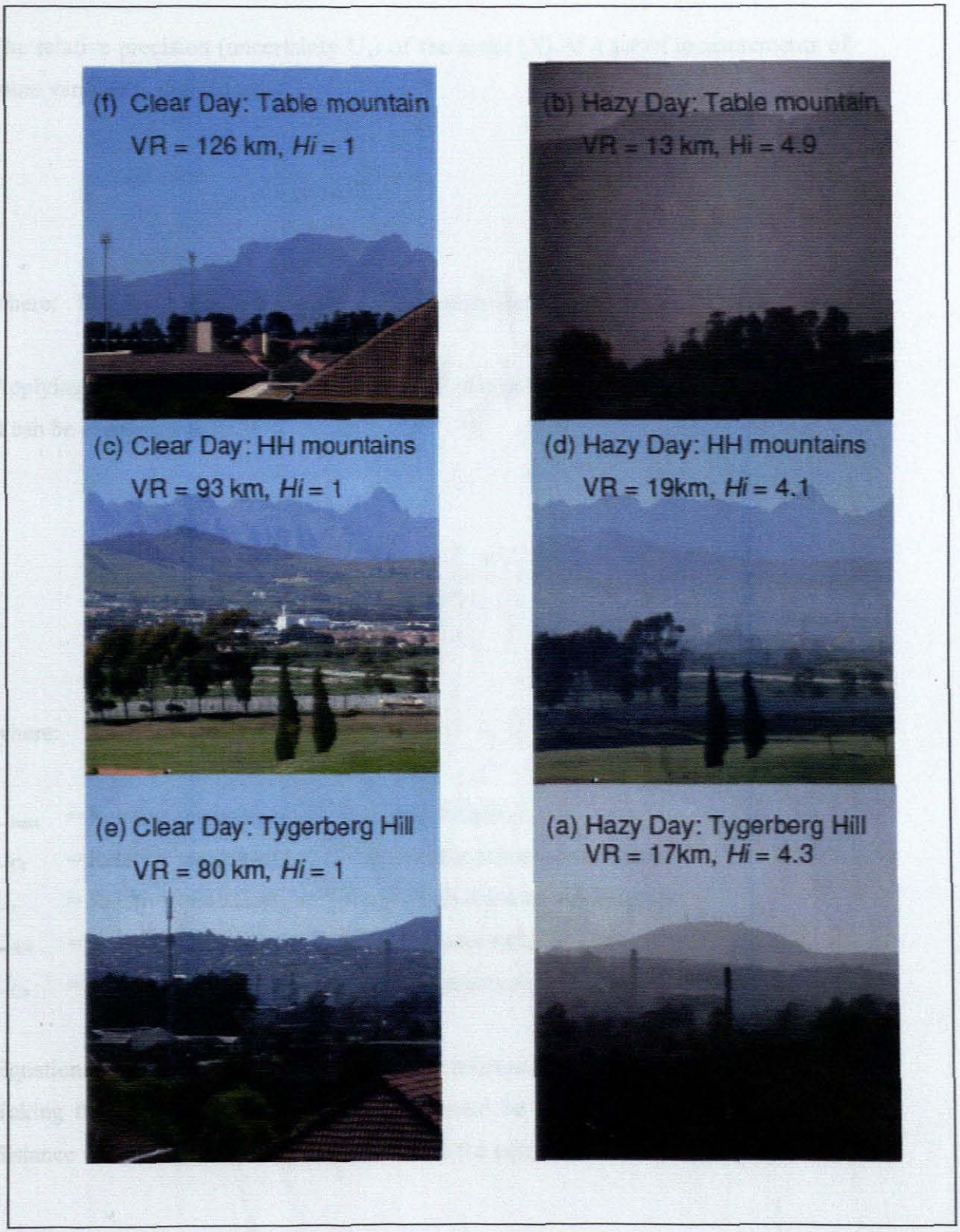

Figure C-1: Visual range estimates (Vr) estimates from digital image analysis, *Hi* is the haze index corresponding to the visual range in the image.

APPENDIX D: Derivation of Uncertainty in b_{ext} Computation by Digital Image Processing

The relative precision (uncertainty U_x) of the mean (X) of a set of measurements of some variable is defined as:

$$U_x = \frac{SD_x}{\overline{X}} \tag{D.1}$$

where: SD_x is the standard deviation of measurements

Applying standard procedures to equation 4.2, the propagation of uncertainty through it can be expressed as [77].

$$U_{bext}^2 = U_r^2 + \left[\frac{\left(U_{R_N}^2 + U_{C_o}^2 + U_{C_r}^2\right)}{\ln^2\left(\frac{R_N C_o}{C_r}\right)} \right] \tag{D.2}$$

where:

U_{bext} = Relative uncertainty of calculated extinction
U_{Cr} = Relative uncertainty of the apparent contrast measurement
U_r = Relative uncertainty of the sight path distance measurement
U_{RN} = Relative uncertainty of the sky radiance ratio estimate
U_{Co} = Relative uncertainty of inherent contrast estimate

Equation D.2 assumes that there are no correlations between any of the variables. Taking the uncertainty in r as zero (we should be able to measure the sight path distance with a very high degree of precision) the equation D.2 can be simplified to:

$$U_{bext} = \left[\frac{\left(U_{R_N}^2 + U_{C_o}^2 + U_{C_r}^2\right)^{0.5}}{\ln\left(\frac{R_N C_o}{C_r}\right)} \right] \qquad \text{(D.3)}$$

Equation D.3 shows that the actual values and uncertainties in R_n, C_o, and C_r are all equally important and cannot be ignored when estimating the uncertainty in calculated b_{ext}.

APPENDIX E: Equipment Used for Continuous Pollutant Sampling

Pollutant Sampled	Equipment Model Used	Principle of Operation
SO_2	API Model 100A	fluorescence of SO_2 due to absorption of Ultraviolet (UV) energy
NO_2	API Model 200A	measures the light intensity of the chemiluminescent gas phase reaction of nitric oxide [NO] and ozone [O_3]
O_3	API Model 400A	Based on the absorption of 254 nm UV light due to the internal electronic resonance of the O_3 molecule.
PM_{10}	TEOM Series 1400a PM-10 Monitor	Based on gravimetric analysis of particulate captured through a filter at a constant flow rate.

APPENDIX F: Outliers and Influential Observations

An outlier is a data point that is not fitted well by the regression model.
An influential observation is one that has a substantial impact on the model, i.e., if you removed the observation, the model would change.

F.1 Outliers:

There are a number of reasons why a data point may be an outlier:

- MEASUREMENT ERROR
- TRANSCRIPTION ERROR
- UNUSUAL EVENTS
- INCORRECT MODEL, ETC

An observation can be an outlier without being influential (and vice versa)

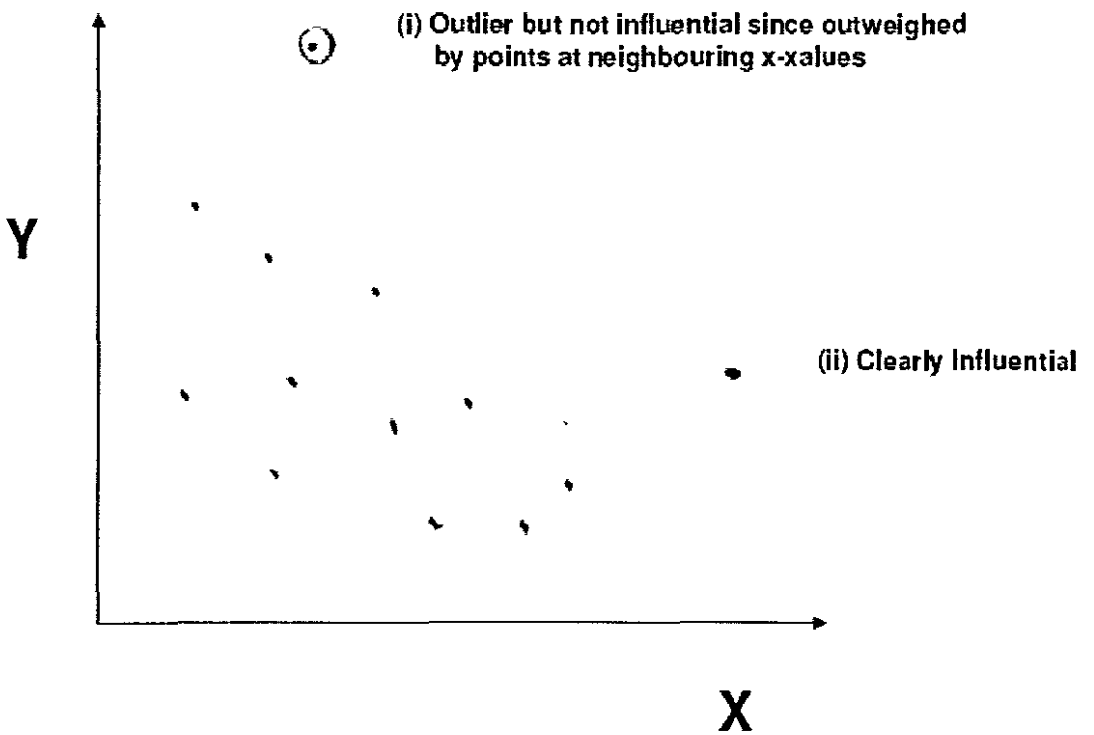

Outliers have extreme Y - values given the corresponding X-values and can be identified by large residuals. Plots of e_i *versus* X_i *and* e_i *versus* Y_i *are useful for identifying outliers.* We can also examine the Studentised residual, which equals the residuals divided by the standard error of the residuals. These studentised residuals follows a t-distribution with n-p-1 degrees of freedom, where

P = number of independent variables
= 1 for simple linear regression

Generally, we would consider studentised residuals which are greater than 2 (in absolute value) as being outliers.

F.2 Influential Observations

1. Cook's distance (D) = measure of the distance between the fitted regression coefficients with and without each observation

As a rule of thumb, you may use Cook's distance > 0.33 □ high influence.

2. Dfits $=e_i\sqrt{[h_i/(1-h)]}$ (F.1)

Large residuals and large h_i increase the value of Dfits. Dfits is in fact a scaled difference between predicted values for the ith case when the regression is estimated with and without the ith value.

A value for $|\text{Dfits}| > 2\sqrt{[k/n]}$, where a value of k = number of predictors (including the constant and n = sample size, may indicate high influence.

In Stata (statistical analysis software), the above diagnostics are generated by using the following statements:

- fpredict resstu, rstudent
- fpredict cooksd, cooksd
- fpredict dfits, dfits
- fpredict [dependent Var]hat
- list [independent var] [dependent var] resstu cooksd dfit

APPENDIX G: Inherent Contrast (C_o) Calibration Curves used to Calculate b_{ext}

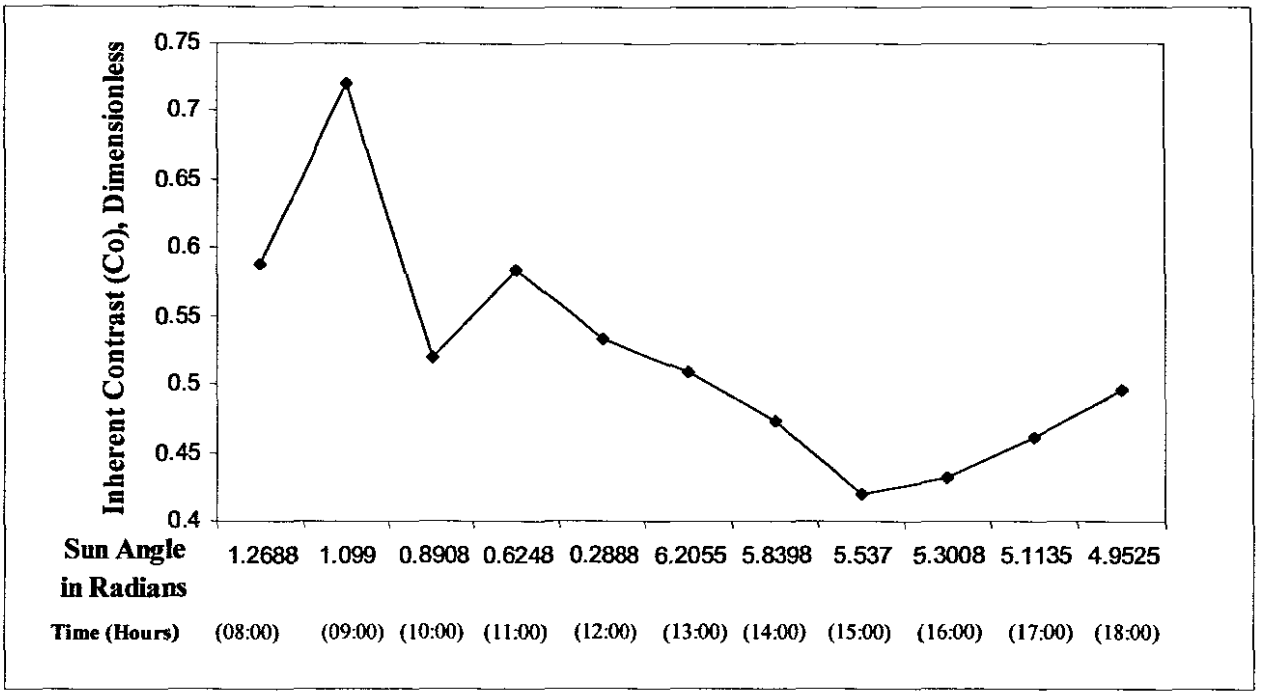

Figure G-1: Inherent contrast calibration curve for the west direction – Inherent contrast versus time of the day when images were sampled.

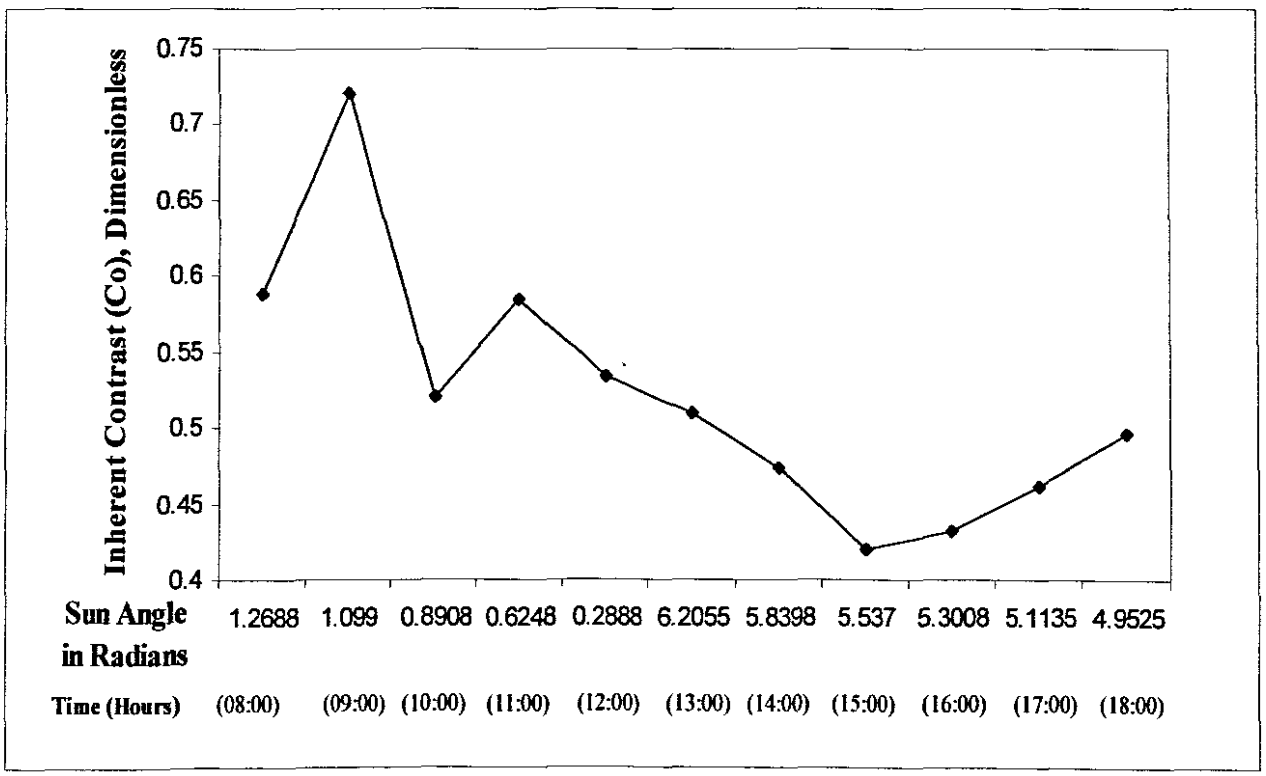

Figure G-2: Inherent calibration curve for the North direction – Inherent contrast versus time of the day when images were sampled.

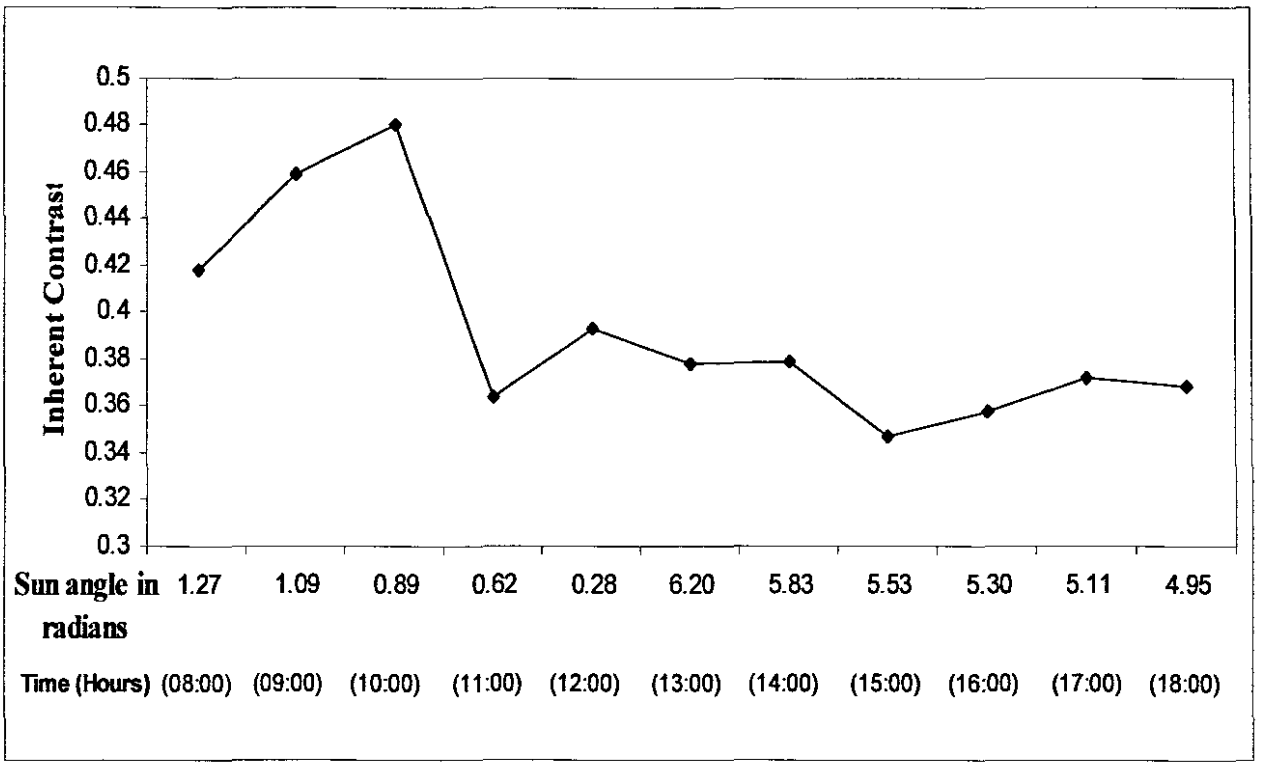

Figure G-3: Inherent calibration curve for the East direction – Inherent contrast versus time of the day when images were sampled.

APPENDIX H: Sun Angle Calibration Curves for Vr estimates using DIP

Graphs of Vr [DIP] vs. Vr [bext model]

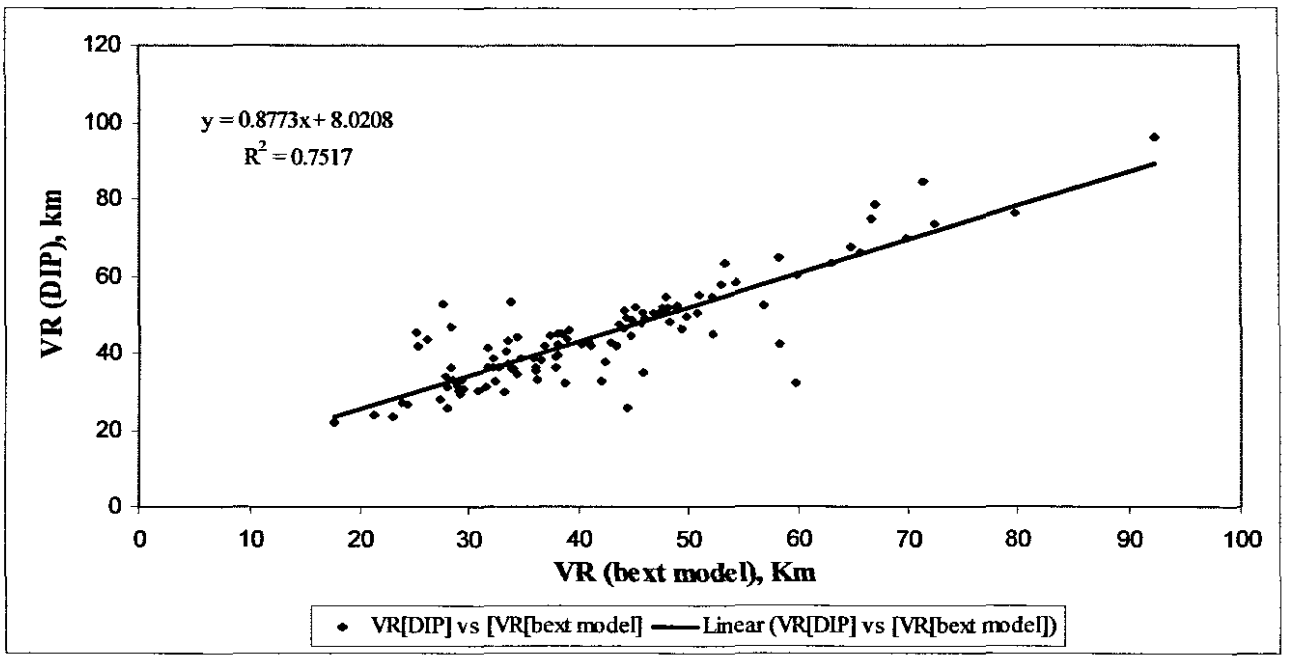

Figure H-1: Sun angle corrected calibration curve of VR DIP estimates - Visual Range (Digital Image Processing estimates) versus Visual Range from light extinction coefficient model. [Summer season and North direction].

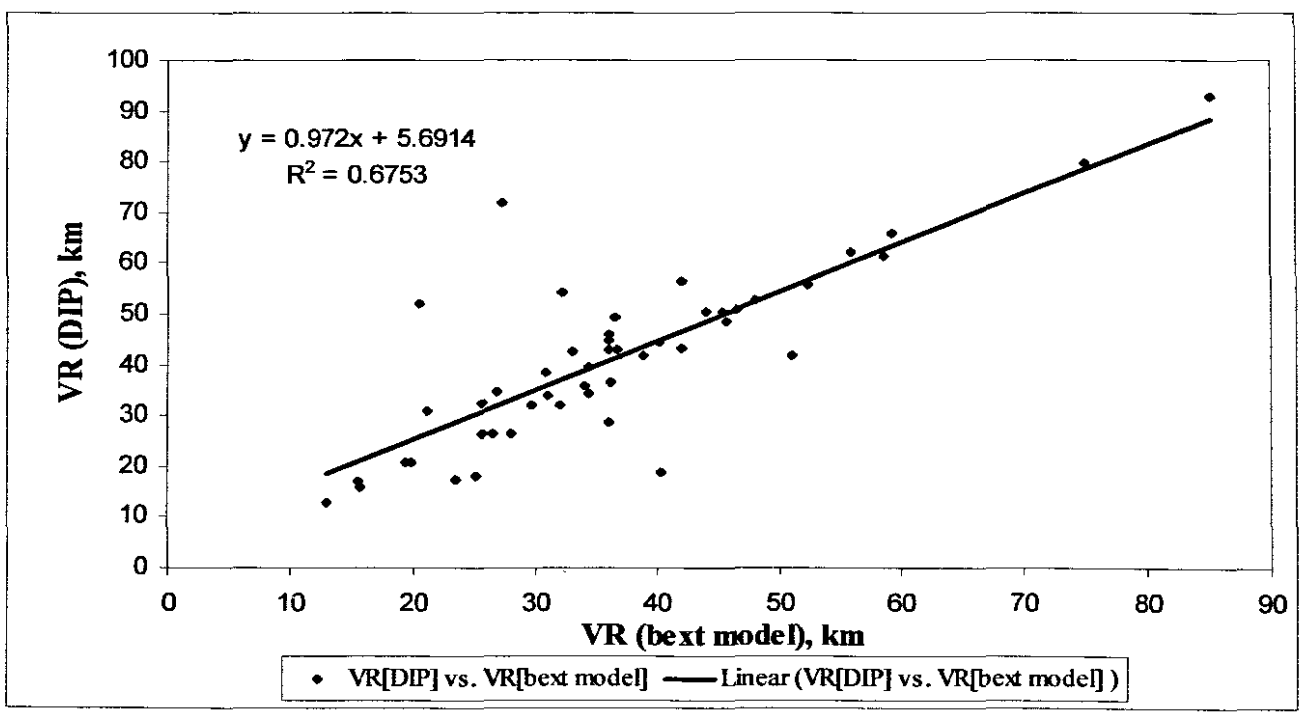

Figure H-2: Sun angle corrected calibration curve of Vr DIP estimates - Visual Range (Digital Image Processing estimates) versus Visual Range from light extinction coefficient model. [Summer season and west direction].

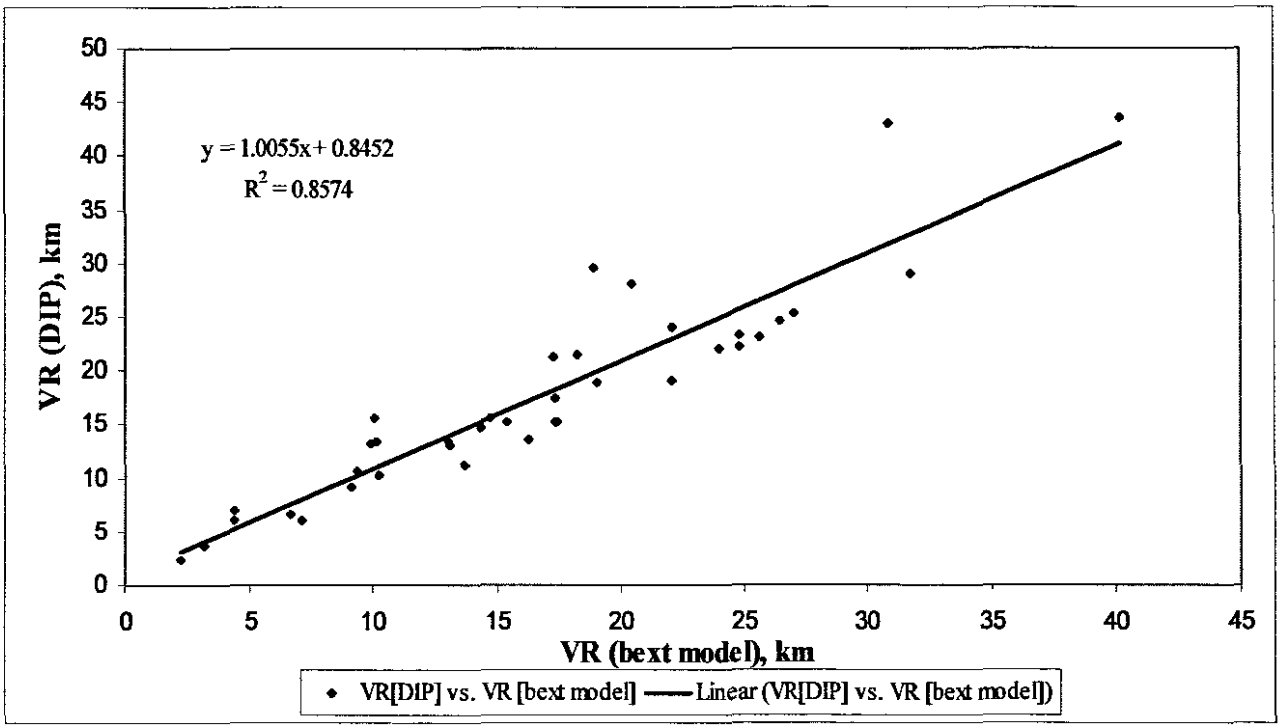

Figure H-3: Sun angle corrected calibration curve of Vr DIP estimates - Visual Range (Digital Image Processing estimates) versus Visual Range from light extinction coefficient model. [Winter season and east direction].

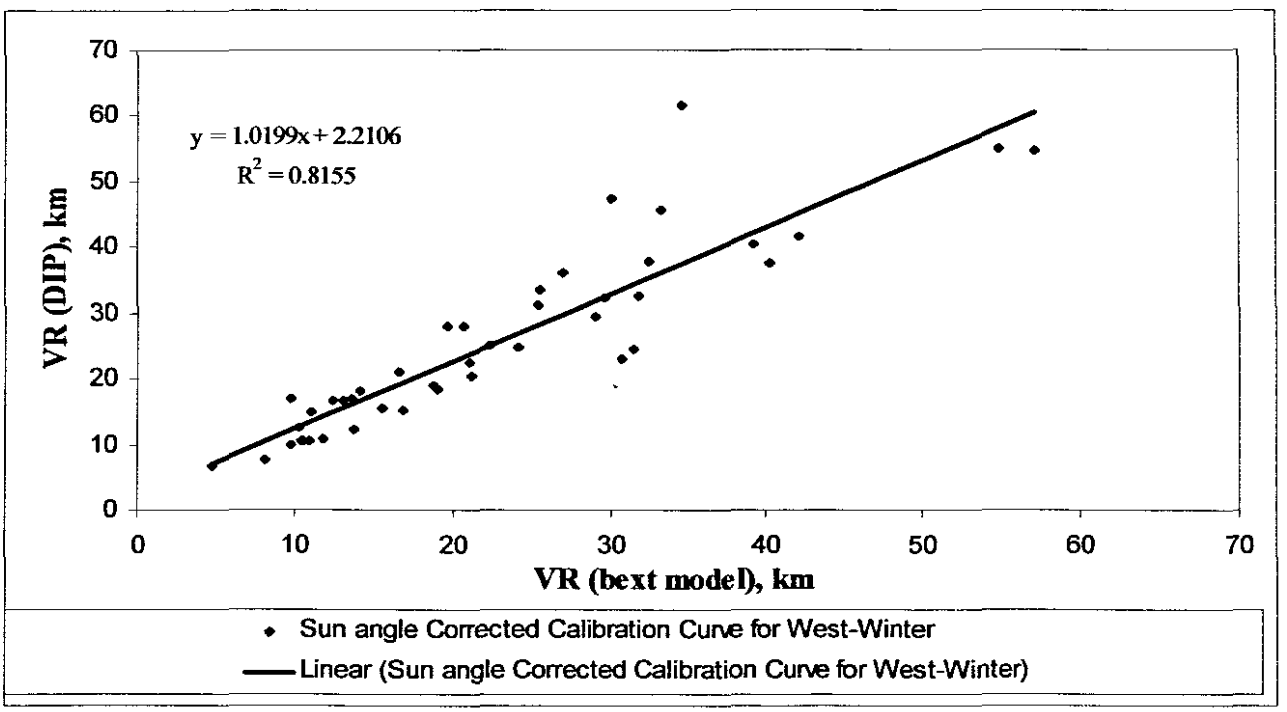

Figure H-4: Sun angle corrected calibration curve of VR DIP estimates - Visual Range (Digital Image Processing estimates) versus Visual Range from light extinction coefficient model. [Winter season and North direction].

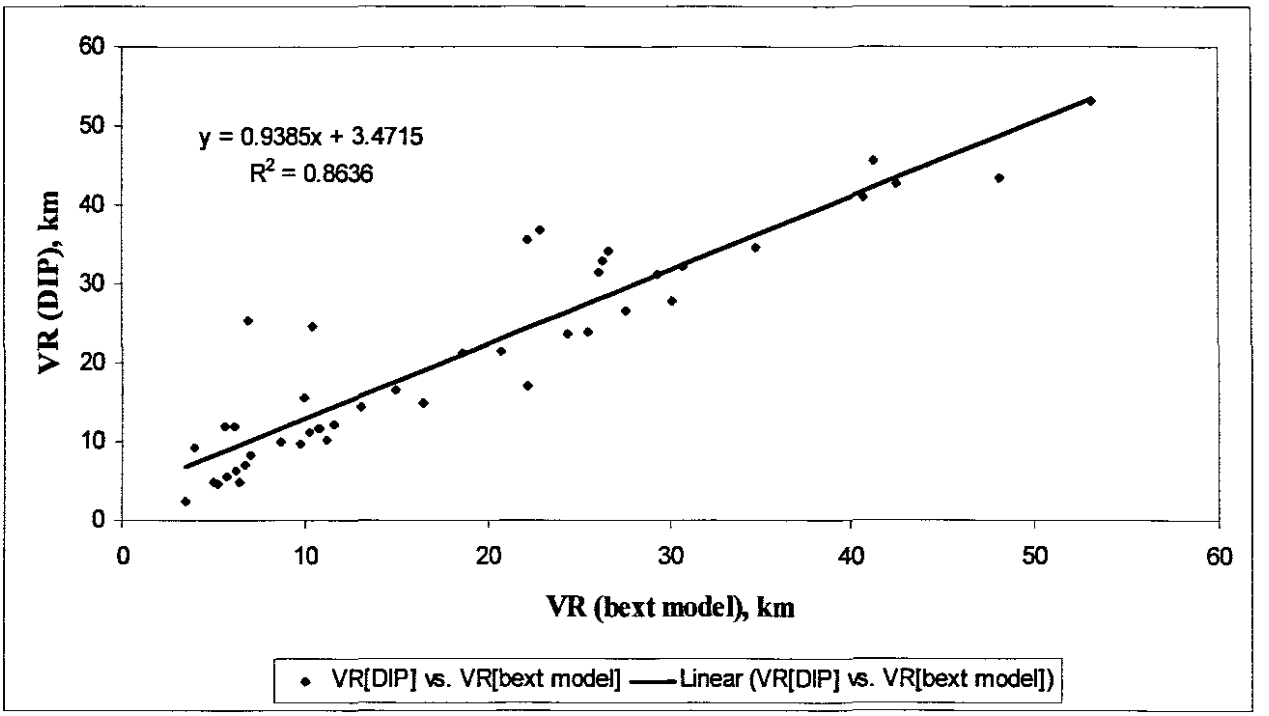

Figure H-5: Sun angle corrected calibration curve of Vr DIP estimates - Visual Range (Digital Image Processing estimates) versus Visual Range from light extinction coefficient model. [Winter season and west direction].

APPENDIX I: Commands used to perform Multiple Linear Regression in Stata Statistical Software

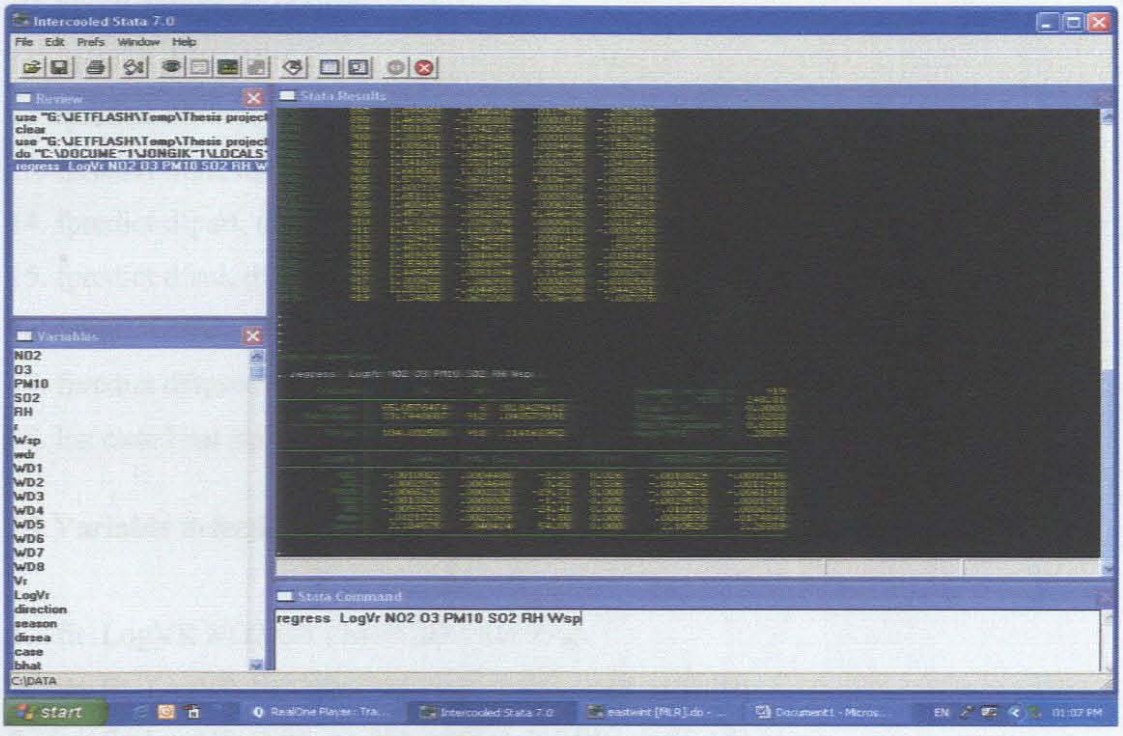

Figure I.1: A look at Stata software and its features.

As can be observed from figure 4.4, Stata software consists of four windows, they are command window, variable list window, command history window as well as results window. The command window allows the user to perform the desired tests on certain variables selected from the variables window and the results are displayed on the Stata results window. The Stata command history window allows the user to use previously executed commands.

I.1 Multiple Linear Regression

1. regress LogVR NO_2 O_3 PM_{10} SO_2 RH Wsp
2. fpredict bhat
3. fpredict seconf, stdp
4. fpredict sepred, stdf
5. gen lcl95 =bhat-2.101*seconf
6. gen ucl95 =bhat+2.101*seconf

7. gen lpl95 =bhat-2.101*sepred
8. gen upl95 =bhat+2.101*sepred
9. fpredict resstu, rstudent
10. fpredict cooksd, cooksd
11. fpredict dfits, dfits
12. fpredict dfnitro, dfbeta (NO_2)
13. fpredict dfoz, dfbeta (O_3)
14. fpredict dfpart, dfbeta (PM_{10})
15. fpredict dfsul, dfbeta (SO_2)
16. fpredict dfrel, dfbeta (RH)
17. fpredict dfspeed, dfbeta (Wsp)
18. list case bhat resstu cooksd dfits, nodisplay

I.2 Variable Selection

1. fit LogVR NO2 O3 PM10 SO2 RH Wsp
2. sw fit LogVR NO2 O3 PM10 SO2 RH Wsp, pr(0.10)
3. sw fit LogVR NO2 O3 PM10 SO2 RH Wsp, pr(0.10) hier
4. sw fit LogVR NO2 O3 PM10 SO2 RH Wsp, pe(0.10)
5. sw fit LogVR NO2 O3 PM10 SO2 RH Wsp, pe(0.10) hier
6. sw fit LogVR NO2 O3 PM10 SO2 RH Wsp, pe(0.08) pr(0.10) forward

I.3 Diagnostics

1. gen case =_n
2. drop if case == [CooksD > 0.33]
3. drop if case == [rstudent > □2□]
4. drop if case == [Dfits < 2/□n] (n = number of observation)
5. regress LogVR NO2 O3 PM10 SO2 RH Wsp

I.4 An extract from the data used for Multiple Linear Regression

NO2	O3	PM10	SO2	R	RH	Wsp	Wdr	VR	LogVr	Direction	Season
ug/m^3	ug/m^3	ug/m^3	ug/m^3	%	Fraction	m/s	Degrees	km	km	0=West, 1=North, 2=East	0=Winter, 1=Summer
60	11	67	42	73	0.73	2.1	30	52.47	1.72	2	0
81	29	50	58	59	0.59	4.2	350	78.16	1.89	2	0
55	48	44	33	63	0.63	4.2	350	57.51	1.76	2	0
19	55	32	20	51	0.51	3.9	360	77.82	1.89	2	0
18	56	43	22	53	0.53	4.6	310	67.26	1.83	2	0
20	55	44	23	71	0.71	6.0	310	75.63	1.88	2	0
30	48	39	24	52	0.52	4.9	330	105.49	2.02	2	0
35	40	59	26	54	0.54	6.6	300	124.03	2.09	2	0
30	42	62	26	63	0.63	7.0	310	109.04	2.04	2	0
35	35	50	24	73	0.73	5.5	320	112.72	2.05	2	0
35	30	52	20	80	0.8	6.0	320	133.32	2.12	2	0
36	21	18	17	88	0.88	7.5	190	54.92	1.74	2	0
37	29	36	19	81	0.81	7.5	180	43.70	1.64	2	0
23	44	24	16	75	0.75	8.9	170	84.22	1.93	2	0
17	47	27	14	73	0.73	8.8	170	133.00	2.12	2	0
10	51	23	13	65	0.65	8.8	170	148.70	2.17	2	0
10	47	27	14	68	0.68	9.7	170	147.61	2.17	2	0
11	44	27	14	70	0.7	9.9	180	93.76	1.97	2	0
15	46	30	16	71	0.71	9.5	180	96.31	1.98	2	0
20	44	37	16	66	0.66	9.8	170	78.83	1.90	2	0
28	30	39	16	65	0.65	11.3	170	82.26	1.92	2	0
31	22	33	16	63	0.63	10.1	160	62.23	1.79	2	0
30	31	42	20	60	0.6	4.6	190	31.72	1.50	2	0
14	60	31	16	54	0.54	4.1	140	28.40	1.45	2	0
38	49	49	21	47	0.47	5.2	150	64.06	1.81	2	0
31	63	40	23	45	0.45	5.0	170	55.94	1.75	2	0
36	61	44	26	39	0.39	4.5	150	81.51	1.91	2	0
28	49	37	25	37	0.37	3.8	170	67.66	1.83	2	0
26	46	40	24	37	0.37	2.8	180	96.74	1.99	2	0
25	43	40	20	46	0.46	4.3	190	84.80	1.93	2	0
24	41	34	18	69	0.69	4.1	220	78.42	1.89	2	0
30	34	33	17	67	0.67	4.8	333	184.08	2.26	2	0
55	10	43	29	81	0.81	3.7	170	64.09	1.81	2	0
31	33	28	25	63	0.63	4.4	150	63.01	1.80	2	0
22	33	26	22	59	0.59	3.2	170	46.59	1.67	2	0
25	44	28	25	52	0.52	2.1	200	73.18	1.86	2	0
24	46	26	26	36	0.36	1.8	200	50.90	1.71	2	0
26	48	28	27	30	0.3	2.0	180	41.56	1.62	2	0
30	45	39	28	31	0.31	2.5	210	64.57	1.81	2	0
40	42	43	29	37	0.37	4.8	170	42.99	1.63	2	0
36	45	45	29	52	0.52	5.8	160	32.30	1.51	2	0
30	42	48	26	63	0.63	6.2	150	40.25	1.60	2	0
36	31	38	21	78	0.78	5.2	210	53.35	1.73	2	0
16	41	42	17	94	0.94	5.5	310	38.15	1.58	2	0
12	43	39	15	93	0.93	4.5	310	50.97	1.71	2	0
8	50	55	14	84	0.84	4.7	320	45.43	1.66	2	0
8	41	55	14	77	0.77	5.5	310	59.93	1.78	2	0
6	58	75	14	60	0.6	5.8	320	52.69	1.72	2	0
5	58	65	16	60	0.6	6.9	290	65.78	1.82	2	0
17	47	101	17	61	0.61	6.2	300	49.02	1.69	2	0
9	52	66	16	60	0.6	8.2	300	50.44	1.70	2	0
10	46	69	15	59	0.59	9.6	290	66.07	1.82	2	0
16	37	62	15	72	0.72	8.0	310	60.80	1.78	2	0
18	34	45	15	80	0.8	7.0	310	82.26	1.92	2	0
15	46	30	14	94	0.94	2.3	330	114.47	2.06	2	0
9	51	34	14	87	0.87	3.9	320	67.75	1.83	2	0
12	51	42	15	83	0.83	4.1	290	80.09	1.90	2	0
9	51	46	14	75	0.75	3.1	350	117.20	2.07	2	0
10	36	48	13	65	0.65	4.2	290	89.67	1.95	2	0
14	48	39	13	57	0.57	5.4	300	72.00	1.86	2	0
17	49	48	15	54	0.54	5.5	290	77.40	1.89	2	0
19	45	41	18	51	0.51	6.3	310	74.22	1.87	2	0
23	39	47	18	50	0.5	5.0	300	71.65	1.86	2	0
31	31	42	17	53	0.53	4.5	310	69.47	1.84	2	0
32	28	53	15	62	0.62	4.3	320	94.55	1.98	2	0
30	46	43	19	65	0.65	3.9	330	69.19	1.84	2	0
19	49	46	17	59	0.59	4.8	310	61.66	1.79	2	0
17	51	46	18	50	0.5	5.3	310	64.56	1.81	2	0
18	52	54	17	50	0.5	6.2	300	67.96	1.83	2	0
17	40	78	16	49	0.49	6.9	300	60.54	1.78	2	0
18	50	108	17	48	0.48	7.9	290	43.08	1.63	2	0
18	47	121	18	51	0.51	7.8	290	26.89	1.43	2	0
33	33	47	19	58	0.58	6.8	300	68.26	1.83	2	0
55	21	65	32	86	0.86	4.9	240	53.59	1.73	2	0

References

3 Chan, Y.C., Simpson, R.W., Cohen, D.D., & Bailey, G.M. (1998) Source apportionment of visibility degradation problems in Brisbane (Australia) using multiple regression techniques, *Atmospheric Environment* pp. 3237-3250.

4 Jacobson, M.Z. (1999) Fundamentals of Atmospheric Modeling, Ch 10. Cambridge University Press, Cambridge.

5 Terblanche, P., Taljaard, J., Nel, R., & Grosser, E. (1996) Milnerton and Surrounding Areas Air Quality Study. Report on Concentration of Airborne Volatile Organic Compounds, Center for Science and Industrial Research, Environmental Services Group.

6 Dockery DW, Pope AC, Xu X et al. (1993) An association between air pollution and mortality in six US cities, *New England Journal of Medicine* vol 329: pp. 1753-1759.

7 Cairncross, E (1998) Environmental Science: Air pollution Module. Cape Town: Peninsula Technikon. [Unpublished course notes]. [Textual reference: Cairncross, 1998]

8 Brown Haze II study press release. (October 2004) Available at http://www.capetown.gov.za/clusters/health.

9 Malm, W.C. (1999) Particle concentration and visibility trends, Introduction to Visibility, Fort Collins: Colorado State University.

10 Malm presentation on Illumination Independent Aerosol Optical Properties. Available at vista.cira.colostate.edu/improve/ Education/ Workshops/ WESTAR/ Malm/ partii_malm

11 Fenger J (1999): Urban air quality, *Atmospheric Environment* vol. 33: pp. 4877-4900.

12 Ravishankara, A. R., Rudich, Y., Talukdar, R., and Barone, S. (1997) Oxidation of atmospheric reduced sulphur compounds: perspective from laboratory studies, Phil. Trans. R. Soc. Lond. B vol. 35: pp. 171-182.

13 Charlson, R.J., Schwartz, S.E., Hales, J. M., Cess, R.D., Coakley, J.A., Hansen, J.E., and Hofmann, D.J. (1992) Climate forcing by anthopogenic aerosols, *Science* vol. 255: pp. 423-430.

14 Hinds, W. C. (1984) Aerosol Technology. New York, NY, John Wiley and Sons, Inc.

15 Seinfeld, J. H. and Pandis, S.N. (1998) Atmospheric Chemistry and Physics. New York, NY, John Wiley and Sons, Inc.

16 Horvath, H. (1994) Proceedings of the Conference on Visibility and Fine Particles, *Atmospheric Environment* vol. 28 : 755-1082.

17 Solomon, S., Garcia, R. R., Rowland, F. S., and Wuebbles, D. J. (1986) On the depletion of Antarctic ozone, *Nature* vol. 321: pp. 755-758.

18 Kulmala, M. et.al, (2004) Formation and growth rates of ultrafine atmospheric particles: a review25 of observations, *Journal of Aerosol Science* vol. 35: pp.143–176.

19 O'Dowd, C.D., and Smith, M.H. (1993) Physicochemical properties of aerosols over the Northeast Atlantic: evidence for wind-speed related submicron sea-salt aerosol production, *Journal of Geophysics*. Res vol. 98: pp. 1137-1149.

20 Hoffmann, T., Odum, J. R., Bowman, F., Collins, D., Klockow, D., Flagan, R. C., and Seinfeld , J. H. (1997) Formation of Organic aerosols from the oxidation of Biogenic hydrocarbons, *Journal of Atmospheric Chemistry* vol. 26: pp.189-222.

21 Griffin, RJ., Cocker III, D.r., Flagan, R.C., and Seinfeld, J.H (1999) Organic aerosol formation from the oxidation of biogenic hydrocarbons, *Journal of Geophysics* vol.104: pp. 3555-3567.

22 Gray, H.A., Cass, G. R., Huntzicker, J. J., Heyerdahl, E. K., and Rau, J. A. (1986) Characteristics of atmospheric organic and elemental carbon particle concentrations in Los Angeles, *Environmental Science and Technology* vol. 20: pp. 580-589.

23 Saxena, P., Hildermann, L. M., McMurry, P.H., and Seinfeld, J.H. (1995) Organics alter hygroscopic behaviour of atmospheric particles, *Journal of Geophysics* vol. 100: pp. 18755-18770.

24 Harley, R.A. & Cass, G.R. (1995) Modeling the atmospheric concentrations of individual volatile organic compounds, *Atmospheric Environment* vol. 29: pp. 905–922

25 Brimblecombe, P., Clegg, S.L., Davies, T.D., Shooter, D. and Tranter, M., (1987) Observations of the preferential loss of major ions from melting snow and laboratory ice, *Water Resources* vol. 21: pp. 1279-1286

26 Noble, C. A. and Prather, K.A. (1998) Aerosol Time-of-Flight Mass Spectrometry: A New Method for Performing Real-time Characterization of Aerosol Particles, Appl. Occup. Environ. Hyg vol. 13: 439-443

27 Pitts, J. N. Jr (1977) Mechanism of photochemical reactions in urban air. Volume I. Chemistry studies. U.S. Environmental Protection Agency Report EPA 600/3-77-014a.

28 US EPA (Environmental Protection Agency) (1996) Air quality criteria for particulate matter. Volume I-3. EPA Report No. EPA/001a-cF, Office of Research& Development, U.S. Environmental Protection Agency, Washington, DC.

29 Phalen, R. F. (1984) Inhalation Studies: Foundations and Techniques. Boca Raton. FL: CRC Press. 277.

30 Pope III, C. A., et al. (1995). Particulate Air Pollution as a Predictor of Mortality in a Prospective Study of U.S. Adults, Am. J. Respir. Crit. Care Med vol. 151: pp. 669-674.

31 Schwartz, J. Dockery, D.W., Neas, L.M. (1996) Is daily mortality associated specifically with fine particles?, *JAWMA* vol. 46: pp. 927-39.

32 Schwartz, J. and Morris, R. (1995) Air Pollution and Hospital Admissions for Cardiovascular Disease in Detroit, Michigan, *American Journal of Epidemiology* vol. 142(1): pp. 23-35.

33 Pope III, C. A. 2000. Epidemiology of Fine Particulate Air Pollution and Human Health Biologic Mechanisms and Who's at Risk?, *Environmental Health Perspectives* vol. 108: pp. 713-723.

34 Schwartz, J., et al. (2001) The Concentration- Response Relation between Air Pollution and Daily Deaths, *Environmental Health Perspectives* vol. 10: pp. 1001-1006.

35 Harre, E. S. M., Price P. D., Ayrey, R. B., Toop, L. J., Martin, I. R., Town, I. G. (1997) The respiratory effects of air pollution in chronic obstruction pulmonary disease. A three month prospective study, *Thorax* vol. 52: pp. 1040- 1044.

36 Donaldson, K., & MacNee, W. (1998) Ultrafine (nanometer) particle-mediated lung injury, *Journal of Aerosol Science* vol. 29: pp.553-560.

37 USEPA (2002) Health Assessment Document for Diesel Emission.Office of Research and Development. EPA/600/8-90/057C.

38 Claiborn, C.S., Larson, T., & Sheppard, L. (2002) Testing the Metals Hypothesis in Spokane, Washington, Environmental Health Perspectives vol. 100: pp.547 – 552.

39 Seaton A, MacNee W, Donaldson K. et al. (1995) Particulate air pollution and acute health effects, *Lancet* vol. 345: pp. 176-178.

40 Siegmann, K. (2000) Soot Formation in Flames, *Journal of Aerosol Scie*nce vol 31: pp. 217-S218.

41 Harrison, R. M., et al. (2000) Measurement of Number, Mass and Size Distribution of Particles in the Atmosphere, Phil. Trans. R. Soc. Lond. A vol. 358: pp. 2567-2580

42 Woodruff, T.J., Grillo, J. & Schoendorf, K.C. (1997) The Relationship between Selected Causes of Postneonatal Infant Mortality and Particulate Air Pollution in the United States Article title, Environmental Health Perspective vol. 105: pp. 608-612.

43 Vedal, S., Petkau, J., White, R., & Blair, J. (1998) Acute effects of ambient inhalable particles in asthmatic and nonasthmatic children, Am J Respir Crit Care Med vol. 157: pp.1034–1043.

44 Pope A.C., et al (2002) Lung cancer, Cardiopulmonary mortality, and long-term exposure to fine particulate air pollution, *JAMWA* vol. 287: pp. 1132 – 1141.

45 Ostro, B., Broadwin, R., Green, S., Feng, W, Y., and Lipsett, M. (2006) Fine Particulate Air Pollution and Mortality in Nine California Counties: Results from CALFINE, *Environmental Health Perspective* vol. 114: pp. 29-33

46 Cohen AJ et al (2004). Mortality impacts of urban air pollution. In: Ezzati M et al., eds. Comparative quantification of health risks: global and regional burden of disease attributable to selected major *risk factors*. Geneva, World Health Organization: 1353–1433

47 Nyberg F et al. (2000) Urban air pollution and lung cancer in Stockholm, *Epidemiology* vol. 11, pp. 487– 495

48 Zanobetti, A., Schwartz, J., and Dockery, D.W. (2000) Airborne Particles Are a Risk Factor for Hospital Admissions for Heart and Lung Disease, *Environmental Health Perspectiv.* vol. 108: pp. 1071-1077

49 USEPA (1996) Review of the National Ambient Air Quality Standards for Particulate Matter: Policy assessment of scientific and technical information. Research Triangle Park, NC, Office of Air Quality Planning and Standards (Staff paper EPA-452\R-96-013)

50 Hurley, F et al (2005) *Methodology for the cost–benefit analysis for CAFE. Volume 2: health impact assessment.* Brussels, European Commission. (http://europa.eu.int/comm /environment/ air/ cafe/pdf/cba_methodology_vol2.pdf, accessed 13 December 2005

51 A Health impact assessment of air pollution and communication. Third year report, 2002–2003. Brussels, APHEIS Programme, European Commission, 2004 (http://www.apheis.net/Apheis-3NEW1.pdf, accessed 3 November 2005)

52 Ostro B.D., Lipsett, M.J., Mann, J., Braxton-Owens, H., & Wjite, M. (2001) Air Pollution and exacerbation of asthma in African-American children in Los Angeles, *Epidemiology* vol. 12: pp. 200 - 208.

53 Linn, W.S., Szlachcic, Y., Gong, H., Kinney, P.L., and Berhane, K.T. (2000) Air Pollution and Daily Hospital Admissions in Metropolitan Los Angeles, *Environmental Health Perspective* vol. 108: pp. 427-434.

54 Ostro, B.D. (1987) Air pollution and morbidity revisited: a specification test, *Journal of Environmental Economics and Management* vol. 14: pp. 87-98.

55 Ostro, B.D., & Rothschild, S. (1989) Air pollution and acute respiratory morbidity: an observational study of multiple pollutants, *Environmental Research* vol. 50: pp. 238–247.

56 Ostro, B.D., Eskeland, G.S., Sanchez, J.M., & Feyzioglu, T. (1999) Air pollution and health effects: a study of medical visits among children in Santiago, Chile, *Environmental Health Perspective* vol. 107: pp. 69 – 73.

57 Dockery, D.W., Pope, C.A. (1994) Acute respiratory effects of particulate air pollution, Annual Review of Public Health vol. 15: pp. 107-32.

58 American Lung Association. June (1995), Dollars and Cents: The economic and health benefits of potential particulate matter reduction in the United States, 1740 Broadway, New York

59 Intergovernmental Panel on Climate Change (IPCC) (2001): Radiative Forcing of Climate Change and an Evaluation of the IPCC IS92 Emission Scenarios. Cambridge University Press, Cambridge, UK

60 Andreae, M.O. (1995) Climate effects of changing atmospheric aerosol levels, in World Survey of Climatology, Future Climates of the World vol. 16: pp. 341-392.

61 Penner, J.E., Charlson, R.J., Hales, J.M., laulainen, N.S., Leifer, R., Novakov, T., Ogren, J., Radke, L. F., Scwartz, S.E., and Travis, L. (1994) Quantifying and minimizing uncertainty of climate forcing by anthropogenic aerosols, Am. *Meteorological Society.* vol. 75: pp. 375-400.

62 Twomey, S. (1991) Aerosols, clouds and radiation, *Journal of Atmospheric Environmen.* vol. 25: pp. 2435-2442.

63 Rosenfeld, D., (1999): TRMM observed first direct evidence of smoke from forest fires inhibiting rainfall, *Journal of Geophys* vol. 26: pp. 3105-3108.

64 International Panel on Climate Change (IPPC). (2001) **IPCC Third Assessment Report: Synthesis Report.** IPCC, Geneva, Switzerland.

65 Groblicki, P.J., Wolff, G. T., and Countess, R.J. (1981) Visibility-reducing species in the Denver "Brown Cloud" Relationships between extinction and chemical composition, *Atmospheric Environment* vol. 15: pp. 2473-2484.

66 Malm, W., (1979) Considerations in the Measurement of Visibility, JAPCA vol. 29: p. 1042-1052

67 Gebhart, K.A., Lattimer, D.A., and Sisler, J F. (1990) Empirical orthogonal function analysis of the particulate sulphate concentrations measured during WHITEX, in

Visibility and Fine particulates, AWMA TR-17, edited by C. V. Mathai. Air & Waste Management Association, Pittsburgh, PA, pp. 860-871.

68 Ministry of Environment (New Zealand). (2002) A report on Good Practive guide for Visibility Measurement in New Zealand. Available at www.mfe.govt.nz.

69 Igbal, M. (1983) An Introduction to Solar Radiation. Academic Press, Toronto.

70 Trijonis, J. (1980). Visibility in California, Final report to the California Air Resources Board for ARB Contract A7-181-30

71 Williams, D.J., Milne, J.W., Roberts, D.B., Jones, D.J.A., (1982) The optical properties of Sydney,s brown haze. In: Carras, Johnson (Eds.), Urban Atmosphere –Sydney. A Case Study pp. 125-140

72 Babson, B.L. et al. (1980) A comparison of telephotometer and nephelometer measurements by statistical analysis of regional field data. Preprint volume of EPA *Symposium on Plumes and Visibility*, Grand Canyon.

73 Malm, W.C., Molenar, J.V. (1994) Visibility measurements in National Parks in the Western United States, *Journal of the Air Pollution Control Association.* vol. 34: pp. 899-904.

74 Larson, S.M., Cass, G.R., Hussey, K.J., & Luce, F. (1998) Verification of Image Processing based visibility models, *Environmental Science & Technology* vol. 22: pp. 629 – 637.

75 Luo, C.H., Liu, S.H., Yuan, C.S. (2005) Investigation of Urban atmospheric visibility by high-frequency extraction: Model development and field test, Journal of Atmospheric Environment vol. 39: pp. 2545-2552.

76 Gonzalez, R.C., Woods, R.E. (2002) Digital Image Processing, second ed. Pearson Education, Inc. publishing as Prentice Hall, Englewood Cliffs, NJ.

77 Cleary, G. T. (2001) Video Detection and Monitoring of Smoke Conditions AUBE'01, Proceeding, Gaithersburg, MD, Gross handler, W., Ed.

78 Budgett, D.M., & Mason, A.J. (1998) Software for Visibility Monitoring by Digital Camera, Stage 2: Algorithm Assessment Using Image database. Auckland Uni-services Limited, Report Ref: 7324.

79 Watson, J.G., Lioy, P.J. and Mueller, P.K. (1983) The Measurement Process: Precision, Accuracy and Validity, in: *Air Sampling Instruments for Evaluation of Atmospheric Contaminants 6th Ed.,* P.J. Lioy and M. Lioy (Eds.), American Conference of Industrial Hygienists, Cincinnati, Ohio.

80 Molenar, J.V. (1993) Uncertainty Analysis of Calculated Extinction from Apparent Contrast Measurements from Images of Natural Targets. Air Resource Specialists, Inc Ft. Collins, Co, 80525.

81 Malm, W.C., Kelley, K., Molenar, J., & Daniel, T. (1981) Human perception of visual air quality (uniform haze), *Atmospheric Environment* vol. 15: pp. 1875-1890.

82 Dietrich, D. L., M. A. Klitch, D. S. Cismoski, and J. V. Molenar (1989) An Assessment Of The Accuracy And Precision Of Photographic Densitometric Measurements For Monitoring Visual Air Quality, in: *Transactions: Visibility and Fine Particles,*C. V. Mathai Editor, Air and Waste Management Association, Pittsburgh, Pa. pp. 281-292.

83 Johnson, C. E., W. C. Malm, G. Persha, J. V. Molenar, and J. R. Hein, (1985) Statistical Comparisons Between Teleradiometer Derived and Slide Derived Visibility Parameters, *JAPCA* vol. 35: pp. 1261-1265.

84 Wicking-Baird, M.C., de Villiers, M.G. and Dutkiewicz, R.K. (1997) Cape Town Brown Haze Study. Report No. GEN 182, Energy Research Institute, University of Cape Town

85 Trijonis, J.C., and Pitchford, M. (1987) Preliminary extinction budget results from the RESOLVE program edited by P.S. Bhardwaja, Air and Waste Management Association, Pittsburgh, PA

86 Trijonis, J.C., Malm, W.C., Pitchford, M., White, W.H., Charlson, R., and Husar, R. (1990) Visibility: Existing and historical conditions-causes and effects, in Sate Sci. State Technol. Rep. 24, National Acid Precipitation Assessment Program, Washington, D.C

87 White, W.H. (1990) Contributions to light scattering, In: Acidic Deposition: State of Science and Technology Report 24, J. Trijonis (lead author), National Acid Precipitation Assessment Program, Washington D.C, pp. 85-102

88 Chow, J.C., Bachmann, J.D., Wierman, S.S.G., Mathai, C.V., Malm, W.C., White, W.H., Mueller, P.K., Kumar, N., Watson, J.G. (2002) Critical Review Discussion: Visibility: Science and Regulation, *Journal of Air and Waste Management* vol. 52: pp. 973-999

89 Chow, J.C, Watson, J.G., Pritchett, L.C., Pierson, W.R., Frazier, C.A. and Purcell, R.G. (1993) The DRI thermal/optical reflectance carbon analysis system: description, evaluation, and applications in U.S. air quality studies, *Atmospheric Environment* vol. 27: pp. 1185-1201.

90 Richards, L.W. et al (1989) Extinction Apportionment for the Denver Brown Cloud; AWMA Transactions.

91 International Civil Aviation Organization (ICAO) (2001) Chapter 4: Visibility, Manual of Runway Visual Range Observing and Reporting Practices (Doc 9328).

92 IMPROVE (Interagency Monitoring of Protected Visual Environments) (1993). Spatial and temporal pattern and the chemical composition of the haze in the United States.

93 Scorgie Y, Annegarn H, Burger L. (2004) *Study to Examine the Potential Socio-Economic Impact of Measures to Reduce Air Pollution from Combustion.* Fund for Research into Industrial Development Growth and Equity [FRIDGE]. Airshed Planning Professionals (Pty) Ltd: Johannesburg.

94 Jackson, R (1998) Community Visibility Survey, Manawatu-Wanganui Region, New Zealand.

95 Yang, H.Y. & Yuan, C.S. (2004) Prediction of Urban Air Quality by Using Visibility as an Indicator in Southern Taiwan. The 15th IUPPA International Conference on Air Quality, London, England.

96 Dracoulides, D.A (1994); Air Pollution Modelling for the Greater Cape Town Region; MSc Thesis Faculty of Engineering; Energy Research Institute, University of Cape Town.

97 IMPROVE (Interagency Monitoring of Protected Visual Environments) (1993). DECIEW, A STANDARD VISIBILITY INDEX. Improve Newsletter vol 2, No. 1

98 Henry, R.C. (1979) Psychophysics and Visibility Values. In: Proceedings of the Workshop on Visibility Values, Fox, D., R.J. Loomis and Greene, T.C. (Technical Coordinators). Fort Collins, Colorado. U.S. Department of Agriculture.